1-1-2015

Optomechanical Devices and Sensors Based on Plasmonic Metamaterial Absorbers

Hai Zhu
University of Pennsylvania, zhuhai@seas.upenn.edu

Optomechanical Devices and Sensors Based on Plasmonic Metamaterial Absorbers

Abstract
Surface plasmon resonance is the resonant oscillations of the free electrons at the interface between two media with different signs in real permittivities, e.g. a metal and a dielectric, stimulated by light. Plasmonics is a promising field of study, because electron oscillations inside a subwavelength space at optical frequencies simultaneously overcome the limit of diffraction in conventional photonics and carrier mobilities in semiconductor electronics. Due to the subwavelength confinement, plasmonic resonances can strongly enhance local fields and, hence, magnify light-matter interactions. Optical absorbers based on plasmonic metamaterials can absorb light resonantly at the operating wavelengths with up to 100% efficiency. We have explored plasmonic absorbers at infrared wavelengths for thermal detectors, e.g. a gold nanostrip antenna absorber that can absorb 10-times light using only 2% of material consumption comparing to a uniform gold film.

In an optomechanical device, the optical mode and mechanical mode are mutually influenced, through the optical forces exerted on the mechanical oscillator and the detuning of optical resonance by the mechanical oscillator, so that the mechanical oscillations are either amplified or suppressed by light. We designed an optomechanical device integrated with plasmonic metamaterial absorber on a membrane mechanical oscillator, wherein a tunable Fano-resonant absorption in the absorber arises from the coupling between the plasmonic and Fabry-Perot reonsances. The absorber traps the incident light and heat up the membrane, causing an increase in thermal stress and a normal plasmomechanical force on it. This is a light-absorption-dependent elastic force arising from the opto-thermo-mechanical interactions. Due to the finite thermal response time in the membrane, the elastic plasmomechanical force is delayed and, consequently, generates a viscous component modifying the damping rate of the mechanical oscillator. We have observed optomechanical amplification and cooling in the device at designed detuning conditions. In particular, on the condition that the optomechanical gain beats the intrinsic mechanical damping, the oscillation becomes coherent, i.e. phonon lasing. We successfully demonstrated phonon lasing with a threshold power of 19 μW. This device is promising as an integration-ready coherent phonon source and may set the stage for applications in fundamental studies and ultrasonic imaging modalities.

Degree Type
Dissertation

Degree Name
Doctor of Philosophy (PhD)

Graduate Group
Materials Science & Engineering

First Advisor
Ertugrul Cubukcu

Keywords
Absorber, Metamaterial, Nanophotonics, Optomechanics, Phonon laser, Plasmonics

Subject Categories
Mechanics of Materials | Optics | Physics

OPTOMECHANICAL DEVICES AND SENSORS BASED ON PLASMONIC METAMATERIAL ABSORBERS

Hai Zhu

A DISSERTATION

in

Materials Science and Engineering

Presented to the Faculties of the University of Pennsylvania

in

Partial Fulfillment of the Requirements for the

Degree of Doctor of Philosophy

2015

Supervisor of Dissertation

_____

Ertugrul Cubukcu

Assistant Professor, Materials Science and Engineering

Graduate Group Chairperson

_____

Shu Yang

Professor, Professor, Materials Science and Engineering

Dissertation Committee

Ritesh Agarwal, Professor, Materials Science and Engineering

Lee C. Bassett, Assistant Professor, Electrical and Systems Engineering

Cherie R. Kagan, Stephen J. Angello Professor, Electrical and Systems Engineering

OPTOMECHANICAL DEVICES AND SENSORS BASED ON PLASMONIC METAMATERIAL ABSORBERS

Hai Zhu

To My Family

ACKNOWLEDGMENT

This thesis summarizes my Ph.D. work in the past half-decade at Penn MSE department. During the time, I have tasted sweetness of success as well as bitterness of failure. I would not be sitting here and writing this without the support from many awesome people, to whom I am going to express my sincere appreciation in this acknowledgment.

First and foremost, I must thank my dear advisor, Prof. Ertugrul Cubukcu, for all his great support, including inspiring guidance, patient encouragement, and kind concerns, from beginning to end. I am very fortunate to have met him. He possesses immense knowledge in physics, optics, and electrical engineering. I have been introduced to the field of nanophotonics and optomechanics and kept motivated all by his mentorship. He is enthusiastic about scientific research and full of ideals, and as a result I have got opportunities to engage in multiple interesting projects and enriched my experience and skills. He asked to always consider the major factor before the minor ones. That advice deeply influenced me and will benefit me forever. I will never forget his strong support during my hard time at school and in life. He has devoted tremendous time and effort to the entire course of my Ph.D. work and made my success.

I want to acknowledge my thesis committee members, Prof. Ritesh Agarwal, Prof. Lee C. Bassett, Prof. Nader Engheta, and Prof. Cherie R. Kagan, for their valuable time and effort on my research proposal, annual thesis progress reports, and dissertation defense. Their insightful comments and suggestions made this thesis better-looking. I feel lucky that Prof. Agarwal can attend my dissertation defense though he was recently burdened with his newborn angel. I am grateful to Prof. Bassett for graciously joining my committee on short notice. Prof. Engheta provided the courses of Electromagnetic and Optical Theory I & II, which benefited me profoundly. His excellent research work on metamaterials was important references for my Ph.D projects. Although he is unable to attend the dissertation defense, I want to express my appreciation towards Prof. Engheta. Prof. Kagan is my first known faculty among the committee. Her lectures on semiconductors and nanotechnologies sparked my interest towards nano research. I want to express my gratitude towards Prof. Kagan.

I also want to thank my awesome labmates, Prof. Fei Yi, Mr. Jason Reed, Mr. Qiushi Guo, Dr. Jiechang Hou, Prof. Feng Liu, Mr. Euijae Shim, Mr. Alexander Zhu, Mr. Guanqing Hao, Ms. Stephanie Malek, and Mr. Yichen Lu, for all kinds of help. It is a precious experience for us from all over the world to meet and work together at Penn. Prof. Yi and Mr. Reed are almost everywhere in my memories associated with LRSM Rm 400. We had many productive collaborations, wherein they gave so much help and support. I want to give special thanks to Prof. Yi and Mr. Reed (Dr. Reed by the time of my thesis deposition). I also want to specially thank Mr. Guo and Dr. Hou for the pleasant collaboration experiences.

I am grateful to faculties and staff that have assisted me on my work and life at Penn. I have invested a lot of time doing research at the Quattrone Nanofabrication Facility (QNF), Wolf Nanofabrication Facility (WNF), Nanoscale Characterization Facility (NCF, the formerly PRNF), and Nano/Bio Interface Center (NBIC). I must acknowledge these facilities and thank the associated staff for providing trainings and consultation. I thank Prof. Robert Carpick for granting me access to the Optical Profilometer in his lab. I thank Prof. Dawn Bonnell for sharing the precious PVD materials. I thank Prof. Christopher Murray and Dr. Xingchen Ye for helping with the FTIR tool in their lab. I thank Prof. Daniel Gianola and Prof. Christopher Murray for giving me the opportunities for teaching assistant practice in MSE/MEAM 505 and MSE 360. I thank the lovely administrative staff of the MSE department, including Ms. Vicky Lee, Ms. Pat Overend, and Ms. Irene Clements, for all the care and assistance they provided during my years spent at the LRSM Building.

Last but not least, I want to express my deepest love and appreciation to my family. My grandmother Ailian Tan nurtured me since I was born and has influenced my character. My grandfather Quan Zhu is my idol and has always been motivating me to fight my way. My father Shujun Zhu and mother Chiping Huang raised me up healthy and happy with their selfless and unconditional love. They have been trusting and supporting me, so I could reach here on the scientific career path. To them, I am indebted forever. Finally, I want to express my special gratitude to the love of my life, Fei Li, for her non-stop accompany since 2011. She made my Ph.D. life not dull at all. I lost my wedding band after an experiment ran overtime, but Fei comforted me saying

“working hard should be rewarded” and encouraged me to get over the guilt. It is her constant support and encouragement that allows me to pursue what I like to do with no worries. No words are able to describe how much I love them. I must dedicate this thesis to all my family.

The major funding for my Ph.D. projects from the University of Pennsylvania and the National Science Foundation (ECCS-1408139) and is also acknowledged.

ABSTRACT

OPTOMECHANICAL DEVICES AND SENSORS BASED ON PLASMONIC METAMATERIAL ABSORBERS

Hai Zhu

Ertugrul Cubukcu

Surface plasmon resonance is the resonant oscillations of the free electrons at the interface between two media with different signs in real permittivities, e.g. a metal and a dielectric, stimulated by light. Plasmonics is a promising field of study, because electron oscillations inside a subwavelength space at optical frequencies simultaneously overcome the limit of diffraction in conventional photonics and carrier mobilities in semiconductor electronics. Due to the subwavelength confinement, plasmonic resonances can strongly enhance local fields and, hence, magnify light-matter interactions. Optical absorbers based on plasmonic metamaterials can absorb light resonantly at the operating wavelengths with up to 100% efficiency. We have explored plasmonic absorbers at infrared wavelengths for thermal detectors, e.g. a gold nanostrip antenna absorber that can absorb 10-times light using only 2% of material consumption comparing to a uniform gold film.

In an optomechanical device, the optical mode and mechanical mode are mutually influenced, through the optical forces exerted on the mechanical oscillator and the detuning of optical resonance by the mechanical oscillator, so that the mechanical oscillations are either amplified or suppressed by light. We designed an optomechanical device integrated with plasmonic metamaterial absorber on a membrane mechanical oscillator, wherein a tunable Fano-resonant absorption in the absorber arises from the coupling between the plasmonic and Fabry-Perot reonsances. The absorber traps the incident light and heat up the membrane, causing an increase in thermal stress and a normal plasmomechanical force on it. This is a light-absorption-dependent elastic force arising from the opto-thermo-mechanical interactions. Due to the finite thermal

response time in the membrane, the elastic plasmomechanical force is delayed and, consequently, generates a viscous component modifying the damping rate of the mechanical oscillator. We have observed optomechanical amplification and cooling in the device at designed detuning conditions. In particular, on the condition that the optomechanical gain beats the intrinsic mechanical damping, the oscillation becomes coherent, i.e. phonon lasing. We successfully demonstrated phonon lasing with a threshold power of 19 μW. This device is promising as an integration-ready coherent phonon source and may set the stage for applications in fundamental studies and ultrasonic imaging modalities.

TABLE OF CONTENTS

ACKNOWLEDGMENT ..... **IV**

ABSTRACT ..... **VII**

LIST OF TABLES ..... **XIII**

LIST OF ILLUSTRATIONS ..... **XIV**

CHAPTER 1: INTRODUCTION **2**

1.1. Background **2**
1.1.a. Optical Materials and Metamaterials 2
1.1.b. Mechanical Effects of Light and Optomechanics 8

1.2. Light Absorption in Lossy Media **12**
1.2.a. The Propagation of Light in Lossy Media 12
1.2.b. Microscopic Mechanisms for Light Absorption 13

1.3. Optics of Linear, Homogeneous, Isotropic, and Nonmagnetic Metals **17**
1.3.a. Metal Conductivity at High Frequencies 17
1.3.b. Metal Permittivity Function at High Frequencies 20
1.3.c. Light Dissipation in Metals 21

1.4. Plasmonics and Surface Plasmon Resonances **23**
1.4.a. Free Electron Gas in Metals 23
1.4.b. Surface Plasmon Polaritons 26
1.4.c. Localized Surface Plasmons 29

1.5. Cavity Optomechanics **30**
1.5.a. Optical and Mechanical Resonance Coupling 30
1.5.b. Optomechanical Effects: in the Perspective of Forces 33
1.5.c. Optomechanical Effects: in the Perspective of Energy 38

1.6. Thesis Outline **39**

1.7. References **40**

CHAPTER 2: OPTICAL ABSORBERS BASED ON SURFACE PLASMON RESONANCES **44**

2.1. Introduction 44

2.2. Plasmonic Absorbers in Infrared for Thermal Detectors 45
2.2.a. Background 45
2.2.b. Absorber Design 46
2.2.c. FDTD Simulation Study 47

2.3. Tunable Plasmonic Absorbers by Plasmonic and Optical Mode Coupling 53
2.3.a. Absorber Design and Simulation Study 53
2.3.b. Coupled Oscillator Model 56

2.4. Conclusions 58

2.5. References 59

CHAPTER 3: SILICON NITRIDE MEMBRANES AS MECHANICAL OSCILLATORS 62

3.1. Introduction 62

3.2. Vibrational Eigenmodes of a Square Membrane Oscillator 63

3.3. Membrane Motion Measurement by Laser Interferometry 66

3.4. Conclusions 70

3.5. References 71

CHAPTER 4: OPTO-THERMO-MECHANICAL COUPLING IN THE DEVICE 72

4.1. Introduction 72

4.2. Thermal Response of the Membrane 72
4.2.a. Heat Transfer Analysis by Green's Function 72
4.2.b. Thermal Response Time Constant 76

4.3. Thermomechanical Deflecion and Force on the Membrane Studied by FEM Simulations . 77
4.3.a. Heat Transfer Results 77
4.3.b. Membrane Deflection and Force Estimation 81

4.4. An Optomechanical Device Supporting Opto-thermo-mechanical Interactions 83
4.4.a. Plasmomechanical Force on the Membrane Oscillator 83
4.4.b. Phase-delayed Plasmomechanical Forces and Their Interaction with the Osicllator System 86

4.5. Plasmomechanical-Force-Induced Optomechanical Effects Analyzed by Coupled-mode Theory 88
4.5.a. Coupled-mode Equations and Their Solutions 88

4.5.b. The Solutions in unresolved sideband limit and adiabatic limit 94

4.6. Conclusions 96

4.7. References 97

CHAPTER 5: DEVICE FABRICATION AND ELECTROSTATIC TUNING TEST 98

5.1. Introduction 98

5.2. Fabrication Flow of the Device 98
5.2.a. The Fabrication Process of the Membrane Chip 98
5.2.b. The Fabrication Process of the Device Base 103
5.2.c. The Bonding Process 104

5.3. Optical Spectroscopy Study of the Device 105
5.3.a. Parallel Plate Capacitor Model 105
5.3.b. Linking the Gap Distance to the Bias Voltage by Optical Spectra 106

5.4. Conclusions 109

CHAPTER 6: PHONON LASING AND OPTOMECHANICAL COOLING IN THE DEVICE 111

6.1. Introduction 111

6.2. Two Optomechanical Effects in One Device 112

6.3. Coherent Mechanical Oscillations: Phonon Lasing 115
6.3.a. Phonon Laser Theory by Laser-Rate-Equations 115
6.3.b. Phonon Lasing in the Device 117
6.3.c. Broadband Capability 119

6.4. Optomechanical Cooling 121

6.5. Conclusions 123

6.6. References 124

CHAPTER 7: AN INFRARED DETECTOR BASED ON THERMOMECHANICAL PLASMONIC MEMBRANES 126

7.1. Introduction 126

7.2. Device Design and Simulations 127
7.2.a. Optical Absorber Design 127
7.2.b. Thermal and Mechanical Analysis 131

7.3. Nanobeam Deflection Detection 134
7.3.a. Deflection Measured by Fiber-optic Interferometer 134
7.3.b. Noise Measurement and Limit Analysis 137

7.4. Conclusions 140

7.5. Contributions 140

7.6. References 141

CHAPTER 8: A BIOSENSOR BASED ON LEAKY CAVITY MODE RESONANCES IN SILICON NANOWIRES 145

8.1. Introduction 145

8.2. Design and Principles of the Leaky Cavity Mode Resonance Biosensor 146
8.2.a. Overview of the Silicon Nanowire Biosensor 146
8.2.b. Microscopic Mechanisms for Light Absorption 148
8.2.c. Resonance Wavelength and Nanowire Cross-section Shape 150
8.2.d. Refractive Index Sensitivity of the Leaky Cavity Mode Resonance 153

8.3. Graphene-functionalized Surface Molecule Binding and Its Detection 154

8.3. Fabrication Process of the Silicon-on-Glass Device 159

8.4. Conclusions. 159

8.5. Contributions 160

8.6. References 160

LIST OF TABLES

Table 1. Electromagneic spectrum, the classes and their ranges in wavelength, frequency, photon energy, and temperature of an equivalent blackbody whose radiation is peaked at the wavelength. 17

Table 2. List of mechanical and thermal parameters of the materials in the bilayer membrane. 75

LIST OF ILLUSTRATIONS

Figure 1-1. The schematic of the integrated plasmonic optomechancial device. A plasmonic metamaterial absorber made of gold thinfilm (yellow) on silicon nitride membrane (blue) with cross-shaped nano holes is free standing above a gold back reflector (yellow). The gap separating the membrane and back reflector is tunable by applying a bias voltage. A 1550 nm laser beam is normally incident onto the membrane and affects the vibration of the membrane. The reflected laser beam is used to detect the vibration.....11

Figure 1-2. Electron oscillations in metals include (A) bulk plasmons which exist within the volume of a metal and (B) surface plasmons which exist only at the interface between a dielectric and a metal.....23

Figure 1-3. The schematic of a typical optomechanical system based on a Fabry-Perot cavity between the flexible end mirror (M1) and the fixed end mirror (M2). 31

Figure 1-4. Varying cavity lengths influence optical resonances. The broad spectra correspond to optical cavity resonances, and the narrow spectra correspond to laser lines. (A) The cavity length change (shortened) leads to detuning. (B) The mechanical motion of the end mirror modulates optical response. (C) Sidebands are generated by Doppler shift. Asymmetric sidebands occur because of (D) blue detuning or (E) red detuning of the cavity. 32

Figure 2-5. The schematic geometry and illumination configuration of the mid-IR nanoantenna absorber. L, W, and t represent the length, width, thickness of a single gold nanostrip, repectively. Px and Py are the longitudinal and lateral periods of the nanoantenna array. The array is illuminated from the top with electric field (E) polarized along the nanostrips. A 5 nm of titanium adhesion layer is assumed. 47

Figure 2-6. Absorber (A) The transmission T (red solid curve), reflection R (green solid curve), and absorption A (blue solid curve) spectra of the nanoantenna absorber.The absorption (A-A) spectra based on dissipated power is shown as hollow triangles. (B) The absorbance of a uniform gold layer for radiation with a wavelength of 6 μm as a function

of the film thickness. The solid curve is the analytical result calculated by transfer matrix method. The red dots are the FDTD results. (C) The absorption peak wavelength as a function of gold nanostrip length (L) for different widths (W). (D) The absorbance at 6 μm as a function of nanoantenna length (L) for various antenna widths (W). The geometric parameters t=20 nm and Px=Py=3000 nm are used for all these simulations. 48

Figure 2-7. The absorbance colormap as a function of (A) wavelength and longitudinal period (P_x), (B) wavelength and lateral period (P_y), and (C) wavelength and gold nanostrip thickness (t). (D) The colormap of the absorbance at 6 μm, as a function of Px and Py. The geometric parameters L=1500 nm, W=150 nm, t=20 nm, P_x=P_y=3000 nm are used for all these simulations, except the ones varying in the colormap. 51

Figure 2-8. The polarization angle (θ) dependence of absorption (at 6 μm) for the nanoantenna array (blue ♦) calculated at 6 μm. The curve resembles the expected $\cos^2\theta$ dependence. The nanoantenna array absorbance as a function of incidence angle for light polarized along the nanostrips (red ●) is also shown. 52

Figure 2-9. Plasmonic and FP cavity mode coupling. (A) The plasmonic coupled FP cavity consists of a semi-mirror (M1) made of a gold thinfilm of 25 nm thickness on a silicon nitride membrane of 100 nm thickness, and a second mirror (M1) made of a gold thinfilm of 50 nm. M1 is modified with nano sized cross-shape thru-holes, which supports plasmonic resonance at about 1437 nm. (B) The simulated spectra of the absorption on the plasmonic nanostructure. The black dashed curve is for nanoantennas only (M1); the red dotted curve is for FP cavity only (1200 nm gap between the holeless M1 and M2); the red curve is for the coupled mode (1200 nm gap between M1 and M2). 54

Figure 2-10. Simulated tuning of the plasmonic-FP hybrid Fano mode. (A) The absorption peak redshifts 59 nm as the FP cavity length increases from 1200 nm to 1300 nm. (B) The absorption spectra at different tuning conditions. The color shows the absorbance, each vertical line represents the absorption spectrum at the specific tuning condition (shown as the FP peak wavelength as well as the FP resonance detuned from plasmonic resonance frequency), and each horizontal line representd the absorption at the specific frequency when the cavity is tuned. The white dash line marks the frequency of interest (1550 nm), and the black dash circle marks the avoided crossing. 55

Figure 2-11. Hybrid Fano resonance interpreted by coupled oscillator model. (A) A typical FDTD simulation result showing the spactra for the plasmonic absorber (green), the FP cavity (blue), and the resulted Fano resonances (blue) for nearly zero detuning. (B) The coupled oscillator model simulates the spectra for different energy detuning values ($\hbar\omega_1 - \hbar\omega_2$). Panel (i) corresponds to the FDTD simulation result in (A). The qualitative agreement between the two is evident despite the simplified model. From Panel (i) to (iv), the FP resonance redshifts and $\hbar\omega_1$ decreases. (C) The schematic of the equivalent coupled mechanical harmonic oscillator model. 58

Figure 3-12. A silicon nitride membrane window on the frame. (A) The membrane of thickness of 100 nm appears transparent, sitting at the center of the silicon frame of 7.5 mm by 7.5 mm. A closer look under the microscope showing the (B) front and (C) back sides of the membrane window ("orange") of 500 μm by 500 μm. The membrane is leveled at the front side of the chip, so there are inclined side walls of silicon viewed from the back side. The colors of the micrographs are false due to white balance issues. 62

Figure 3-13. Demonstration of the vibrational eigenmodes of the square membrane oscillator. (A) The amplitude profiles of the lowest 8 eigenmodes. (B) The geometric parameters of the membrane in the Cartesian coordinate. 66

Figure 3-14. The schematic of the optomechanical measurement system. The area boxed by the red dash rectangular is in vacuum. The right bottom exemplifies a raw spectrum acquired by this system. The right top shows the major part of the vacuum chamber. ...68

Figure 3-15. The procedure to calculate sensitivity data. (A) The original FDTD-simulated reflectance at 1550 nm wavelength is adjusted by a linear transformation, so that the adjusted simulation curve matches the measured results in (B). (C) The sensitivities are calculated by taking the differential of the reflectance with respect to the absorber gap length. 70

Figure 4-16. The solution of heat equation (72). (A) The steady state temperature increase distribution along the center line on the membrane by computing the series in equation (79) up to m=101 and n=101, the values of relevant mechanical and thermal constants are from Table 2. (B) The temporal evolution of max temperature increase by computing the series in equation (80) up to m=101 and n=101. (C) The thermal response of the device

measured with a modulated input laser and lock-in amplifier, the 3dB frequency of 237 Hz is equivalent to a time constant of 0.67 ms. 76

Figure 4-17. The IR images of the device region (left) and laser spot (right) for laser spot size estimation. The images were recorded with the same magnification and pixel configuration. The laser spot size is estimated as ~41μm based on the known width (200 μm) of electrode channel. 78

Figure 4-18. The FEA simulation results on the heat transfer and membrane deflection. (A) The steady state temperature increase ΔT distribution along the center line on the membrane (the dashed line on the inset), for different optical spot sizes but same total power of 1mW. The inset is the 2D ΔT distribution for a spot size of 21.5 μm. (B) The temporal evolution of max ΔT , which is calculated at the center of the membrane, corresponding to (A). (C) The max ΔT scales linearly with heating absorbed optical power. (D) The typical membrane deflection profile (not up to scale). The curves are the membrane deflection (ΔZ) profiles, for the same cases as in (A). I The membrane deflection (ΔZ) profile when the membrane undergoes a uniform normal pressure of 0.4 Pa (100 nN on 500 μm by 500 μm area), and the average of the profile. (F) The max ΔZ , which occurs at the center of the membrane, and the average ΔZ scale linearly with the total uniform force. The spring constants calculated by the inverse of slope are 9.55 N/m based on max ΔZ and 16.3 N/m based on average ΔZ 80

Figure 4-19. Plasmomechanical force arises from the opto-thermo-mechanical interactions. Compare to (A) the membrane at balance position, (B) the membrane at a small displacement of ΔZ exhibits a decreased absorption. Their force compositions are shown in (C), revealing that the membrane is subjected to the net plasmomechanical force $F_{pm}\left(\Delta Z\right) \propto \Delta Z$ in addition to the net membrane elastic force $F_{mem}\left(\Delta Z\right) \propto \Delta Z$ 84

Figure 4-20. Time-varying reactive plasmomechanical force and its rate of work to the mechanical oscillator. (A) In a damping-free harmonic oscillator, the velocity $\vec{v}\left(t\right)$ (grey dashed curve) is $\frac{\pi}{2}$ after the displacement $\vec{x}\left(t\right)$ (orange curve). The rate of work done by the plasmomechanical force to the mechanical oscillator is $P\left(t\right) = \vec{F}_{pm}\left(\vec{x}\left(t\right)\right) \cdot \vec{v}\left(t\right)$,

and its time-varying values are exemplified in several cases where $\vec{F}_{pm}\left(\vec{x}(t)\right)$ (purple curve) has different phases. (B) The optomechanical amplification scenario: $\vec{F}_{pm}\left(\vec{x}(t)\right)$ is out-of-phase with $\vec{v}(t)$, and $P(t)$ is positive during most of the time in one period. (C) The unperturbed scenario: $\vec{F}_{pm}\left(\vec{x}(t)\right)$ is in-phase with $\vec{v}(t)$, and $P(t)$ is positive during half of the time in one period. (D) The optomechanical cooling scenario: $\vec{F}_{pm}\left(\vec{x}(t)\right)$ is out-of-phase with $\vec{v}(t)$ but the direction is reversed from (B), and $P(t)$ is negative during most of the time in one period. 87

Figure 5-21. The major fabrication steps for the membrane chip. 99

Figure 5-22. SEM images of the absorber. (A) The square area (240 μm by 240 μm) at the center of the membrane window is the plasmonic nanostructures (metasurface). (B) The close-up of cross-shaped hole array on the bilayer membrane, wherein length is about 360 nm, the width is about 100 nm, and the period of the square array is 800 nm.....102

Figure 5-23. The major fabrication steps for the device base. 103

Figure 5-24. The membrane chip is bonded to the device base to make the completed device, the right photo demonstrates a real device wherein the “green lighting spot” at the center is the plasmonic metamaterial absorber area.....105

Figure 5-25. Blue and red detuning of the Fano resonance in the device. (A) Simulated spectral absorbance for the optomechanical device (blue curve): The Fano resonance arises from the coupling between the FP (green dashed curve) and plasmonic resonance (red curve). The Fano resonance peak position is voltage tunable, and the results shown are for the device biased at 5.5 V, where the absorbance peak nearly reaches unity. (B) Measured metamaterial absorption spectra of the device biased at 3.2 V (magenta dashed line in (C)) and 5.5 V (cyan dashed line in (C)) corresponding, respectively, to the cases where the 1550 nm laser (vertical grey line) is detuned to the blue and red side from the Fano peak. (C) Measured spectral absorbance for a range of absorber gaps. The Fano peak wavelength (yellow-white region) tunes linearly with the absorber gap.....107

Figure 5-26. Device absorbance spectra by measurement and simulation. The measured spectra at 0, 10, 20, 30, 40, 50, and 60 in the unit of square of voltage are plotted with the

bold curves, showing a linear blueshift. The simulated spectra are corresponding to the absorber gap distances from 2950 nm to 2500 nm with 10 nm change step between each spectrum, also exhibiting a linear blueshift. 108

Figure 6-27. Mechanical spectra of optomechanical amplification (red), weak interaction (green), and cooling (blue) for the deivce under different bias voltages. The incident laser power of 17 μW is used for the measurement. 112

Figure 6-28. Optomechanical amplification and cooling in one device. (A) The differential spectral absorbance vs frequency detuning. (B) The total mechanical damping $\Gamma = \Gamma_0 + \Gamma_{pm}$ vs frequency detuning. The measured data (dots) is in excellent agreement with theory (solid lines). The mechanical linewidth is decreased ($\Gamma_{pm} < 0$) at negative (blue) detuning and increased ($\Gamma_{pm} > 0$) at positive (red) detuning. 115

Figure 6-29. Phonon lasing in the device tuned at 3.2 V. (A) The mechanical linewidth decreases linearly until it reaches below the instrument limit of 0.58 Hz at the threshold pump power of about 19 μW (B) The mechanical peak amplitude increases with the optical pump power. Above the same threshold pump power, the mechanical amplitude increases drastically until it saturates. (C) The mechanical output power, generally proportional to the square of the amplitude, increases with the optical pump power. The measurements (dots) are fitted by equation (130), yielding the theory curve and giving the power threshold value of 18.7 μW. 119

Figure 6-30. Phonon lasing in different detuning conditions. (A) The threshold pump power for phonon lasing in the device (blue disks) follows the inverse trend of the differential spectral absorbance (magenta curve). (B) The phonon lasing results measured at the tuning voltage of 1.6 V, 2.7 V, and 3.5 V. The linewidth, mechanical amplitude, and mechanical output power all exhibit a transition at the threshold power. The output power data are fitted by equation (130), giving the threshold power for each condition. 120

Figure 6-31. Optomechanical cooling in the device tuned at 5.5 V. (A) The effective temperature of the mechanical mode, a character of energy, is reduced to below 50K by 210 μm laser pump power in the environment of 300 K. Inset: the mechanical resonance spectra and their Lorentzian fits for 56 μW and 210 μW laser pump powers exemplify the

reduction in mechanical energy, i.e. cooling, which is related to the area under the mechanical resonance peak. 123

Figure 7-32. An overview of the plasmo-thermomechanical IR detector (PlasMIRD). (A) A nanoslot antenna array is embedded in the gold layer of a bi-metalic beam structure. The IR radiation is converted into heat by the nanoantenna array and causes temperature increase in the bilayer structure. The increased temperature causes the bilayer structure to deflect due to the mismatch between the thermal expansion coefficients of the gold and silicon nitride layers. The bilayer beam is one of the two reflectors of a fiber optic Fabry-Perot interferometer (FFPI). The deflection of the bilayer beam is read out optically by the FFPI. (B) and (C) are the false color SEM images of the nanobeam and plasmonic nanoantennas.....128

Figure 7-33. The simulation and measurement of the resonant nanoslot plasmonic antennas (A) A unit cell of the studied nanoslot antennas etched into the gold layer with periodic boundary conditions. The thicknesses of the silicon nitride and metal layers are t_1 = 100nm and t_2 = 25nm, respectively (Ti / Au = 3nm / 22nm). b, The schematic diagram of the unit cell and the near field distribution in the slot. c, The typical measured absorption spectrum and the corresponding detector responsivity of the nanoslot antennas with p_x = p_y= 3μm, W = 100nm and L = 1.6μm. 130

Figure 7-34. The FEA simulation results for the heat transfer and mechanical deflection (A) The steady state temperature difference distribution ΔT along a bilayer beam under uniform infrared illumination and the corresponding line-scan at the center point. The total absorbed power P_{abs} = 1μW. (B) The temporal evolution of temperature increases ΔT_0 at the center of the beam. (C) The 2D distribution of steady state deflection z in a bilayer beam caused by the temperature increase. The bilayer beam is fixed at the two edges. (D) The steady state temperature increase ΔT_0 and the resulted mechanical deflection z_0 as a function of the absorbed power P_{abs}. 132

Figure 7-35. Characterization of the IR detector. (A) The schematic of the measurement system. (B) The normalized frequency response of the PlasMIRD measured using a modulated 405nm laser as the excitation. (C) The relationship between the response of the PlasMIRD at 1000 Hz and the input IR power. The vertical axis is the output voltage of the current to voltage converter, measured by the lock-in amplifier. The horizontal axis

is the IR power received by the nanobeam. (C) 1/f spectral density noise of the readout system. (D) The total bilayer noise density $\boldsymbol{p}_{bilayer}$, including thermal fluctuation noise, background fluctuation noise, and thermomechanical vibration noise (the red solid line), and the optical readout noise equivalent power $\boldsymbol{p}_{readout}$. (the blue solid line for $\eta_{PlasMIRD}$ =0.29 A/W and the black dash line for $\eta_{PlasMIRD}$ =2.9 A/W). 136

Figure 8-36. An overview of the LCMR sensor and its optical properties. (A) Schematic representation of a SiNW array on a glass substrate, oriented transverse to the light polarization. The graphene monolayer overlaid on the SiNW array facilitates the adsorption of various biomolecules. The array period, nanowire height, and width are denoted by Λ, H, and W, respectively. (B) SEM image of the 60° tilted SiNW array. The overall extent is 100 μm × 100 μm. (C) Magnified top view of SiNW array under SEM. The nanowires have a width of 140 nm, with a periodicity of 500 nm. (d) Photonic band diagram showing the reflection coefficient for the periodic SiNW array in the (ω, k_x) plane. The dashed lines correspond to analytically derived resonance positions for TE_{11} and TE_{12} mode. The parameters of the structure are Λ=500 nm, W=H=140 nm. The TE_{11} resonance remains the same up to k_x=0.5 μm^{-1} , corresponding to an incidence angle of ~48° and a numerical aperture of ~0.375, before diffractive effects become pronounced. 147

Figure 8-37. Size-dependent multicolor reflection of SiNW arrays. (A) Bright-field optical microscope images showing SiNW arrays of different widths, and constant NW interspacing of 350 nm. (B) The simulated electric field intensity distribution of TE_{11} leaky cavity mode for a typical nanowire array with $W \times H$=150 nm × **140** nm, Λ=500 nm at λ=765 nm. The near-field distribution along the broken line in (B) illustrates the strong field localization with sufficient modal overlap with the surrounding medium. (C) Measured normalized reflection coefficient under TE incident light for representative SiNWs with W=150 nm (green), 160 nm (red), 170 nm (blue), and 180 nm (orange). (D) The corresponding simulated reflection spectra of the same arrays. (E) FDTD calculated total quality factor (Q_{total}) and radiation quality factor (Q_{rad}) as functions of the cavity side length W.....151

Figure 8-38. Experimental bulk sensitivities of the LCMR sensor over a small index range. The sensitivities of the spectral shifts ($d\lambda/dn$) for the SiNW arrays with widths of 130, 140

nm are 171.94 nm/RIU, 213.41 nm/RIU, respectively. Error bars represent standard deviation of 4 individual arrays with identical sizes. 154

Figure 8-39. Demonstration of LCMR SiNW array in immunodetection. (a) Raman spectrum corresponds to the graphene covered area. Relative intensities of the G and 2D bands suggest monolayer graphene. Absence of a significant D peak further indicates that the graphene layer is of high quality and is largely defect free. (b) SEM image of SiNW arrays after loading with 100 nM of IgG protein. Dashed line sketches the boundary between the covered and non-covered areas. (c) Response of an A/G functionalized graphene covered LCMR sensor to IgG antibody with various concentrations, ranging from 30 pM to 300 nM. A/G on graphene serves as a specific binding intermediary while IgG antibodies are the target molecules. (d) Resonant wavelength shift in response to specific binding of IgG antibody with A/G protein on graphene enabled LCMR sensor for various concentrations. The wavelength shift is taken as the value ~30 min after buffer solution wash, the red curve is fitted using the Langmuir isotherm. The error bars present standard deviation values on the mean, for multiple measurements (n=4). Black circles below the detection limit (horizontal dashed line) show the negative control with nonspecific binding on to bare silicon surfaces. 155

PART A: PHONON LASING AND COOLING BY OPTICAL PUMP IN A PLASMONIC OPTOMECHANICAL DEVICE

CHAPTER 1: Introduction

1.1. Background

1.1.a. Optical Materials and Metamaterials

The material of choice has often symbolized the level of technology at that time in the long path of human civilization. Again and again, technological evolution took rapid accelerations after leaps in experience and knowledge on materials. Comparing iron and bronze to stone, the stronger materials with shapeablility had enabled advanced instruments of production [1] and inspired men to derive new materials with merits of desire. Steels, alloys of iron, carbon and other elements, possess even higher mechanical strength and ductility. It was the material that opened the doors to industrial revolution and modern urbanization. Modern metallurgy has been pushing the limit of performance of structural alloys and successfully empowered mankind to explore the outer space [2].

Our knowledge on optics was not as rich as that on mechanics in the early days, although visual perception plays a big role for a man since was born. One of the causes is that decent optical materials, like glass and crystal, were not easily available at that time. Thanks to the progress on techniques to purify and machine silica, microscopes and telescopes were two major inventions that had extended our vision on the scale of the universe [3]. The development of optical materials of required purity and quality is the foundation for the modern optical technologies [4]. Optical fiber, a long and thin shape of silica or plastic coated with cladding, allows the transmission of optical signals at high speed, in large bandwidth, and, the most important, with low loss, comparing to electrical signal transmission in copper cables. Fiber-optic communication technology had been indispensable in the advent of the information age. Despite optical materials and

technologies have already revolutionized the world, there is yet a great deal of applications to enhance and unknowns to explore.

Light is an example of electromagnetic wave, whose behaviors are hence governed by Maxwell's equations with given initial and boundary conditions including the electromagnetic properties of the materials. For a given wavelength of light, the most fundamental characteristic of a homogeneous medium is its refractive index n, which is defined by the ratio of the speed of light in vacuum to the phase velocity of light in the medium $n = \frac{c_0}{c}$.

Why does the propagation of light wave depend on media? How does the refractive index relate to media? Electromagnetic waves originate from the fact that a temporally changing magnetic field generates an electric field and, at the same time, a temporally changing electric field generates a magnetic field. This chain process depends on the interaction between the material and field. In general, the electromagnetic phenomena are the result of the interaction between the electric charges in the media and the applied electromagnetic field. Inside a medium placed in an electric field, the free charges or dipoles are driven by the electric field to migrate or reorient until reaching equilibrium. This process is called polarization. The result of such charge redistribution is the reduction or even complete cancellation of the external field. Depending on the density of the responsive charges and how easy they are able to travel, individual materials react differently to the field. The capability of polarization in a given material is quantified by the permittivity ε. In practice, the relative permittivity ε_r, which is defined by

normalizing the absolute permittivity to the vacuum permittivity ε_0, is more popularly used to characterize electromagnetic materials. In the case of static fields, the relative permittivity ε_r is widely known as the dielectric constant. Besides interactions with electric field, materials placed in a magnetic field undergo some microscopic dynamics as well. Magnetic moment, usually generated by the electric current in a closed-loop or the spin of element particles, e.g. electrons, protons, and neutrons, would reorient in a kinetically preferred manner. This process is called magnetization. Similarly, the degree of magnetic interaction in a given material depends on the availability of magnetic moments and how easily they are able to rotate. Permeability μ quantifies the ability of magnetization in a material. The relative permeability μ_r, which is similarly defined by normalizing the absolute permeability to the vacuum permeability μ_0, characterizes the other major property electromagnetic materials. Permittivity and permeability together determine electromagnetic phenomena inside a medium. Told by the solution of Maxwell's equations, the speed of light directly relates on the permittivity and permeability in the form of $c = 1/\sqrt{\varepsilon\mu}$. Therefore, the refractive index of a medium is represented by $n = \sqrt{\varepsilon\mu/\varepsilon_0\mu_0} = \sqrt{\varepsilon_r\mu_r}$.

Having known the permittivity and permeability of materials, we should be able to understand optical phenomena in any given systems. However, far more details still need taking into consideration. The previously described polarization and magnetization processes are actual microscopic dynamic actions with certain response time. As a result, their efficiency depends on the electromagnetic frequency. At very low frequency, the

migration of charge and the reorientation of electric dipole and magnetic moment occur almost instantly. At very high frequency, in contrast, these processes become sluggish because the charges, electric dipoles, and magnetic moments are unable to keep up the pace with the variance of the field. As a result, different polarization and magnetization mechanisms dominate at different frequency ranges. Instead of constants, the permittivity and permeability are functions of frequency, $\varepsilon(\omega)$ and $\mu(\omega)$, and so is the refractive index, $n(\omega)$. This phenomenon is termed as dispersion, whose very early application was to break up white light into rainbow colors. In the case that the response time is not negligible, the field inside the medium exhibits a phase delay on the external field. The delay is an important root of the electromagnetic absorption in materials, which will be discussed in the next section. Maxwell's equations and their solutions are able to keep the same shape by treating the permittivity and permeability as complex functions $\varepsilon(\omega)=\varepsilon'(\omega)+i\varepsilon''(\omega)$ and $\mu(\omega)=\mu'(\omega)+i\mu''(\omega)$. Derived from $n=\sqrt{\varepsilon_r\mu_r}$, a complex index of refraction is defined by $\tilde{n}(\omega)=n(\omega)+i\kappa(\omega)$, where the imaginary part $\kappa(\omega)$ is named extinction coefficient[1]. For common optical materials, the relative permeability is

[1] Depending on the choice of the complex field phasor, there are two conventions in symbols and equations in electromagnetism. Physicists uses $e^{-i\omega t}$ and $E=\mathrm{Re}\left(\tilde{E}e^{-i(\omega t-\tilde{\beta}z)}\right)$, while electrical engineers use $e^{+j\omega t}$ and $E=\mathrm{Re}\left(\tilde{E}e^{+j(\omega t-\tilde{\beta}z)}\right)$. In either way, the results are equivalent if exchanging $-i$ with $+j$, although mathematically $i=j\equiv\sqrt{-1}$. The complex index of refraction in electrical engineering convention is defined as $\tilde{n}(\omega)=n(\omega)-jk(\omega)$. The physics convention is used in this thesis.

very close to 1, because their interaction with high-frequency magnetic field is usually weak. Consequently, $\mu_r(\omega)=1$ is assumed for a common optical material that is nonmagnetic, and its complex index of refraction is related to the relative permittivity via $\tilde{n}(\omega)=\sqrt{\varepsilon_r'(\omega)+i\varepsilon_r''(\omega)}$.

Although the permittivity and permeability have been generalized to complex functions of frequency, there are even more to consider in order to describe all real materials. In this thesis, only linear and isotropic materials are of interest for discussion.

By extracting the permittivity and permeability of materials, we are able to explain the optical phenomena inside the media. In order to meet the functional needs, materials with certain permittivity and permeability are desired. Metamaterials are artificially engineered materials that are demonstrating unprecedented electromagnetic properties that cannot be obtained with conventional natural materials [5]. Metamaterials are fabricated by assembling elements of conventional materials into an array of repeating patterns at subwavelength scales. By choosing the base material and designing the structure, metamaterials are endowed with unconventional electromagnetic properties, the most typical one of which is negative refractive index. As a result of the special characteristics, metamaterials have realized applications including superlenses [6], which can image in a resolution beyond the diffraction limit, and cloaking [7], which hides an object from electromagnetic detection.

Owing to the invention of the scanning tunneling microscope (STM) and scanning force microscope (AFM) in the 1980s, atomic level of surface imaging and manipulation capabilities were realized for the first time. With the aid of the epoch-making technologies,

nanoscience and nanotechnologies started to boom [8] and have become the hottest topic of the contemporary research community. In recent years, nanofabrication technologies [9] had a great deal of progress and made it possible to create nanostructured metamaterials for optical wavelengths [5, 10]. The advances in fabrication and characterization technologies made it possible to study the behaviors of light in nanoscaled systems and manipulate light at nanoscales. It is not surprising that the new field hybridized by optics and nanoscience is named nanophotonics. At nanoscales, transmission and manipulation of light suffer from diffraction limit. Usually, optical energy cannot be retained in a small space whose dimensions are comparable to the wavelength. This limit had never been exceeded until the advent of the field of plasmonics. Plasmonics is the study of the coupling between light and surface plasmons, which are the collective oscillation of free carriers at the interface between two media with different signs in real permittivities, e.g. a metal and a dielectric. Plasmonic nanostructures can compress light into a sub-wavelength region and, consequently, create very strong local field that allows for very efficient light-matter interactions [11, 12]. As a very hot research topic in the past 15 years, plasmonics has realized a wide set of applications including High performance near-field optical microscopy, high-sensitivity chemical detection and biosensing, and high-speed optical circuits without diffraction limits [13, 14]. Besides these, optical absorbers based on plasmonic metamaterials [15-37] are able to demonstrate very large absorption efficiency with tunability and integrability. Plasmonic metamateial absorbers will be later discussed in details as a major topic.

1.1.b. Mechanical Effects of Light and Optomechanics

All electromagnetic waves carries energy as well as momentum. It is not surprising that the momentum of light may transfer, when light interacts with matter, and such momentum transfer results in a force exerted on the object. The most common and intuitive form of optical forces is the radiation pressure force. When a light beam is normally incident onto an object and then reflected partially or completely, the photons rebound and meanwhile push the object toward the incident direction. In the case of complete reflection on an object in vacuum or air, the radiation pressure force is about 6.7 pN per mW of input radiation power, which is equivalent to levitating just 25 human red blood cells [38]. Nevertheless, in a damping free environment with weak gravity, e.g. the outer space, the radiation pressure gives rise to comet tail formation and nebula evolution. In 2011, Japan Aerospace Exploration Agency (JAXA) successfully launched and deployed the IKAROS, a kite-like spacecraft that gains propulsion from the solar radiation. Besides radiation pressure, an optical field gradient also apply forces on objects placed in the gradient region. "Optical tweezers" originated from the strong electromagnetic field gradient near the focus of a laser beam have been widely used to trap and manipulate microscopic particles including living cells and bacteria. In dynamics, trapping microscopic particles even including molecules and atoms is realized by adding a restoring force against their motion, which actually removes their kinetic energy and cools them down. Drs. Steven Chu, Claude Cohen-Tannoudji, and William D. Phillips were honored with the Nobel Prize in Physics 1997, for developing the methods of laser cooling and trapping.

Optomechanics is the study of systems where light and mechanical objects interact and exchange energy. In an optomechanical system, optical resonances are coupled with

mechanical resonances, which offers a channel for energy transfer. On certain conditions, mechanical energy is decreased by such interaction and the mechanical oscillation is dampened. It is also possible that mechanical energy is increased and the mechanical oscillation is amplified. With no energy input, microscopic mechanical motions are often related to the Brownian motion, and an effective temperature is used to measure the intensity of the motion. Mechanical damping is called cooling, since lower energy is marked by lower effective temperature. Optomechanical effects will be later discussed in details.

In the past two decades, optomechanics and, specifically, cavity optomechanics have been extensively studied. Besides the deeper understanding on the mechanism of optical forces, the improved capability in fabricating and characterizing micro-scale optomechanical systems has served as the foundation. A typical cavity optomechanical system consists of an optical resonant cavity and a mechanical oscillator whose resonances are mutually influenced. Since optical forces are relatively small, the mechanical oscillator requires low mass and high quality factor (Q-factor). Microbeams, microtoroids, microdisks, nanomembranes, and nanorods are examples of successfully applied structures as mechanical oscillators, the masses of which range from micrograms to femtograms, and the Q-factors of which are as high as $\sim 10^6$ [39]. In fine optomechanical systems, the amplitude of mechanical motion is usually less than a nanometer and sometimes as small as a few femtometers. Although it is challenging to measure such weak mechanical motions, there are various schemes for this task. In optomechanical systems, the output signal of light is influenced by how much energy is lost in the optomechanical interaction. The

amount of energy transfer usually depends on the strength of optomechanical coupling, which is usually determined by the position of the oscillating mechanical element. With state-of-the-art photodetectors and amplifiers, the dynamic motions can be transduced to electric spectra and measured by a spectrum analyzer. Optic fibers has been previously discussed for their contributions in information communication. In addition, optic fibers have been a successful approach to precision sensing and measurement, which majorly utilizes interferometry [40]. The current state-of-the-art optical interferometric sensors are capable of detecting tiny deflection on the order of femtometers [41, 42].

Optomechanics is a successful example of fusing optics and mechanics with the aid of nanotechnologies. Plasmonic nanostructures can compress light to a very small region and create very strong local field, which allows for very efficient light-matter interaction. It is appealing to integrate plasmonics into optomechanics. We designed and fabricated an integrated plasmonic optomechanical device (Figure 1-1), and it demonstrated impressive optomechanical effects including coherent mechanical oscillation and optomechanical cooling by optical pump.

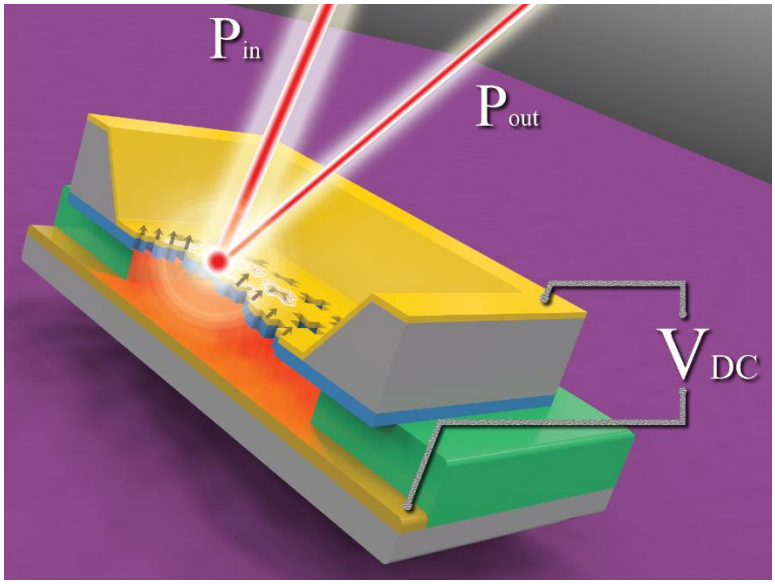

Figure 1-1. The schematic of the integrated plasmonic optomechancial device. A plasmonic metamaterial absorber made of gold thinfilm (yellow) on silicon nitride membrane (blue) with cross-shaped nano holes is free standing above a gold back reflector (yellow). The gap separating the membrane and back reflector is tunable by applying a bias voltage. A 1550 nm laser beam is normally incident onto the membrane and affects the vibration of the membrane. The reflected laser beam is used to detect the vibration.

This plasmonic optomechanical device consists of a suspended flexible plasmonic membrane and a conductive back reflector separated by an electrostatically tunable air gap. The membrane itself is a mechanical oscillator of high-Q factor, and the cavity between the membrane and reflector simultaneously supports optical resonances. Such optical resonances depend on the cavity length or the position of the membrane. When pumped with a 1550 nm laser, the membrane absorbs the light and is heated up, which generates a normal force on itself. The bilayered membrane has been engineered to yield maximum force on heating. As a result of this opto-thermo-mechanical effect, the vibration of the membrane is influenced by light. At the same time, the light absorption depends on the optical resonance and, therefore, it is influenced by the motion of the membrane. These

mechanisms demonstrate how optics and mechanics interact in the device. In this opto-thermo-mechanical coupling loop, the mechanical oscillator receives feedback from its motion. By applying a bias voltage, the optical resonance can be directly tuned near the wavelength of 1550nm. Depending on the direction of detuning, the optomechanical feedback can be positive or negative. Positive feedback works as optomechanical gain and amplifies the mechanical oscillation until phonon lasing, which becomes coherent mechanical oscillation if the optomechanical gain cancels the damping. Conversely, negative feedback adds optomechanical damping to the mechanical oscillator, which makes the oscillation inactive like molecules being cooled down. We have experimental demonstration of phonon lasing with a low pump threshold of 19 μW and optomechanical cooling of the mechanical resonances down to an effective temperature of 48 K. This optomechanical device integrated with plasmonic metamaterial absorber has the merits of free-space accessibility and broadband tolerance on optical pump source. As a new coherent acoustic phonon source, this device is expected to favor applications in fundamental research, novel sensors, and ultrasonic imaging modalities.

1.2. Light Absorption in Lossy Media

1.2.a. The Propagation of Light in Lossy Media

Unless it is a perfectly transparent medium that permits the passage of a light wave without any change in its intensity, the light intensity usually changes when it propagates through a medium. Such change could be either an increase or a decrease. The former happens in an active medium or gain medium, wherein the atoms or molecules can be excited to create a population inversion and have light radiation by stimulated emission.

Laser is the most important application built with active media. The latter takes place in a lossy medium, wherein the electromagnetic energy is converted, partially or completely, into the internal energy of the medium, e.g. the kinetic energy of vibration and rotation of molecules and atoms. The reduction in intensity of a light wave passing through a lossy medium is known as attenuation or extinction. The power of a medium to absorb light depends on several factors including the electronic structure of the molecules and atoms in the medium, the wavelength of the light, the distance for the light to travel in the medium. In special cases, electric or magnetic fields may change the light absorption, and examples are the Stark effect and the Zeeman effect.

The Lambert's law quantifies the light absorption in a homogeneous lossy medium: a monochromatic parallel beam of light of intensity I_0 traverses a length d in a homogeneous lossy medium is weaken to intensity $I = I_0 e^{-\alpha d}$, where α is the absorption coefficient of the medium at this wavelength. The absorption coefficient is the reciprocal of the length required for a light wave to traverse to attenuate to $1/e$ of the initial intensity.

1.2.b. Microscopic Mechanisms for Light Absorption

There is not a known medium opaque to all wavelengths of the light through infrared, visible, and ultraviolet, nor a known medium transparent to the complete spectrum of light. Absorption coefficients are usually wavelength dependent. A medium may be absorptive in a wide range of spectrum, while sometimes at specific wavelengths. For example, liquid water is transparent in visible but opaque in ultraviolet below 200 nm and infrared of long wavelength. Colored glasses exhibit selective absorption at the visible

wavelength and thus yield the appearance. To explain these phenomena, the physical nature of light absorption needs to be reviewed. In the microscopic picture, how an electromagnetic field interacts with materials is basically through electromagnetic forces applied on the electric charges inside the materials. Although materials are usually electrically neutral, they do have microscopic electric structures. There exist abundant free electrons in conductors such as metals, while there are no free charges but electric dipoles in insulators such as dielectric materials.

In dielectric materials, there exist electric dipoles. An electric dipole is a pair of positive and negative electric charges separated by a distance. There are many ways to form a dipole. Asymmetric covalent bond molecules may exhibit an imbalance of charge. This kind of molecules is called polar molecules. For instance, a water molecule has one negative oxygen atom is on one side of the molecule and two positive hydrogen atoms are on the other side, and this configuration creates a permanent dipole. In nonpolar molecules or atoms, especially with larger sizes, charges sometimes happen to be more concentrated unevenly in the molecule and form an instantaneous dipole. In the case of one molecule stays close to another polar molecule, a new dipole may be induced in the former by the latter. The kind of dipole is known as induced dipoles. In an electromagnetic field, dipoles feeling the electromagnetic forces cause the molecules, ions, and atoms to rotate and vibrate. Such kinetic energy is further dissipated by the collision and friction between the microscopic particles. The motion of molecules, ions, and atoms exhibits as heat and a rise in the temperature of the medium.

In metals, external electromagnetic field drives free electrons to accelerate and form electric currents. The electromagnetic energy is transduced into the kinetic energy of

free electrons. The accelerated electrons then undergo relaxation through collisions with larger and heavier atomic ions. These atomic ions pick up the kinetic energy of the electrons and vibrate more intensely, which exhibits as heating and a rise in the temperature of the medium. This electron relaxation mechanism is also the root of ohmic loss or Joule heating, the efficiency of which is determined by the conductivity σ. Although this is an important channel to dissipate electromagnetic waves, it is not efficient for light. At optical frequencies, electromagnetic waves hardly penetrate the conductor surface but usually get reflected back, leaving little chance for light-metal interactions, i.e. absorption. Optical behaviors in metals will be discussed in the next section.

In any materials, electron transitions are another channel for light absorption. In the quantum point of view, electromagnetic waves carry energy in the quantum of photons. The energy of a photon at frequency ν is $E = h\nu$. An electron bound to an atomic or a molecular orbit has a defined potential energy depending on the energy level. In an electromagnetic field, a bound electron can absorb an incoming photon of a specific energy and gets promoted from a lower energy level to a higher one. This absorption mechanism requires electromagnetic waves at coincident wavelengths, so it is a highly selective absorption. In most metals, the electron transition requires an energy of a couple of eVs, which lands in the spectral range of visible and UV (Table 1). In semiconductor heterojunctions, the carrier transition between valence band and conduction band requires an energy of about 1 eV, which corresponds to the spectral range of visible and IR. In addition to electron transition, rotational and vibrational modes of identical molecules also have precisely defined energies. When the electromagnetic wave matches those energies,

the molecules start to absorb resonantly, which also manifests a selective absorption character.

In conclusion, electromagnetic waves can be absorbed through dipole relaxation, free electron relaxation, and electron transition. The absorption profile can be broad band or selective. In real materials, some mechanism may dominate while the others also contribute depending on the structure of materials. In atomic gases, electron transition from a low energy level to a high one prevails the light-matter interaction, due to the lack of mechanical modes for the atoms with a simple geometry. As a result, atomic gases absorb light at very selective wavelengths, yielding line-shaped spectra. In molecular gases, there are more complicated vibrational and rotational modes in the molecules. As a result, molecular gases have broadened absorption lines. In liquids and solids, there are a lot of collisions going on between molecules and atoms. As a result, liquids and solids usually have continuous absorption bands over a wide spectral range. At ultraviolet frequencies, free electrons in metals cannot response instantaneously to the varying electromagnetic fields. As a result, metals usually behave like dielectrics and exhibit transparency at ultraviolet frequencies, except for absorption regions due to electron band transitions in transition metals such as gold and silver.

Table 1. Electromagneic spectrum, the classes and their ranges in wavelength, frequency, photon energy, and temperature of an equivalent blackbody whose radiation is peaked at the wavelength.

Spectral class	Wavelength	Frequency	Photon energy		Temperature of equivalent blackbody
γ-ray	10 pm	3.00×10^{7} THz	1.99×10^{-14} J	124 keV	2.90×10^{8} K
Hard X-ray	20 pm	1.50×10^{7} THz	9.93×10^{-15} J	62.0 keV	1.45×10^{8} K
Soft X-ray	10 nm	3.00×10^{4} THz	1.99×10^{-17} J	124 eV	2.90×10^{5} K
EUV	100 nm	3.00×10^{3} THz	1.99×10^{-18} J	12.4 eV	2.90×10^{4} K
UV	380 nm	789 THz	5.23×10^{-19} J	3.26 eV	7.63×10^{3} K
Violet	450 nm	666 THz	4.41×10^{-19} J	2.76 eV	6.44×10^{3} K
Blue	495 nm	606 THz	4.01×10^{-19} J	2.50 eV	5.85×10^{3} K
Green	570 nm	526 THz	3.48×10^{-19} J	2.18 eV	5.08×10^{3} K
Yellow	590 nm	508 THz	3.37×10^{-19} J	2.10 eV	4.91×10^{3} K
Orange	620 nm	484 THz	3.20×10^{-19} J	2.00 eV	4.67×10^{3} K
Red	750 nm	400 THz	2.65×10^{-19} J	1.65 eV	3.86×10^{3} K
Near IR	3 μm	100 THz	6.62×10^{-20} J	413 meV	966 K
Mid IR	50 μm	6 THz	3.97×10^{-21} J	24.8 meV	58.0 K
Far IR	1 mm	300 GHz	1.99×10^{-22} J	1.24 meV	2.90 K
Microwaves	1 m	300 MHz	1.99×10^{-25} J	1.24 μeV	2.90×10^{-3} K
Radio waves					

1.3. Optics of Linear, Homogeneous, Isotropic, and Nonmagnetic Metals[2]

1.3.a. Metal Conductivity at High Frequencies

The microscopic mechanisms of the interaction of metals with electromagnetic fields have been previously described. Experiences have told us metal are highly reflective at visible light frequencies. It is also true for low-frequency regime including microwaves and far-infrared. At near-infrared and visible frequencies, electromagnetic fields are easier

[2] This section is majorly sourced from reference [43] and [44] .

to penetrate into a metal, resulting in increased dissipation. Beyond visible frequencies, metals become dielectric media that can support the propagation of ultraviolet light waves. At low frequencies, permittivity ε is usually used to describe the response of electric dipoles to applied electric field in dielectric materials, while conductivity σ is usually used to describe how free electrons in metals form an electric current. However, at optical frequencies, both mechanisms work together. ε and σ at high frequencies are closely related to each other in metals. Analysis starting from Maxwell's equations

$$\nabla \cdot \vec{D} = \rho \tag{1}$$

$$\nabla \cdot \vec{B} = 0 \tag{2}$$

$$\nabla \times \vec{E} = -\frac{\partial \vec{B}}{\partial t} \tag{3}$$

$$\nabla \times \vec{H} = \vec{J} + \frac{\partial \vec{D}}{\partial t} \tag{4}$$

can help to quantitatively understand how metals response to light and how light behaves in metals. These equations link the four macroscopic electromagnetic fields $\vec{D}$ (the dielectric displacement), $\vec{B}$ (the magnetic induction), $\vec{E}$ (the electric field), and $\vec{H}$ (the magnetic field) with the electric charge and current densities ρ and $\vec{J}$. In linear, homogeneous, and isotropic materials, the field variables are halved by the constitutive relations

$$\vec{D} = \varepsilon \vec{E} \tag{5}$$

$$\vec{B} = \mu \vec{H} \tag{6}$$

The internal electric current density is linear to the electric field:

$$\vec{J} = \sigma \vec{E} \tag{7}$$

Use $-i\omega$ to replace $\frac{\partial}{\partial t}$ in equation (4) and decompose the electric current into the impressed current density $\vec{J}_i$ (existing from the beginning) and conduction electric current density $\vec{J}_c$ (caused by the electric field):

$$\nabla \times \vec{H} = \vec{J}_i + \vec{J}_c - i\omega \vec{D} \tag{8}$$

Inserting the constitutive relations (5) and (7) into (8) yields

$$\nabla \times \vec{H} = \vec{J}_i + \sigma_s \vec{E} - i\omega\varepsilon \vec{E} \tag{9}$$

where σ_s is the static conductivity of the metal and $\varepsilon = \varepsilon' + i\varepsilon''$ is the complex permittivity function of the metal. Now equation (9) transforms to

$$\nabla \times \vec{H} = \vec{J}_i + \left[\left(\sigma_s + \omega\varepsilon'' \right) - i\omega\varepsilon' \right] \vec{E} \tag{10}$$

and an effective conductivity is defined:

$$\sigma_e = \sigma_s + \omega\varepsilon'' \tag{11}$$

The effective conductivity consists of the static part σ_s and the alternating part $\omega\varepsilon''$. σ_s is attributed to free electrons, while $\omega\varepsilon''$ is attributed to the rotation of dipoles that are driven by the alternating electric field. Typical dielectric materials have very small σ_s and exhibit good insulator characters. However, in high-frequency alternating field, they have large $\omega\varepsilon''$ and behave as conductors. The electric current driven by the alternating field generates Joule heat, which explains the electromagnetic energy

dissipation in dielectric materials. It should be noticed that the alternating conductivity is related to the imaginary part of the complex permittivity.

1.3.b. Metal Permittivity Function at High Frequencies

In equation (10), there is a last electric current density term $-i\omega\varepsilon'\vec{E}$, named the displacement current density. Differed by $-i$ phase, the displacement current density is orthogonal to the conduction current density. Materials with $\sigma_e \ll \omega\varepsilon'$ are good dielectrics, wherein the total current is majorly displacement current. Materials with $\sigma_e \gg \omega\varepsilon'$ are good conductors, wherein the total current is majorly conduction current.

Besides the electric current interpretation, electromagnetic attenuation can also be explained by dielectric loss. Equation (4) can be reorganized into

$$\nabla \times \vec{H} = \vec{J}_i - i\omega\varepsilon'\left(1 + i\frac{\sigma_s + \omega\varepsilon''}{\omega\varepsilon'}\right)\vec{E} \tag{12}$$

and an effective loss tangent is defined by $\tan\delta_e = \frac{\sigma_s + \omega\varepsilon''}{\omega\varepsilon'}$.

The effective loss tangent comprise two parts, $\frac{\sigma_s}{\omega\varepsilon'}$ and $\frac{\varepsilon''}{\varepsilon'}$. The former is attributed to loss due to collisions of free electrons with atoms and ions, and the latter is attributed to loss due to rotation and friction of electric dipoles. Basically, the complex permittivity including the contribution by free electrons in an alternating field is found from equation (12):

$$\varepsilon = \varepsilon' + i\frac{\sigma_s + \omega\varepsilon''}{\omega} = \varepsilon' + i\frac{\sigma_e}{\omega} \tag{13}$$

In linear, homogeneous, isotropic, and nonmagnetic materials, the complex refractive index and relative permittivity have the relations:

$$\varepsilon_r' = n^2 - \kappa^2 \tag{14}$$

$$\varepsilon_r'' = 2n\kappa \tag{15}$$

$$n^2 = \frac{\varepsilon_r'}{2} + \frac{1}{2}\sqrt{\varepsilon_r'^2 + \varepsilon_r''^2} \tag{16}$$

$$\kappa = \frac{\varepsilon_r''}{2n} \tag{17}$$

The extinction coefficient κ determines the electromagnetic loss in the medium, and the origin is the imaginary part of the complex permittivity.

1.3.c. Light Dissipation in Metals

Taking the plain wave equation, a very common example of Maxwell's equations, for instance:

$$\nabla_r^2 \vec{E}(r,t) = \mu\varepsilon \frac{\partial^2 \vec{E}(r,t)}{\partial t^2} \tag{18}$$

The solution is a basic plain wave function

$$\vec{E}(\vec{r},t) = \vec{E}_0 e^{i(kr-\omega t)} \tag{19}$$

The scalarized wave vector $k = \omega\sqrt{\mu\varepsilon} = \frac{\omega}{c}\tilde{n} = \frac{\omega}{c}(n + i\kappa)$ can be used to reform the solution to yield

$$\vec{E}(\vec{r},t) = \vec{E}_0 e^{-\frac{\kappa\omega}{c}r} e^{i\left(\frac{n\omega}{c}r - \omega t\right)} \tag{20}$$

where the term $e^{-\frac{\kappa\omega}{c}r}$ determines the electromagnetic attenuation in the medium. The intensity attenuation is then known:

$$I \propto \left|\vec{E}\right|^2 \propto \left|\vec{E}_0\right|^2 e^{-\frac{2\kappa\omega}{c}r} \tag{21}$$

Comparing to Lambert's law, the absorption coefficient α is linked to the extinction coefficient κ via

$$\alpha = \frac{2\kappa\omega}{c} \tag{22}$$

Equations (11) (13) (16) and (17) reveals how the conductivity and the imaginary part of complex permittivity determine the absorption of electromagnetic waves in metals.

Derived from the Poynting vector $\vec{E} \times \vec{H}$, the dissipated power is represented by

$$\langle P_d \rangle = \iiint_v \vec{J} \cdot \vec{\mathrm{E}} dv = \frac{1}{2} \iiint_v \vec{J} \cdot \vec{\mathrm{E}}^* dv = \frac{1}{2} \iiint_v \sigma_e \left|\vec{\mathrm{E}}\right|^2 dv \tag{23}$$

The dissipated power density $\frac{1}{2}\sigma_e \left|\vec{\mathrm{E}}\right|^2$ is proportional to the square of electric field. Although it appears that the dissipated power is proportional to the effective conductivity, $\langle P_d \rangle$ actually does not increase with σ_e due to a further decrease in the electric field in a good conductor.

1.4. Plasmonics and Surface Plasmon Resonances[3]

1.4.a. Free Electron Gas in Metals

In metals, the outer electrons are delocalized and can move freely against heavier and almost immobile cations. The plasma model has successfully explained the optical behavior and dielectric function of metals, in which those electrons are treated as a gas. The plasma model assumes that free electrons are driven by a harmonically varying electric field $\vec{E}(t) = \vec{E}_0 e^{-i\omega t}$, oscillate with damping via electron-cation collisions, and manifest polarization depending on their displacement. Figure 1-2(A) depicts such oscillations, and the quanta of these electron oscillations are named bulk plasmons.

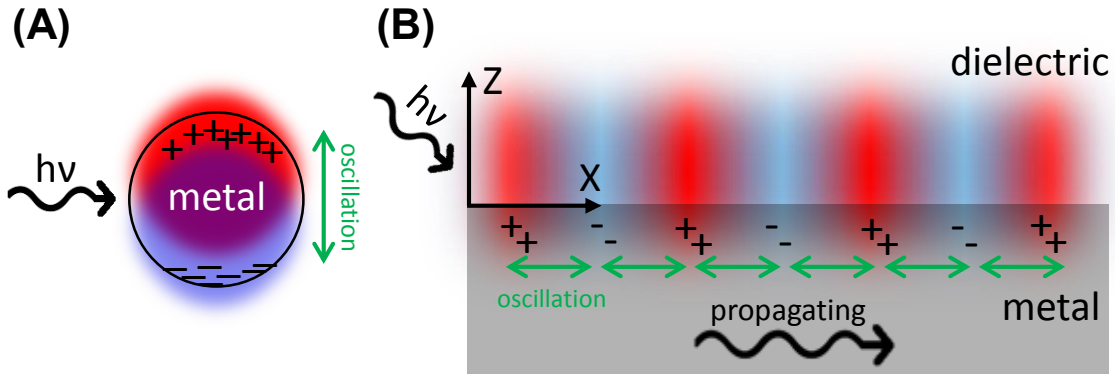

Figure 1-2. Electron oscillations in metals include (A) bulk plasmons which exist within the volume of a metal and (B) surface plasmons which exist only at the interface between a dielectric and a metal.

[3] This section is majorly sourced from reference [43] and [45].

Comparing the new total field to the driving field, the dielectric function of a free electron gas is given:

$$\varepsilon_r(\omega) = 1 - \frac{\omega_p^2}{\omega^2 + i\omega/\tau_e} = \left(1 - \frac{\omega_p^2 \tau_e^2}{1+\omega^2\tau_e^2}\right) + i\frac{\omega_p^2 \tau_e}{\omega\left(1+\omega^2\tau_e^2\right)} \tag{24}$$

where τ_e is the relaxation time and ω_p is the plasma frequency of the free electron gas. τ_e can represents the length of time for electrons to travel the distance of mean free path in the cation lattice and is usually on the order of 10 fs at room temperature. The plasma frequency is a character of metals. It is the resonance frequency of the oscillation of a free electron gas. Its value depends on the number density of electrons n_e and the (effective) mass of an electron m_e:

$$\omega_p^2 = \frac{n_e e^2}{\varepsilon_0 m_e} \tag{25}$$

Equation (24) predicts the dielectric function dispersion of metals. At high but below plasma frequency, where $\omega_p \tau_e > \omega\tau_e \gg 1$, equation (24) is reduced to a real function

$$\varepsilon_r(\omega) = 1 - \frac{\omega_p^2}{\omega^2} \tag{26}$$

Having a negligible imaginary permittivity, metals do not absorb any light at high frequencies. Alkali metals are good examples as they are transparent for ultraviolet light. However, noble metals encounter interband transitions and exhibit an increase in the imaginary permittivity. Having a negative real permittivity, metals' complex refractive index is usually predominantly imaginary, which results in complete reflection of light.

At very low frequencies, where $\omega\tau_e \ll 1$, equation (24) is reduced to

$$\varepsilon_r(\omega) = \left(1 - \omega_p^2 \tau_e^2\right) + i\frac{\omega_p^2 \tau_e}{\omega} \tag{27}$$

The imaginary part dominate over the real part of the complex permittivity, and metals are absorptive at thie region. Now, the real and imaginary part of the complex refractive index are of comparable magnitude:

$$n \approx \kappa \approx \sqrt{\frac{\varepsilon_r''}{2}} = \sqrt{\frac{\omega_p^2 \tau_e}{2\omega}} \tag{28}$$

Bring this back to equation (22), the absorption coefficient is found:

$$\alpha = \sqrt{\frac{2\omega_p^2 \tau_e \omega}{c^2}} \tag{29}$$

This equation can be rewritten using the static conductivity from Drude model $\sigma_s = \frac{n_e e^2 \tau_e}{m_e} = \omega_p^2 \tau_e \varepsilon_0$, yielding

$$\alpha = \sqrt{2\sigma_s \omega \mu_0} \tag{30}$$

This result suggests that the electromagnetic attenuation in metals at low frequencies is majorly caused by free electron acceleration and relaxation and, thus, can be described by the real static conductivity σ_s. As the frequency increases, κ becomes predominant in $\tilde{n}$ and σ_s acquires more and more complex character.

At very high frequencies, where $\omega\tau_e \gg \omega_p\tau_e \gg 1$, equation (26) tells $\varepsilon_r(\omega) \to 1$. However, it is not valid for noble metals such as gold and silver, since the inner d-band electrons have already coursed a polarized environment and constitute a residual

polarization $\varepsilon_{r,\infty}$ (usually valued between 1 and 10). Therefore, at frequencies above the plasma frequency $\omega > \omega_p$, equation (24) should be revised for noble metals:

$$\varepsilon_r(\omega) = \varepsilon_{r,\infty} - \frac{\omega_p^2}{\omega^2 + i\omega/\tau_e} \tag{31}$$

It should be noticed that the validity of equation (31) is still limited by the interband transition effect in noble metals at visible and ultraviolet regions, which leads to an increase in the imaginary part of $\varepsilon_r(\omega)$.

1.4.b. Surface Plasmon Polaritons

Besides bulk plasmons in the whole volume of a metal, there is a special class of electron oscillations only at the interface between a dielectric and a conductor, named surface plasmons (Figure 1-2(B)). While the electrons are oscillating, an electromagnetic wave at the same frequency as the electron oscillation is excited and propagating at the interface. This electron-photon excitation is called a surface plasmon polariton (SPP). Starting from Maxwell's equations at a single interface, shown in Figure 1-2(B), between a dielectric with relative complex permittivity $\varepsilon_{d,r}$ and a metal with relative complex permittivity $\varepsilon_{m,r}$, SPPs are described in the following solutions:

$$H_y(z) = Ae^{i\beta x}e^{-k_d z} \tag{32}$$

$$E_x(z) = \frac{iAk_d}{\omega\varepsilon_0\varepsilon_{d,r}}e^{i\beta x}e^{-k_d z} \tag{33}$$

$$E_z(z) = -\frac{A\beta}{\omega\varepsilon_0\varepsilon_{d,r}}e^{i\beta x}e^{-k_d z} \tag{34}$$

for the dielectric space $z > 0$ and

$$H_y(z) = Ae^{i\beta x}e^{-k_m z} \tag{35}$$

$$E_x(z) = -\frac{iAk_m}{\omega\varepsilon_0\varepsilon_{m,r}}e^{i\beta x}e^{-k_m z} \tag{36}$$

$$E_z(z) = -\frac{A\beta}{\omega\varepsilon_0\varepsilon_{m,r}}e^{i\beta x}e^{-k_m z} \tag{37}$$

for the metal space $z < 0$. k_d and k_m are the perpendicular components of the wave vector, and β is the propagation constant. The above equations indicate that SPPs are TM waves propagating along x direction. SPPs are trapped at the interface, for the fields decay exponentially as leaving the $z = 0$ plane. The evanescent decay length is defined by the reciprocal of the perpendicular wave vector, $1/|k_d|$ and $1/|k_m|$. The wave vectors are related to the wave vector in vacuum k_0 and the propagation constant β via

$$k_d^2 = \beta^2 - k_0^2\varepsilon_{d,r} \tag{38}$$

$$k_m^2 = \beta^2 - k_0^2\varepsilon_{m,r} \tag{39}$$

The continuous condition of the magnetic field at $z = 0$ requires

$$\frac{k_d}{k_m} = -\frac{\varepsilon_{d,r}}{\varepsilon_{m,r}} \tag{40}$$

Equation (40) indicates that SPPs exist only at interfaces of media with opposite signs of permittivities, such as dielectric-conductor. Fields decay faster in the metal space, for usually $|\varepsilon_{m,r}| > |\varepsilon_{d,r}|$ and consequently $k_m > k_d$. In other words, the fields extend further

into the dielectric space than the metal space. By combining equations (38-40), the dispersion relation of SPPs is found:

$$\beta = k_0 \sqrt{\frac{\varepsilon_{m,r}\varepsilon_{d,r}}{\varepsilon_{m,r} + \varepsilon_{d,r}}} \tag{41}$$

Equation (41) indicates that there exists an intrinsic momentum mismatch between SPPs and photons in free space, because $\beta > k_0$ for dielectric-metal combination. Introducing equation (26), in the limit of large wave vector, $\beta \to \infty$ or $\varepsilon_{m,r}(\omega) + \varepsilon_{d,r} = 0$, the frequency of SPPs also approaches a limit:

$$\omega_{sp} = \frac{\omega_p}{\sqrt{1 + \varepsilon_{d,r}}} \tag{42}$$

which is named surface plasmon frequency.

Equation (41) is still valid for complex permittivities, i.e. for lossy media. In that case, the propagation constant β has a complex value, wherein the imaginary part leads to attenuation along x direction. $1/2\,\mathrm{Im}(\beta)$ is defined as the propagation length of SPPs in lossy media. Good candidates of plasmonic materials require a large negative real part and a small imaginary part of the complex permittivity, which, respectively, correspond to high conductivity and low loss. Based on these criteria, the best known plasmonic materials are silver, gold, and aluminum. Sodium and potassium possess the same plasmonic qualities and are free of interband transitions at high-frequencies, but it is difficult to process alkali metals [46]. Taking air-silver combination for instance, at the frequency of 450 nm wavelength light in free space, SPPs have propagation length of ~16 μm and dielectric

evanescent decay length of ~180 nm. At 1.5 μm, due to less loss and larger $\left|\mathrm{Re}\left(\varepsilon_{m,r}\right)\right|$, SPPs have propagation length of ~1080 μm and dielectric evanescent decay length of ~2.6 μm. The evanescent decay length in metal space is ~20 nm over these frequencies [43].

Owing to the intrinsic momentum mismatch, SPPs can neither be excited by photons in the air nor emit photons to the air. Despite this, there are several ways to excite SPPs at planar interfaces, by using prisms, gratings, or even surface roughness. These, in turn, can also serve as the methods to couple SPPs into light.

1.4.c. Localized Surface Plasmons

In addition to SPPs, there is a non-propagating version existing in metallic nanoparticles and nanoshells of sub-wavelength dimensions, called localized surface plasmons (LSPs). Due to the non-planar geometry of the dielectric-metal interfaces on nanoparticles, the excitation of LSPs can be fulfilled by direct light illumination. As a result of geometric confinement in nanoparticles, LSPs reach resonances at certain frequencies, causing strong extinction of light. The resonance also leads to field enhancement in the near-field area, which amplifies the light-matter interaction in that area.

Plasmonic resonances are extremely sensitive to the refractive index at the interface area, so they are powerful in refractive sensing applications, wherein the resonance changes if the refractive index varies. Based on this, plasmonic chemical sensors and bio-sensors are of great interest. The local field enhancement enables promising applications in spectroscopy, imaging, photovoltaic, and thermally assisted technologies. Theoretical framework of optical nanocircuits based on plasmonic nanoparticles and metamaterials has

been developed [14]. Comparing to the wavelength of the light at the same frequency, surface plasmons reside in an area of sub-wavelength dimensions. Although electronic devices are sized in nano-scales, the speed is limited to below 10 GHz by heat generation and interconnect delay time issues. Plasmonics can serve as a bridge to link photonics and nanoelectronics, and pave a way to faster, smaller, and more efficient electronics [13].

1.5. Cavity Optomechanics

1.5.a. Optical and Mechanical Resonance Coupling

A cavity optomechanical system is typically composed of an optical cavity and a mechanical oscillator (Figure 1-3). An optical cavity, e.g. a Fabry-Perot (FP) cavity, can retain photons which travel back and forth until leaking out. If the cavity length meets the standing wave condition for the light, the density of photons in this cavity would be boosted. This situation is the so-called resonance. Resonant photons have a lifetime long enough to interact with the cavity medium as well as the end mirrors. The former is a necessary condition for lasers, and the latter provides the possibility of optomechanical coupling.

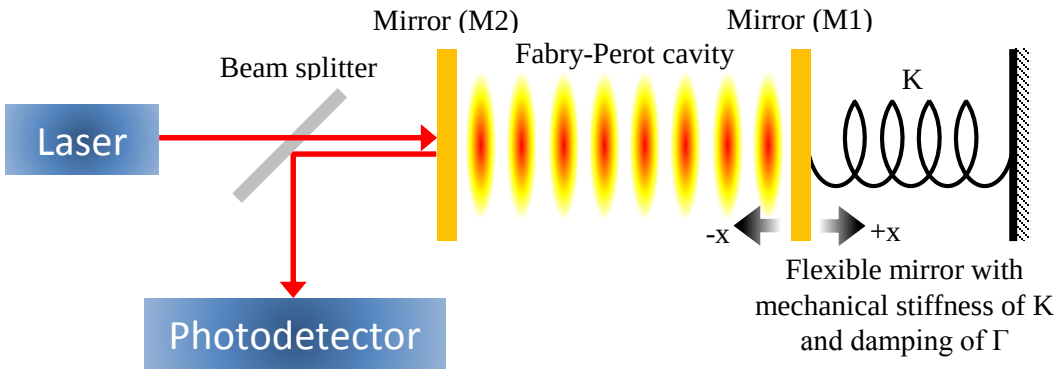

Figure 1-3. The schematic of a typical optomechanical system based on a Fabry-Perot cavity between the flexible end mirror (M1) and the fixed end mirror (M2).

The optomechanical coupling effects include the influence on photon density in the cavity and the optical force exerted on the mirrors. A probe laser resonantly couples into a FP cavity with one flexible end mirror (M1 in Figure 1-3) and the frequencies of the probe laser and the cavity resonance are ω_L and ω_C respectively. If the cavity length ever varies by any means, the optical resonance would be detuned and the photon density in the cavity would decrease (Figure 1-4(A)). In the situation, an enhanced reflection signal would be observed at the output port. This is the basic for optomechanical switches and amplitude modulator. If M1 vibrates along the cavity axis, the photon density will be varying accordingly, leading to an oscillating optical intensity signals at the output port which is transduced from the mechanical displacement (Figure 1-4(B)). This principle allows to detect very weak mechanical motions. The best displacement sensitivity achieved by using this technique can exceed $10^{-19} m/\sqrt{Hz}$ for gravitational wave detection research [47]. If M1 oscillates harmonically at the frequency of Ω_m, the photon density frequency spectrum with the peak at ω_L would split into three bands with frequencies of $\omega_L - \Omega_m$, ω_L, and

$\omega_L + \Omega_m$ due to Doppler effect (Figure 1-4(C)). This is the basic for optomechanical frequency modulators. If the cavity is detuned from $\omega_C = \omega_L$, the Doppler sidebands would become asymmetric (Figure 1-4(D) and (E)).

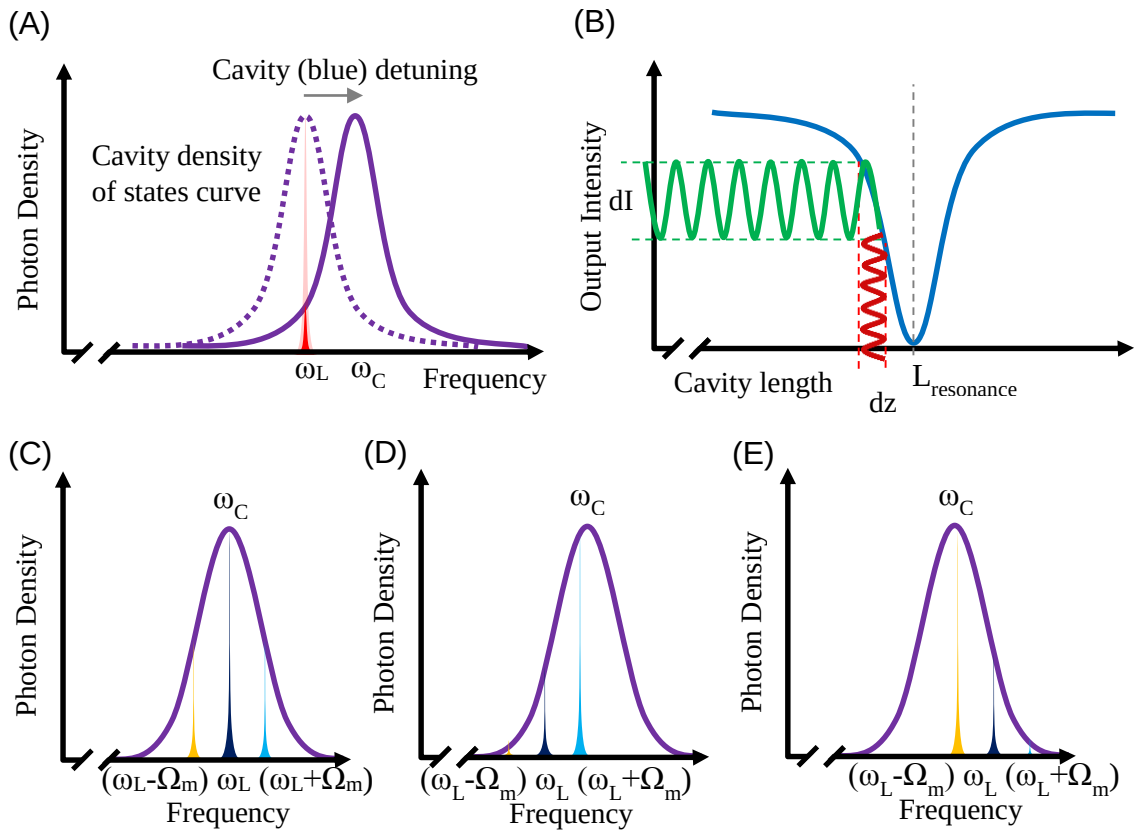

Figure 1-4. Varying cavity lengths influence optical resonances. The broad spectra correspond to optical cavity resonances, and the narrow spectra correspond to laser lines. (A) The cavity length change (shortened) leads to detuning. (B) The mechanical motion of the end mirror modulates optical response. (C) Sidebands are generated by Doppler shift. Asymmetric sidebands occur because of (D) blue detuning or (E) red detuning of the cavity.

The aforementioned discussion only considered that the optical resonance is able to response instantaneously to the cavity length change. In practice, the response speed is

substantially limited by the lifetime of in-cavity photons. The Q-factor of an optical cavity is the character of the optical resonance as well as the indicator of the average period of time for a photon to live in the cavity. In a high-Q cavity, the resonant photons undergo many roundtrips between the end mirrors before escaping. Once the cavity is detuned, it takes a finite period of time for the photons to achieve equilibrium when the entering and exiting rates of photons are balanced. Therefore, the modulator cannot respond faster than the relaxation time of the cavity. Although low-Q cavities have short relaxation time, the signal-to-noise ratio is also sacrificed. An optimized design should be found to balance the factors.

1.5.b. Optomechanical Effects: in the Perspective of Forces

In the mechanical perspective, the end mirrors are subjected to the radiation pressure force, which is proportional to the photon density in the cavity. The optical force decreases as a result of resonance detuning. If M1 oscillates harmonically, the optical force would co-vary with the photon density. Assuming that M1 has been blue-detuned (Figure 1-4(A) and (D)) at beginning, the optical force is weaker when M1 is at the position of -z (cavity is further blue-detuned) but stronger when M1 is at the position of +z (cavity is less blue-detuned). Taking the optical force at the balance position as zero reference, the optical force manifests an elastic restoring force at a small displacement. This optomechanical coupling effect acts as an optical spring [48] on M1, adding an extra stiffness onto the intrinsic mechanical stiffness and leading to an increase in the mechanical eigenfrequency. In the opposite scenario that the mirror starts at the red-detuned position (Figure 1-4(E)), the optical force is stronger when M1 is at position of -z (cavity less red-detuned) but

weaker when M1 is at position of +z (cavity further red detuned). This is equivalent to a negative optical spring constant, which undermines the intrinsic mechanical stiffness of M1 and leads to a decrease in the mechanical eigenfequency.

The photon-induced stiffness is the only optomechanical phenomenon only if the photon response is instantaneous. On the condition that the cavity relaxation time is non-negligible, the optical resonance exhibits a finite delay in response time. When the cavity delay time is comparable or even longer then the mirror oscillation period, a dynamic backaction on the vibrating mirror emerges and induces either damping or amplifying feed-back to M1 [47]. References [49] and [50] have provided a delayed force model to explain this phenomenon. The delay in cavity response leads to the delay in force with respect to a sudden change of M1 position. The delayed force acted on M1 can be modeled as a convolution of the force changing rate $\frac{dF_{om}\left[x(t)\right]}{dt}$ and a response function $h(t)$:

$$\bar{F}_{om}\left[x(t)\right]=\int_0^t \frac{dF_{om}\left[x(t')\right]}{dt'}h(t-t')dt' \tag{43}$$

Then, the equation of motion describing the oscillation of M1 is

$$m\frac{d^2x}{dt^2}+m\Gamma_{m,0}\frac{dx}{dt}+K_{m,0}x=F_{dr}(t)+\int_0^t \frac{dF_{om}\left[x(t')\right]}{dt'}h(t-t')dt' \tag{44}$$

where m is the effective mass of M1, $\Gamma_{m,0}$ is the intrinsic mechanical damping, $K_{m,0}$ is the intrinsic mechanical stiffness, and $F_{dr}(t)$ is the effective driving force exerted on the mirror oscillator, e.g. the effective thermal noise force to drive the Brownian motion. The response function of the delayed force is an exponential formalism: $h(t)=1-e^{-t/\tau_c}$, where

τ_c is the cavity relaxation time constant. Treating equation (44) by Laplace transform, the equation of motion is reformulated:

$$-m\omega^2 x_\omega + i\omega m\Gamma_{m,eff} x_\omega + K_{m,eff} x_\omega = F_{dr,\omega} \tag{45}$$

where the effective spring constant is

$$K_{m,eff} = K_{m,0}\left(1 - \frac{1}{1+\omega^2\tau_c^2}\cdot\frac{\nabla F_{om}}{K_{m,0}}\right) \tag{46}$$

and the effective damping is

$$\Gamma_{m,eff} = \Gamma_{m,0}\left(1 + Q_M\,\frac{\omega_0\tau_c}{1+\omega^2\tau_c^2}\cdot\frac{\nabla F_{om}}{K_{m,0}}\right) \tag{47}$$

where $\omega_0 \equiv \sqrt{\frac{K_{m,0}}{m}}$ is the mechanical eigenfrequency and $Q_M \equiv \frac{\omega_0}{\Gamma_{m,0}}$ is the mechanical Q-factor [50].

An optomechanical modification on the effective spring constant is due to an elastic backaction force. In the limit of small displacement, ∇F_{om} indicates such a force. On the condition that F_{om} is delayed by $\sim\tau_c$, the damping is modified by the delayed optomechanical force. This condition is proved by equation (47), wherein $\Gamma_{m,eff} = \Gamma_{m,0}$ if $\tau_c = 0$. Equations (46) and (47) also reveals that the trend (increase or decrease) of optomechanical modifications is determined by the sign of ∇F_{om}, which depends on the direction of the cavity detuning.

The modification on the damping attributes to the most fascinating optomechanical phenomena. When the damping is increased, the oscillation exhibits a smaller amplitude,

which is called optomechanical cooling. The term “cooling” has been adopted to cavity optomechanics because the energy of a small mechanical oscillator can be conveniently characterized by the effective temperature T_{eff} of an equivalent quantum oscillator $E = k_B T_{eff}$. When the damping is decreased, the oscillation is amplified, which is called optomechanical self-oscillation. At the point when the effective damping reaches zero, i.e. the mechanical oscillation becomes friction-free, phonon lasing or coherent oscillation would occur. To achieve maximum modification on the mechanical damping, τ_c should be close to the mechanical oscillation period so that $\tau_c \omega_0 \approx 1$.

Optomechanical cooling or amplification occurs depending on the energy flow direction between the optical mode and mechanical mode, which is determined by the cavity detuning direction. The process is analogous to Raman scattering. In Figure 1-4(D), the cavity is blue-detuned and the anti-Stokes optical mode is stronger than the Stokes optical mode, which means the photons have gained energy out of the cavity. Such energy must come from the mechanical mode. Therefore the mechanical oscillation is dampened. Figure 1-4(E) illustrates the red-detuned cavity, and, in contrast, the Stokes band is stronger than the anti-Stokes band, which indicates the photons have given energy to the cavity. Similarly, this explains how the mechanical oscillation is amplified.

There have been numerous experimental studies on optomechanical cooling effect [49-52]. Cooling of a micromirror down to effective temperature of about 10 K has been demonstrated [51]. On the other hand, the opposite effect, particularly the zero-damping case, has not drawn much attention. There are a few experimental and theoretical works reported [53-56] yet no systematic and comprehensive study about phonon lasing.

It is rare to refer to optomechanical self-oscillation as "optomechanical heating", because the heating effect is universal in practical optomechanical cavity systems and it is confusing to simultaneously discuss the concepts of mirror heating and oscillator heating. In practical optomechanical devices, the flexible mirrors are usually tiny and of small thermal capacitance. They may be easy to deform once heated up by the light illumination. Such deformation leads the displacement of the mirror and a force. This opto-thermo-mechanical force can be treated the same way as a radiation pressure force in the equation of motion (44), except that the opto-thermo-mechanical force is always delayed since the thermomechanical process is relatively slow. Taking into account all possible contributions to the photo-induced force, the optomechanical force $F_{om}\left[x(t)\right]$ changes to the sum of them all: $F_{om}\left[x(t)\right]=\sum_n F_{om,n}\left[x(t)\right]$. Now the equation of motion is generalized to consider all types of photo-induced forces:

$$m\frac{d^2x}{dt^2}+m\Gamma_{m,0}\frac{dx}{dt}+K_{m,0}x=F_{dr}(t)+\sum_n\int_0^t\frac{dF_{om,n}\left[x(t')\right]}{dt'}h_n(t-t')dt' \tag{48}$$

Since this is a linear differential equation, the new solution is the superposition of the solutions with each type of force, yielding the modified mechanical oscillation:

$$K_{m,eff}=K_{m,0}\left(1-\sum_n\frac{1}{1+\omega^2\tau_{c,n}^2}\cdot\frac{\nabla F_{om,n}}{K_{m,0}}\right) \tag{49}$$

$$\Gamma_{m,eff}=\Gamma_{m,0}\left(1+Q_M\sum_n\frac{\omega_0\tau_{c,n}}{1+\omega^2\tau_{c,n}^2}\cdot\frac{\nabla F_{om,n}}{K_{m,0}}\right) \tag{50}$$

The photon-induced forces, if there exist several ones, work together or compete against each other to determine the optomechanical modifications in a system. The force

intensity, force gradient, force delay time constant, and the mechanical Q-factor are all determining factors on the optomechanical effects, which is told by equations (49) and (50). For radiation pressure forces, the intensity and delay depend on the Q-factor of the optical cavity. In a FP cavity, the Q-factor is related to the finesse and cavity length by $Q = \frac{nL}{\lambda}\mathcal{F}$. The finesse $\mathcal{F}$, measuring how many times a photon is reflected by the mirrors until it escapes, is determined by the reflectivity of the end mirror ($\mathcal{F} \approx \frac{\pi\sqrt{R}}{1-R}$). At a particular wavelength, photons traverse more roundtrips in a cavity with highly reflective end mirrors. Photons also spend longer time on each roundtrip inside a longer cavity. Hence, a high-Q optical cavity supports a longer photon lifetime and, consequently has a larger cavity relaxation time constant. This is a helpful guide to design a proper cavity. In some systems, opto-thermo-mechanical forces are much stronger than radiation pressure forces and, hence, can be treated as the sole contributor to the optomechanical effects.

Generally, radiation pressure forces require high-Q optical cavities to achieve strong optomechanical effects. For opto-thermo-mechanical forces, the intensity depends on the opto-thermal conversion efficiency and the delay depends on the thermal conductance.

1.5.c. Optomechanical Effects: in the Perspective of Energy

The optomechanical force can be analyzed in an energetic system perspective [57]. In the eigenmode of an optical cavity, the total stored energy is $U = N\hbar\omega$, where N is the population of the photons of the frequency of ω. An adiabatic mechanical displacement

of the mirror $\Delta\xi$ induces the shift of optical eigenmode frequency by $\Delta\omega$. The change in optical eigenfrequency causes the change in energy, which equals to the work done by the optomechanical force:

$$F_{om} = -\frac{dU}{d\xi} = -\frac{d\left(N\hbar\omega\right)}{d\xi} = -N\hbar\frac{d\omega}{d\xi} = -\frac{U}{\omega}\frac{d\omega}{d\xi} \tag{51}$$

$\frac{d\omega}{d\xi}$ represents how much the eigenfrequency shifts with respect to the mechanical perturbation, and is defined as the optomechanical coupling coefficient $g_{OM} \equiv \frac{d\omega}{d\xi}$, which is a general character of the coupling strength in optomechanical systems. Equation (51) suggests that the optomechanical force is proportional not only to g_{OM} but also to the total energy of the optical mode, which can be built up by high power input light and a high Q-factor cavity.

1.6. Thesis Outline

In this thesis, my work on optomechanical devices and sensors based on plasmonic and nanophotnic structures is summarized. Except for the general introduction in CHAPTER 1:, the plasmonic optomechanical device that demonstrates phonon lasing and cooling by optical pump is discussed in PART A. At first, optical absorbers, my focus of interest in the field of metamaterials and plasmonics, are explored in CHAPTER 2:. In this optomechanical device, plasmonic metamaterial absorber is built on the silicon nitride membrane, which meanwhile serves as the mechanical oscillator (CHAPTER 3:). With the optical and mechanical elements ready, CHAPTER 4: explains the coupling between the

optical and mechanical modes. The device fabrication and validation before the optomechanical test are documented in CHAPTER 5:. The most exciting results about phonon lasing and optomechanical cooling in the device are finally presented in CHAPTER 6:.

The second part of the thesis is about sensing applications of novel plasmonic and nanophotonic devices, where two major projects are documented, including infrared sensors based on thermomechanical plasmonic membranes in CHAPTER 7: and biosensor based on silicon leaky cavity mode resonances in silicon nanowires in CHAPTER 8:.

1.7. References

1. Brown, H.T., *507 mechanical movements*. 2005, Mineola, N.Y.: Dover. 122 p.
2. Mouritz, A.P., *Introduction to aerospace materials*. AIAA education series. 2012, Reston, VA; Cambridge, UK: American Institute of Aeronautics and Astronautics; Woodhead Pub. xiv, 621 p.
3. Doak, R.S., *The telescope and microscope*. Great inventions. 2005, Milwaukee: World Almanac Library. 48 p.
4. Glass, A.M., *Optical-Materials.* Science, 1987. **235**(4792): p. 1003-1009.
5. Shalaev, V.M., *Optical negative-index metamaterials.* Nature Photonics, 2007. **1**(1): p. 41-48.
6. Zhang, X. and Z.W. Liu, *Superlenses to overcome the diffraction limit.* Nature Materials, 2008. **7**(6): p. 435-441.
7. Alu, A. and N. Engheta, *Achieving transparency with plasmonic and metamaterial coatings.* Physical Review E, 2005. **72**(1).
8. Drexler, K.E., *Engines of creation*. 1st ed. 1986, Garden City, N.Y.: Anchor Press/Doubleday. xii, 298 p.
9. Stepanova, M. and S. Dew, *Nanofabrication : techniques and principles*. 2012, Wien ; New York: Springer. viii, 344 p.
10. Zhang, S., et al., *Experimental demonstration of near-infrared negative-index metamaterials.* Physical Review Letters, 2005. **95**(13).

11. Barnes, W.L., A. Dereux, and T.W. Ebbesen, *Surface plasmon subwavelength optics.* Nature, 2003. **424**(6950): p. 824-830.

12. Gramotnev, D.K. and S.I. Bozhevolnyi, *Plasmonics beyond the diffraction limit.* Nature Photonics, 2010. **4**(2): p. 83-91.

13. Brongersma, M.L. and V.M. Shalaev, *APPLIED PHYSICS The Case for Plasmonics.* Science, 2010. **328**(5977): p. 440-441.

14. Engheta, N., *Circuits with light at nanoscales: Optical nanocircuits inspired by metamaterials.* Science, 2007. **317**(5845): p. 1698-1702.

15. Landy, N.I., et al., *Perfect metamaterial absorber.* Physical Review Letters, 2008. **100**(20).

16. Tao, H., et al., *A metamaterial absorber for the terahertz regime: Design, fabrication and characterization.* Optics Express, 2008. **16**(10): p. 7181-7188.

17. Landy, N.I., et al., *Design, theory, and measurement of a polarization-insensitive absorber for terahertz imaging.* Physical Review B, 2009. **79**(12).

18. Avitzour, Y., Y.A. Urzhumov, and G. Shvets, *Wide-angle infrared absorber based on a negative-index plasmonic metamaterial.* Physical Review B, 2009. **79**(4).

19. Hao, J.M., et al., *High performance optical absorber based on a plasmonic metamaterial.* Applied Physics Letters, 2010. **96**(25).

20. Liu, X.L., et al., *Infrared Spatial and Frequency Selective Metamaterial with Near-Unity Absorbance.* Physical Review Letters, 2010. **104**(20).

21. Liu, N., et al., *Infrared Perfect Absorber and Its Application As Plasmonic Sensor.* Nano Letters, 2010. **10**(7): p. 2342-2348.

22. Alici, K.B., et al., *Experimental verification of metamaterial based subwavelength microwave absorbers.* Journal of Applied Physics, 2010. **108**(8).

23. Wu, C.H., et al., *Large-area wide-angle spectrally selective plasmonic absorber.* Physical Review B, 2011. **84**(7).

24. Tittl, A., et al., *Palladium-Based Plasmonic Perfect Absorber in the Visible Wavelength Range and Its Application to Hydrogen Sensing.* Nano Letters, 2011. **11**(10): p. 4366-4369.

25. Aydin, K., et al., *Broadband polarization-independent resonant light absorption using ultrathin plasmonic super absorbers.* Nature Communications, 2011. **2**.

26. Cui, Y.X., et al., *A thin film broadband absorber based on multi-sized nanoantennas.* Applied Physics Letters, 2011. **99**(25).

27. Zhu, H., F. Yi, and E. Cubukcu, *Nanoantenna Absorbers for Thermal Detectors.* Ieee Photonics Technology Letters, 2012. **24**(14): p. 1194-1196.

28. Cui, Y.X., et al., *Ultrabroadband Light Absorption by a Sawtooth Anisotropic Metamaterial Slab.* Nano Letters, 2012. **12**(3): p. 1443-1447.

29. Wang, Y., et al., *Metamaterial-Plasmonic Absorber Structure for High Efficiency Amorphous Silicon Solar Cells.* Nano Letters, 2012. **12**(1): p. 440-445.

30. Fang, Z.Y., et al., *Tunable wide-angle plasmonic perfect absorber at visible frequencies.* Physical Review B, 2012. **85**(24).

31. Cui, Y.X., et al., *Multiband plasmonic absorber based on transverse phase resonances.* Optics Express, 2012. **20**(16): p. 17552-17559.

32. Watts, C.M., X.L. Liu, and W.J. Padilla, *Metamaterial Electromagnetic Wave Absorbers.* Advanced Materials, 2012. **24**(23): p. Op98-Op120.

33. Wu, C.H., et al., *Metamaterial-based integrated plasmonic absorber/emitter for solar thermo-photovoltaic systems.* Journal of Optics, 2012. **14**(2).

34. Yi, F., et al., *Voltage tuning of plasmonic absorbers by indium tin oxide.* Applied Physics Letters, 2013. **102**(22).

35. Cheng, Y.Z., et al., *Ultrabroadband Plasmonic Absorber for Terahertz Waves.* Advanced Optical Materials, 2015. **3**(3): p. 376-380.

36. Walter, R., et al., *Large-Area Low-Cost Tunable Plasmonic Perfect Absorber in the Near Infrared by Colloidal Etching Lithography.* Advanced Optical Materials, 2015. **3**(3): p. 398-403.

37. Brongersma, M.L., N.J. Halas, and P. Nordlander, *Plasmon-induced hot carrier science and technology.* Nature Nanotechnology, 2015. **10**(1): p. 25-34.

38. Phillips, K.G., S.L. Jacques, and O.J.T. McCarty, *Measurement of Single Cell Refractive Index, Dry Mass, Volume, and Density Using a Transillumination Microscope.* Physical Review Letters, 2012. **109**(11).

39. Aspelmeyer, M., T.J. Kippenberg, and F. Marquard, *Cavity optomechanics.* Reviews of Modern Physics, 2014. **86**(4): p. 1391-1452.

40. Culshaw, B. and A. Kersey, *Fiber-optic sensing: A historical perspective.* Journal of Lightwave Technology, 2008. **26**(9-12): p. 1064-1078.

41. Hoogenboom, B.W., et al., *A Fabry-Perot interferometer for micrometer-sized cantilevers.* Applied Physics Letters, 2005. **86**(7).

42. Rasool, H.I., et al., *A low noise all-fiber interferometer for high resolution frequency modulated atomic force microscopy imaging in liquids.* Review of Scientific Instruments, 2010. **81**(2).

43. Maier, S.A., *Plasmonics : fundamentals and applications*. 2007, New York: Springer. xxiv, 223 p.

44. Balanis, C.A., *Advanced engineering electromagnetics*. 1989, New York: Wiley. xx, 981 p.

45. Schasfoort, R.B.M. and A.J. Tudos, *Handbook of surface plasmon resonance*. 2008, Cambridge, UK: RSC Pub. xxi, 403 p.

46. West, P.R., et al., *Searching for better plasmonic materials.* Laser & Photonics Reviews, 2010. **4**(6): p. 795-808.

47. Kippenberg, T.J. and K.J. Vahala, *Cavity optomechanics: Back-action at the mesoscale.* Science, 2008. **321**(5893): p. 1172-1176.

48. Sheard, B.S., et al., *Observation and characterization of an optical spring.* Physical Review A, 2004. **69**(5).

49. Metzger, C.H. and K. Karrai, *Cavity cooling of a microlever.* Nature, 2004. **432**(7020): p. 1002-1005.

50. Metzger, C., et al., *Optical self cooling of a deformable Fabry-Perot cavity in the classical limit.* Physical Review B, 2008. **78**(3).

51. Arcizet, O., et al., *Radiation-pressure cooling and optomechanical instability of a micromirror.* Nature, 2006. **444**(7115): p. 71-74.

52. Woolf, D., et al., *Optomechanical and photothermal interactions in suspended photonic crystal membranes.* Optics Express, 2013. **21**(6): p. 7258-7275.

53. Vahala, K., et al., *A phonon laser.* Nature Physics, 2009. **5**(9): p. 682-686.

54. Grudinin, I.S., et al., *Phonon Laser Action in a Tunable Two-Level System.* Physical Review Letters, 2010. **104**(8).

55. Khurgin, J.B., et al., *Laser-Rate-Equation Description of Optomechanical Oscillators.* Physical Review Letters, 2012. **108**(22).

56. Mahboob, I., et al., *Phonon Lasing in an Electromechanical Resonator*. Physical Review Letters, 2013. **110**(12).

57. Povinelli, M.L., et al., *Evanescent-wave bonding between optical waveguides.* Optics Letters, 2005. **30**(22): p. 3042-3044.

CHAPTER 2: Optical Absorbers Based on Surface Plasmon Resonances

2.1. Introduction

Optical absorbers are devices wherein the incident radiation of light can be absorbed efficiently and converted into heat [1, 2]. Depending on the design, the absorption efficiency is optimized for particular wavelengths. For a lossless medium, light is usually partially reflected and partially transmitted, and the intensities of the reflection and transmission at a certain wavelength add up to the incident intensity. For absorbers, reflection or transmission may still occur, but the sum of them is less than the incident intensity by the amount of absorption.

As the previous chapter has discussed, metals are usually highly reflective at optical frequencies. Fortunately surface plasmons are able to provide a path to couple light into local fields. Photons excite the electron oscillation, and the oscillating electrons eventually lose their kinetic energy through electron-ion collisions, resulting in heating the materials. Optical absorbers based on surface plasmon resonances, or plasmonic (metamaterial) absorbers, usually exhibit impressive efficiencies because plasmonic resonances can generate very much enhanced local fields and the electromagnetic energy dissipation is proportional to the square of the electric field intensity (equation (23)). As a result of the resonance nature of plasmonics and the dispersion character of materials, the absorption is usually wavelength dependent. Perfect absorbers have been developed based on surface plasmon resonances, which can all incident light at the operating wavelengths [3-6].

2.2. Plasmonic Absorbers in Infrared for Thermal Detectors[4]

2.2.a. Background

A plasmonic-nanoantenna-based infrared absorber for thermal infrared detectors is proposed. Optical nanoantennas are commonly used for their ability to enhance and localize electromagnetic radiation. Here, we demonstrate that these nanoscale analogs of microwave antennas can absorb the incident radiation efficiently owing to their resonant response. The proposed structures can absorb up to 45% of the incoming infrared radiation for an areal coverage of only 2.5%. Compared to a uniform metal layer of the same thickness, the reported absorption is an order of magnitude larger. This reduced size of the absorber with higher efficiency is very critical for the performance of thermal detectors. The detection noise level of such detectors scales with the thermal conductance of the system that increases with increasing absorber thickness.

Thermal infrared detectors, such as bolometers, consists of an absorber and some "thermometer" mechanism to measure the induced temperature change due to absorption of radiation [8, 9]. The noise performance of these detectors is fundamentally limited by the total thermal conductance of the system, which scales with the total thickness of the absorber [10]. Recently, it was proposed that metamaterials [11-13] can be used as "perfect" absorbers that can resonantly absorb over 90% of incoming infrared radiation [3, 14-17]. Metamaterial absorbers can, potentially, significantly improve the absorption efficiency of

[4] This section is majorly adopted from [7].

thermal detectors. However, as far as the noise is concerned the demonstrated structures are comparable in thickness to absorbers currently used in state-of-the-art thermal detectors [18-20]. Another structure of interest in the field of plasmonics is the optical nanoantenna [21-24], which is the optical analog of microwave antennas. Nanoantennas are widely used, owing to their ability to localize and enhance electromagnetic radiation, for imaging and sensing applications [25-28]. However, the resonant absorption in optical nanoantennas is often overlooked. We propose a truly nanoscale single layer nanoantenna based infrared absorber that can significantly improve the noise performance of thermal detectors.

2.2.b. Absorber Design

The mid-infrared (mid-IR) nanoantenna based absorber design is illustrated in Figure 2-5. A very thin (200 nm) but robust silicon nitride membrane serves as the substrate for the periodic gold nanostrip antenna array. We use the finite-difference time-domain (FDTD) method, to simulate the nanoantenna array around a design wavelength of 6 μm. Simulations are performed using periodic boundary conditions on a unit cell containing a single gold nanostrip antenna. A plane wave is normally incident onto the gold nanostrip, with the electric field (E) polarized parallel to the longitudinal axis of the nanoantenna. Two 2D power monitors are placed in the far field of the front and back sides of the absorber to calculate the transmission and reflection for the nanoantenna array. The absorbance, A, is calculated by using the equation A=1-T-R, where T and R are normalized transmission and reflection for the absorber, respectively [3].

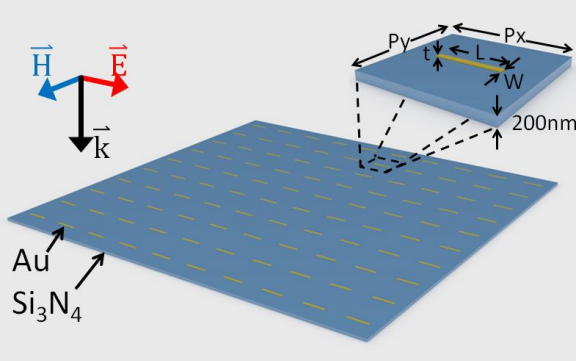

Figure 2-5. The schematic geometry and illumination configuration of the mid-IR nanoantenna absorber. L, W, and t represent the length, width, thickness of a single gold nanostrip, repectively. Px and Py are the longitudinal and lateral periods of the nanoantenna array. The array is illuminated from the top with electric field (E) polarized along the nanostrips. A 5 nm of titanium adhesion layer is assumed.

2.2.c. FDTD Simulation Study

Figure 2-6(A) shows the absorption, transmission, and reflection spectra for an optimized nanoantenna absorber with nanostrip length L=1500 nm, width w=150 nm, and thickness t=20 nm. These parameters are optimized by generating parametric maps for absorbance around 6 μm. The longitudinal (Px) and lateral (Py) periods of the array are both 3000 nm. In this study, a 5 nm titanium adhesion layer is inserted below the gold antenna layer in order to get realistic results. The nanoantenna resonance appears as a dip in transmission and as a peak in reflection at around a wavelength of 6 μm. The absorption spectrum reaches a peak value of 45.4% at 5.95 μm, with a bandwidth of 1.15 μm.

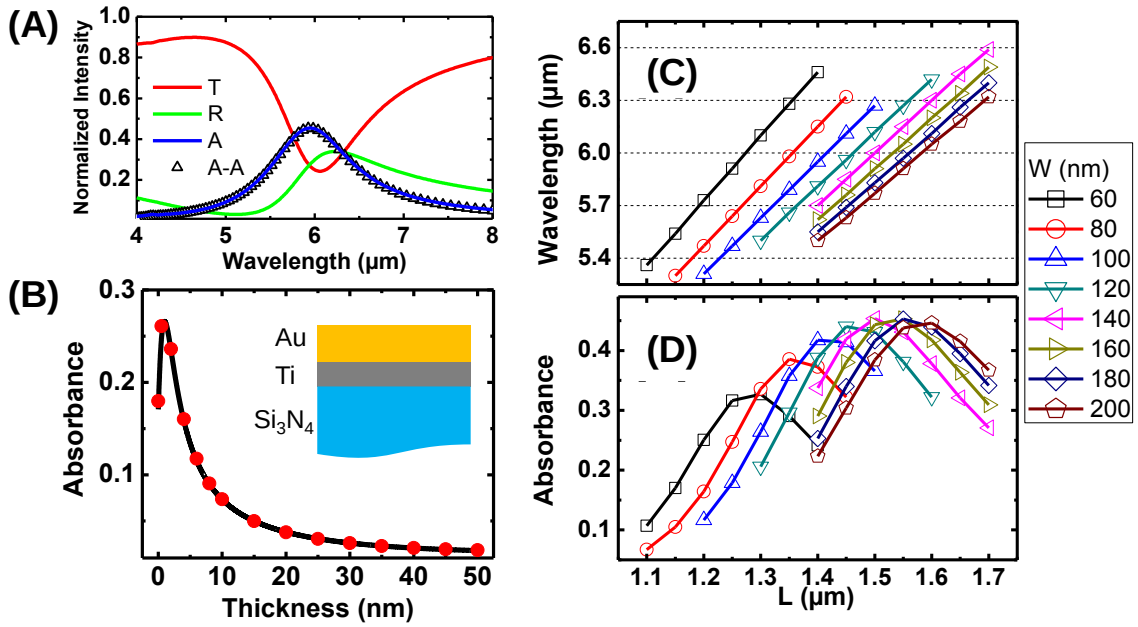

Figure 2-6. Absorber (A) The transmission T (red solid curve), reflection R (green solid curve), and absorption A (blue solid curve) spectra of the nanoantenna absorber.The absorption (A-A) spectra based on dissipated power is shown as hollow triangles. (B) The absorbance of a uniform gold layer for radiation with a wavelength of 6 μm as a function of the film thickness. The solid curve is the analytical result calculated by transfer matrix method. The red dots are the FDTD results. (C) The absorption peak wavelength as a function of gold nanostrip length (L) for different widths (W). (D) The absorbance at 6 μm as a function of nanoantenna length (L) for various antenna widths (W). The geometric parameters t=20 nm and Px=Py=3000 nm are used for all these simulations.

A thin uniform metal layer is commonly used in thermal detectors as an absorber, though with limited absorption efficiency [19]. For comparison with the nanoantenna absorber, we investigated the absorption in a very thin layer of gold on a silicon nitride substrate. We analytically calculated the absorbance of the gold thin film absorber as a function of the layer thickness using the transfer matrix method. Figure 2-6(B) shows how the absorbance at 6 μm varies with the gold thin film thickness in addition to a 5 nm titanium layer. For gold films much thinner than 10 nm (the skin depth of gold at 6 μm),

the electromagnetic fields can reach the bottom of the film and reflect multiple times dissipating electromagnetic energy through the free electron absorption. As the film gets thicker, the electromagnetic fields cannot penetrate significantly beyond the skin depth and are reflected. The absorption maximum (26.6%) appears at about 1 nm thickness, which is impractical since usual deposition techniques like electron-beam evaporation cannot yield such ultra-thin uniform and continuous gold films as a result of the formation of metal islands for such thicknesses [29]. For reasonable film thicknesses over 20 nm, the absorbance is less than 3.8%. FDTD results are in excellent agreement with the analytical absorbance (Figure 2-6(B)).

On the contrary, the nanoantenna absorber, comprising gold nanostrips of the same thickness (20 nm), can absorb 45.1% of the incident mid-IR radiation energy at 6 μm (Figure 2-6(A)) corresponding to a 10-fold enhancement in absorption efficiency for only 2.5 % areal coverage. With less metal, the total thermal conductance, and consequently the noise level, can be reduced. The physical mechanism of this nanoantenna absorber is straightforward: when excited resonantly a current will be induced in the gold nanostrips, which will be dissipated due to the Ohmic losses in the metal, similar to power dissipated in a resistor. By the resonance effect [23], the gold nanoantennas can capture the incident energy and dissipate it into heat effectively before it is radiated back into the space.

For the FDTD simulation configuration we use, it is possible that the energy carried in the side-scattered waves is omitted during the far field transmission or reflection calculations. To verify this part, we calculate the power dissipated by the near fields on the lossy nanoantenna. The equation $P = \frac{1}{2}\omega\varepsilon''|E|^2$ gives the dissipated power density, where

ε'' is the absolute value of the imaginary part of the permittivity of the metal. Absorbance from Joule heating is acquired by integration of the dissipated power density over the simulation space and normalization to the source power (Figure 2-6(A)). This result is quite close to the absorbance curve acquired by A=1-T-R calculation, because the angular profile of the scattered waves is minimally modulated by the array (i.e. a 2D grating). The array periods are smaller than the wavelength, so only zero order output is expected. This is a good indicator that the A=1-T-R is an accurate approximation for this study.

The resonance wavelength is strongly dependent on geometric parameters [21]. Therefore it is crucial to optimize the nanoantenna absorber for specific resonance wavelengths targeted. This nanoantenna absorber can be easily tuned to different resonance wavelengths. If the array periods, thickness, and width are fixed, the absorption peak wavelength scales linearly with the nanostrip length as illustrated in Figure 2-6(C). With this map, the compatible geometric parameters of L and w for a certain resonance wavelength can be roughly located. To search for the best L and w for absorption, the absorbance data at 6 μm are plotted in Figure 2-6(D). The best performance is found for 140 nm<w<160 nm and 1500 nm<L<1550 nm.

We also investigated the effects of coupling strength between adjacent nanoantennas. For large array periods (i.e. comparable with the wavelength), the coupling between neighboring unit cells rarely exists. On the other hand, when the array periods are small, the coupling strength plays a significant role. Figure 2-7(A) and (B) illustrate, as P_x (P_y) decreases, the absorption peak is redshifted (blueshifted), because the head-to-head (side-to-side) coupling of adjacent gold nanostrips lowers (raises) the resonant energy

level. Figure 2-7(C) shows the influence of thickness on absorption spectra: for thinner gold nanostrips, the peak is redshifted, due to the increase of the effective index. At a particular wavelength, e,g, 6 μm, there is an optimized thickness to achieve efficient absorption, because too thin gold nanostrips transmit too much and too thick gold nanostrips reflect too much. A thickness of ~20 nm is best for absorption at 6 μm. To optimize P_x and P_y for absorption at 6 μm, the absorbance data are plotted as a colormap (Figure 2-7(D)). The maximum absorbance is found when P_x=2.5 to 3 μm and P_y=3 μm. This is how the optimized design in Figure 2-6(A) was determined.

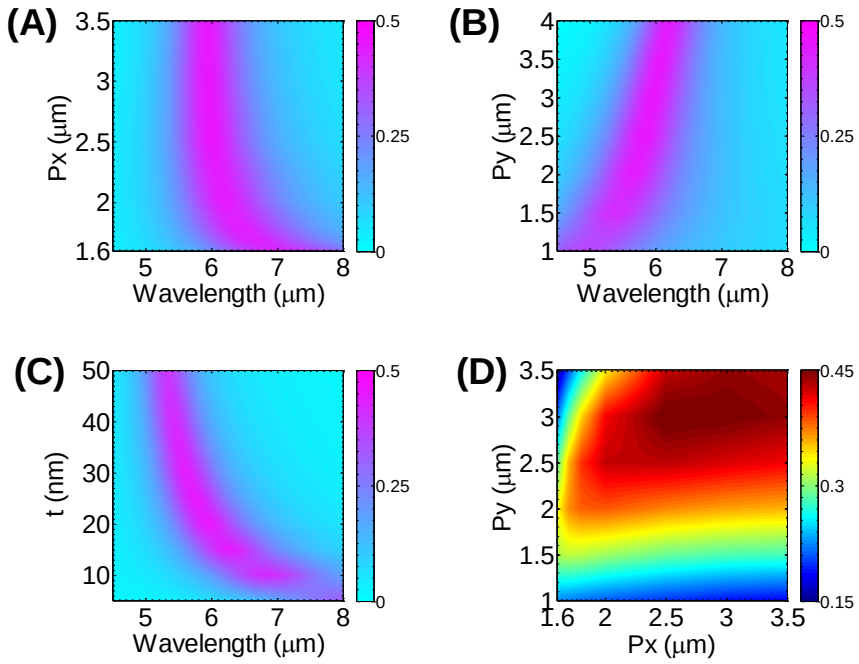

Figure 2-7. The absorbance colormap as a function of (A) wavelength and longitudinal period (P_x), (B) wavelength and lateral period (P_y), and (C) wavelength and gold nanostrip thickness (t). (D) The colormap of the absorbance at 6 μm, as a function of Px and Py. The geometric parameters L=1500 nm, W=150 nm, t=20 nm, P_x=P_y=3000 nm are used for all these simulations, except the ones varying in the colormap.

Due to the inherent anisotropy of the nanostrips, the nanoantenna array absorption is polarization dependent [23]. As shown in Figure 2-8, the polarization dependence of the absorption follows a $\cos^2\theta$ relation as expected for a linear dipole antenna. . We have also investigated, using a frequency domain finite element method (FEM) solver, the dependence of resonant absorption on the angle of incidence for plane waves polarized along the nanostrip. As the angle of incidence increases, the absorption peak redshifts resulting in smaller absorption at 6 μm (Figure 2-8). At an incidence angle of 60°, corresponding to a numerical aperture (NA) of ~0.9 in air, the absorbance drops to only 35%. This performance is very promising for such a simple structure as the NAs are much lower than this for mid-IR lenses [9].

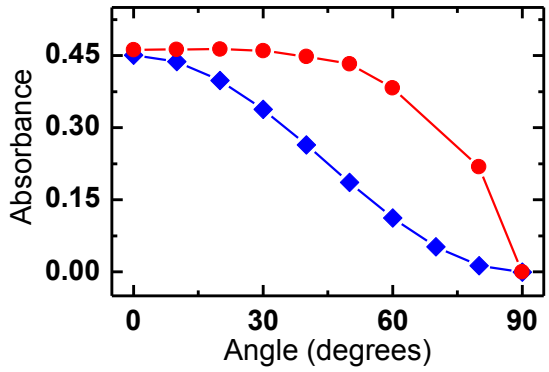

Figure 2-8. The polarization angle (θ) dependence of absorption (at 6 μm) for the nanoantenna array (blue ♦) calculated at 6 μm. The curve resembles the expected $\cos^2\theta$ dependence. The nanoantenna array absorbance as a function of incidence angle for light polarized along the nanostrips (red ●) is also shown.

2.3. Tunable Plasmonic Absorbers by Plasmonic and Optical Mode Coupling

2.3.a. Absorber Design and Simulation Study

Due to the resonance nature of plasmonic absorbers, the absorption is not universal over the complete electromagnetic spectrum range but occurs only at operating wavelengths. For some applications, tunability of the absorption wavelengths is desired. Although the operating wavelengths can be targeted by varying the design of the geometry of the plasmonic resonance structures, it is difficult to change the geometry physically once the device is made.

One alternative approach is to change the surrounding refractive index to tune the plasmonic resonance and, consequently, the absorptive wavelengths. We experimentally demonstrated an electrically tunable plasmonic mid-IR perfect absorber at 4 μm. The perfect infrared absorption was realized by an array of gold nanostrip antennas separated from a back reflector by a thin layer of indium tin oxide (ITO). By applying a bias voltage, the carrier injection into ITO layer caused a change in the refractive index and, consequently, the plasmonic resonance. A shift of 10 nm in the absorption peak was observed at 10 V [30].

We also found a more efficient way to realize a tunale plasmonic absorber, by coupling the plasmonic mode with the optical mode. In a system where the plasmonic nanostructures are on one of the two mirrors of a FP cavity (Figure 2-9(A)), a Fano-like [31, 32] electromagnetic coupling between the plasmonic and FP resonances yields hybrid near-perfect absorption resonances (Figure 2-9(B)). The spectral position of FP resonances strongly depends on the FP cavity length. The peak position of the hybrid mode acquires

the character from its parent, the FP resonance, so it become tunable by changing the gap between M1 and M2. Changing the gap is relatively easy to implement, as long as the position of M1 or M2 is flexible. This condition is naturally satisfied in an optomechanical system.

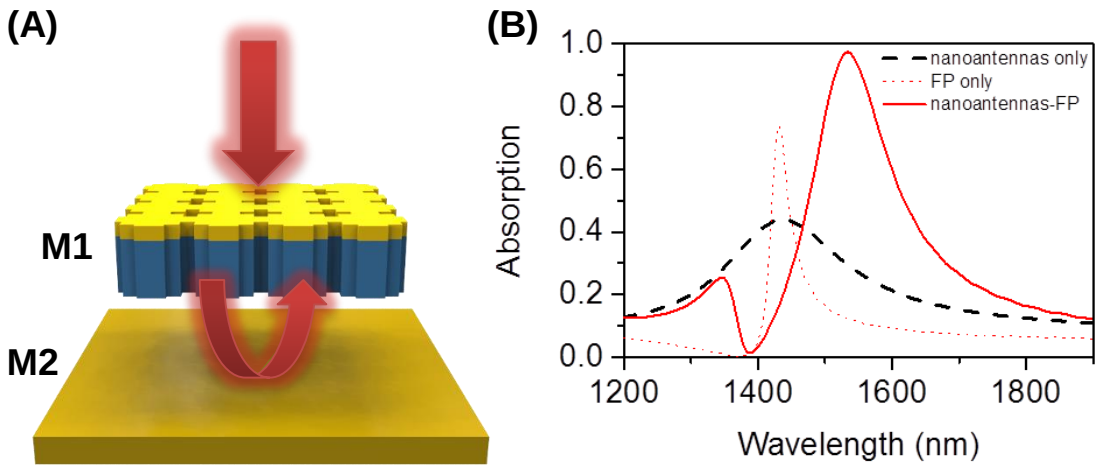

Figure 2-9. Plasmonic and FP cavity mode coupling. (A) The plasmonic coupled FP cavity consists of a semi-mirror (M1) made of a gold thinfilm of 25 nm thickness on a silicon nitride membrane of 100 nm thickness, and a second mirror (M1) made of a gold thinfilm of 50 nm. M1 is modified with nano sized cross-shape thru-holes, which supports plasmonic resonance at about 1437 nm. (B) The simulated spectra of the absorption on the plasmonic nanostructure. The black dashed curve is for nanoantennas only (M1); the red dotted curve is for FP cavity only (1200 nm gap between the holeless M1 and M2); the red curve is for the coupled mode (1200 nm gap between M1 and M2).

Further FDTD simulation study demonstrated the peak shift as well as the slightly variant peak shape of the hybrid mode, as the absorption spectra shown in Figure 2-10(A). In these simulations, the same configuration as that in Figure 2-9(B) was used, and the cavity length was tuned from 1200 nm to 1300 nm. An absorption peak redshift of 59 nm

was observed. Figure 2-10(A) also shows the hybrid resonance shift is in accordance to the imaginary FP resonance shift. In the extended simulation on the spectra-tuning dependence, an avoided energy crossing occurs when the two resonances overlap spectrally (Figure 2-10(B)).

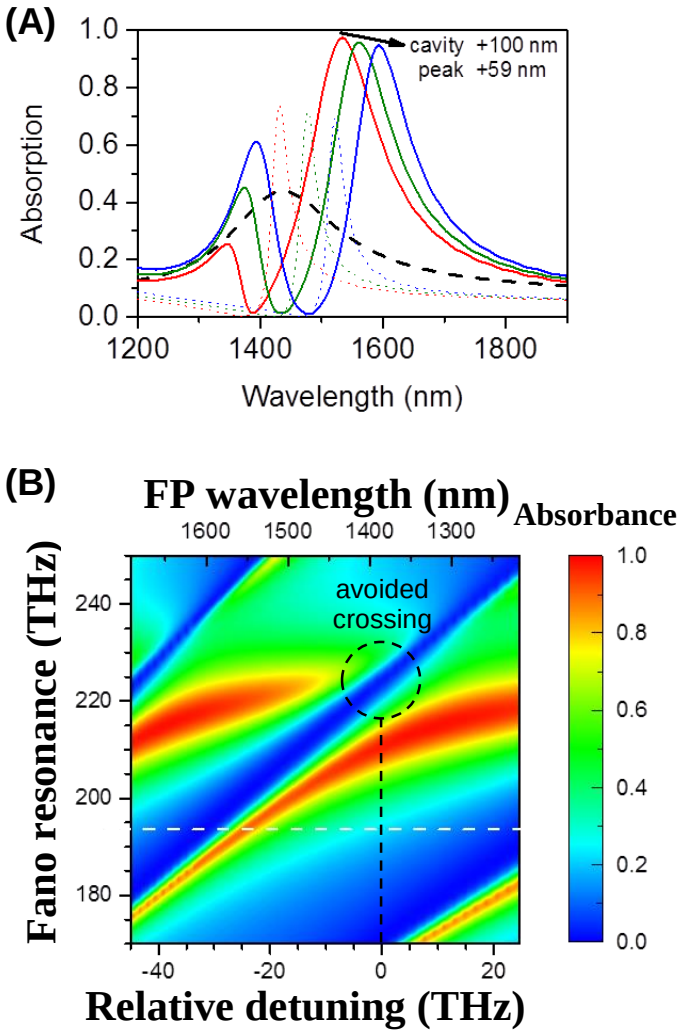

Figure 2-10. Simulated tuning of the plasmonic-FP hybrid Fano mode. (A) The absorption peak redshifts 59 nm as the FP cavity length increases from 1200 nm to 1300 nm. (B) The absorption spectra at different tuning conditions. The color shows the absorbance, each vertical line represents the absorption spectrum at the specific tuning condition (shown as the FP peak wavelength as well as the FP resonance detuned from plasmonic resonance frequency), and each horizontal line

representd the absorption at the specific frequency when the cavity is tuned. The white dash line marks the frequency of interest (1550 nm), and the black dash circle marks the avoided crossing.

2.3.b. Coupled Oscillator Model

In order to explain the underlying physical coupling mechanism for the Fano-like resonances, we employ a coupled oscillator model using the analogy of two coupled mechanical harmonic oscillators (Figure 2-11(C)). The hybrid system is described with equations very similar to the equation of motion of mechanical harmonic oscillators [33]. Use "1" is to denote "FP resonance", and "2" is to denote "plasmonic resonances", yielding:

$$\ddot{a}_1 + \gamma_1 \dot{a}_1 + \omega_1^2 a_1 - C_{12} a_2 = 0 \tag{52}$$

$$\ddot{a}_2 + \gamma_2 \dot{a}_2 + \omega_2^2 a_2 - C_{12} a_1 = a_{drive} \tag{53}$$

where $a_{1,2}$ is the optical field, $\gamma_{1,2}$ is the optical mode linewidth, C_{12} is the mode coupling coefficient, a_{drive} is the external excitation field, and $\omega_{1,2}$ is the eigen-frequency of the optical mode. Using $A_{1,2}$ to represent the complex amplitude of the optical mode and A_e to represent that of the external excitation field, the fields are expressed as $a_1 = A_1 e^{-i\omega t}$, $a_2 = A_2 e^{-i\omega t}$, and $a_{drive} = A_e e^{-i\omega t}$. Equations (52) and (53) are then organized into:

$$\begin{pmatrix} -\omega^2 - i\omega\gamma_1 + \omega_1^2 & -C_{12} \\ C_{12} & -\omega^2 - i\omega\gamma_2 + \omega_2^2 \end{pmatrix} \begin{pmatrix} A_1 \\ A_2 \end{pmatrix} = \begin{pmatrix} 0 \\ A_e \end{pmatrix} \tag{54}$$

By solving the linear equation set (54), the complex amplitudes are found:

$$A_1 = \frac{C_{12} A_e}{\left(-\omega^2 - i\omega\gamma_1 + \omega_1^2\right)\left(-\omega^2 - i\omega\gamma_2 + \omega_2^2\right) + C_{12}^2} \tag{55}$$

$$A_2 = \frac{\left(-\omega^2 - i\omega\gamma_1 + \omega_1^2\right)A_e}{\left(-\omega^2 - i\omega\gamma_1 + \omega_1^2\right)\left(-\omega^2 - i\omega\gamma_2 + \omega_2^2\right) + C_{12}^2} \tag{56}$$

Given the spectra of the F-P and plasmonic modes, we can extract the values of ω_1, ω_2, γ_1 and γ_2 out of the peak position and width. There are two ways to utilize the equations (55) and (56). By fitting the hybrid mode spectrum with the function $\left|A_1(\omega) + A_2(\omega)\right|^2$, we can estimate the values of the mode coupling coefficient C_{12}. By adjusting the values of C_{12} and A_e, we can simulate the spectrum of the hybrid mode, which is $\left|A_1(\omega) + A_2(\omega)\right|^2$, and demonstrate how the spectrum evolves with different FP frequency ω_1.

In Figure 2-11(A), the same spectra from Figure 2-9(B) are plotted in energy domain instead of frequency domain, simply by the conversion relation $E = \hbar\omega = \frac{hc}{\lambda}$. In order to facilitate the numerical calculation, eV is taken as the energy unit [34]. By measuring the FP and plasmonic resonance peaks, we acquire the individual eigenfrequency and damping rate: $\omega_1 = 0.8681$ eV, $\gamma_1 = 0.0232$ eV, $\omega_2 = 0.8654$ eV, and $\gamma_2 = 0.1651$ eV. By tuning the values of C_{12} and A_e, a spectrum curve is obtained (Figure 2-11(B-i)) which is analogous to the one in Figure 2-11(A). By decreasing ω_1, a series of spectra are acquired, which simulate the evolution of the hybrid mode spectrum.

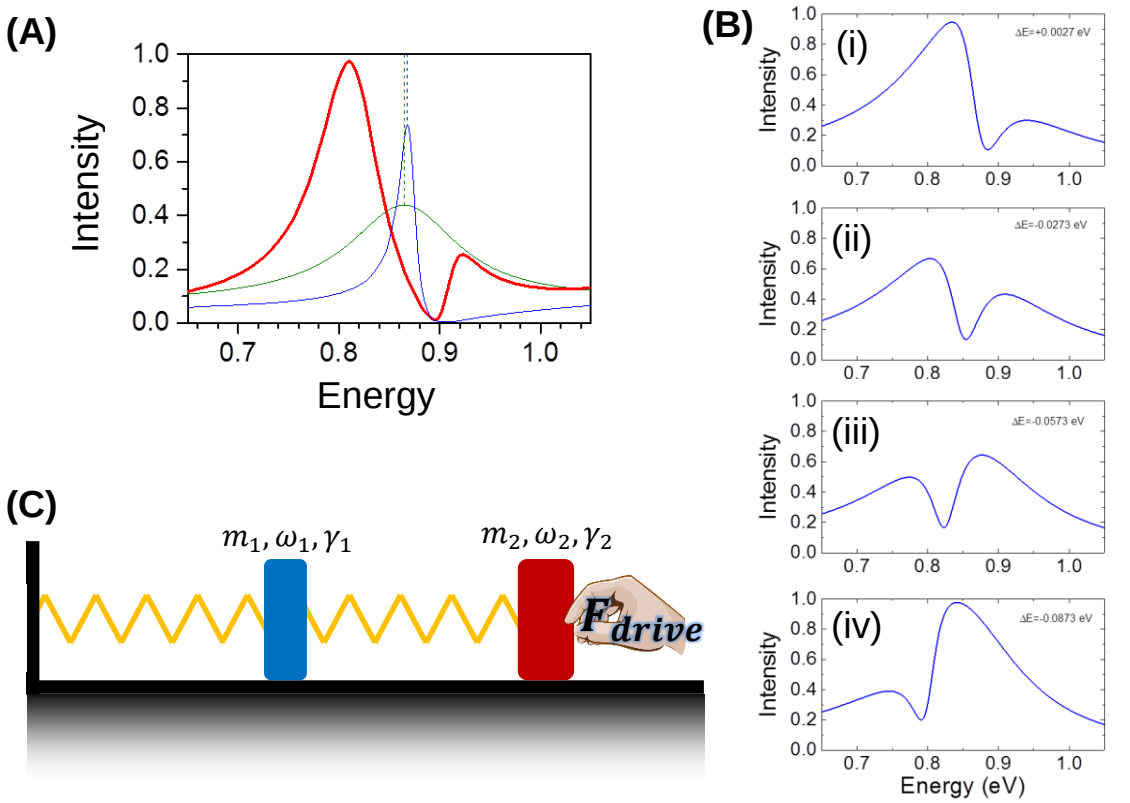

Figure 2-11. Hybrid Fano resonance interpreted by coupled oscillator model. (A) A typical FDTD simulation result showing the spactra for the plasmonic absorber (green), the FP cavity (blue), and the resulted Fano resonances (blue) for nearly zero detuning. (B) The coupled oscillator model simulates the spectra for different energy detuning values ($\hbar\omega_1 - \hbar\omega_2$). Panel (i) corresponds to the FDTD simulation result in (A). The qualitative agreement between the two is evident despite the simplified model. From Panel (i) to (iv), the FP resonance redshifts and $\hbar\omega_1$ decreases. (C) The schematic of the equivalent coupled mechanical harmonic oscillator model.

2.4. Conclusions

In summary, we demonstrated an extremely thin resonant infrared absorber based on gold nanostrip antennas, which can absorb up to 45% of the incoming radiation. This seemingly smaller absorption compared to a perfect absorber is achieved for a metal

thickness that is an order of magnitude smaller [16]. By eliminating continuous metallic structures in the absorber design, the device thermal conductance is significantly reduced. This is critical for infrared thermal detectors as, the thermal conductance determines the minimum noise level, which depends on the thickness of the absorber [8]. Compared to a bulk metal layer, the nanoantenna design offers a 10-fold enhancement in absorption with only an areal coverage of 2.5 % for the same thickness. The polarization dependence of the present structure can be removed by utilizing a symmetric antenna design. A broadband version of this absorber also can easily be achieved by utilizing coupled antennas of different sizes. This design is promising for low thermal noise infrared thermal detectors.

We also designed a tunable plasmonic absorber based on a FP cavity with one mirror modified by plasmonic nanostructures. The coupling between the FP and plasmonic mode leads to a Fano-like hybrid mode, which has near-perfect absorption at the resonance peak. The resonance peak position of the hybrid mode is determined by the FP resonance wavelength, which depends on the FP cavity length. The formation of the hybrid mode can be interpreted by the coupled oscillator model which has been used in coupled mechanical harmonic oscillator systems. This type of absorber can be easily tuned by changing the position of one of the two mirrors, which is suitable as part of an optomechanical system.

2.5. References

1. Cui, Y.X., et al., *Plasmonic and metamaterial structures as electromagnetic absorbers.* Laser & Photonics Reviews, 2014. **8**(4): p. 495-520.
2. Brongersma, M.L., N.J. Halas, and P. Nordlander, *Plasmon-induced hot carrier science and technology.* Nature Nanotechnology, 2015. **10**(1): p. 25-34.
3. Landy, N.I., et al., *Perfect metamaterial absorber.* Physical Review Letters, 2008. **100**(20).

4. Liu, N., et al., *Infrared Perfect Absorber and Its Application As Plasmonic Sensor.* Nano Letters, 2010. **10**(7): p. 2342-2348.

5. Fang, Z.Y., et al., *Tunable wide-angle plasmonic perfect absorber at visible frequencies.* Physical Review B, 2012. **85**(24).

6. Walter, R., et al., *Large-Area Low-Cost Tunable Plasmonic Perfect Absorber in the Near Infrared by Colloidal Etching Lithography.* Advanced Optical Materials, 2015. **3**(3): p. 398-403.

7. Zhu, H., F. Yi, and E. Cubukcu, *Nanoantenna Absorbers for Thermal Detectors.* Ieee Photonics Technology Letters, 2012. **24**(14): p. 1194-1196.

8. Kruse, P.W., *Uncooled Infrared Imaging Arrays and Systems*. 1997, San Diego, CA: Academic Press.

9. Piotrowski, J. and A. Rogalski, *High-operating-temperature infrared photodetectors*. 2007, Bellingham, Wash.: SPIE. xiv, 240 p.

10. Low, F.J. and A.R. Hoffman, *The Detectivity of Cryogenic Bolometers.* Applied Optics, 1963. **2**(6): p. 649-650.

11. Aydin, K., et al., *Experimental observation of true left-handed transmission peaks in metamaterials.* Optics Letters, 2004. **29**(22): p. 2623-2625.

12. Soukoulis, C.M. and M. Wegener, *Past achievements and future challenges in the development of three-dimensional photonic metamaterials.* Nature Photonics, 2011. **5**(9): p. 523-530.

13. Aydin, K., I.M. Pryce, and H.A. Atwater, *Symmetry breaking and strong coupling in planar optical metamaterials.* Optics Express, 2010. **18**(13): p. 13407-13417.

14. Hao, J.M., et al., *High performance optical absorber based on a plasmonic metamaterial.* Applied Physics Letters, 2010. **96**(25).

15. Landy, N.I., et al., *Design, theory, and measurement of a polarization-insensitive absorber for terahertz imaging.* Physical Review B, 2009. **79**(12).

16. Liu, X.L., et al., *Infrared Spatial and Frequency Selective Metamaterial with Near-Unity Absorbance.* Physical Review Letters, 2010. **104**(20).

17. Avitzour, Y., Y.A. Urzhumov, and G. Shvets, *Wide-angle infrared absorber based on a negative-index plasmonic metamaterial.* Physical Review B, 2009. **79**(4).

18. Downey, P.M., et al., *Monolithic Silicon Bolometers.* Applied Optics, 1984. **23**(6): p. 910-914.

19. Dragovan, M. and S.H. Moseley, *Gold Absorbing Film for a Composite Bolometer.* Applied Optics, 1984. **23**(5): p. 654-656.

20. Nishioka, N.S., P.L. Richards, and D.P. Woody, *Composite Bolometers for Submillimeter Wavelengths.* Applied Optics, 1978. **17**(10): p. 1562-1567.

21. Cubukcu, E., et al., *Plasmonic Laser Antennas and Related Devices.* Ieee Journal of Selected Topics in Quantum Electronics, 2008. **14**(6): p. 1448-1461.

22. Crozier, K.B., et al., *Optical antennas: Resonators for local field enhancement.* Journal of Applied Physics, 2003. **94**(7): p. 4632-4642.

23. Muhlschlegel, P., et al., *Resonant optical antennas.* Science, 2005. **308**(5728): p. 1607-1609.

24. Cubukcu, E. and F. Capasso, *Optical nanorod antennas as dispersive one-dimensional Fabry-Perot resonators for surface plasmons.* Applied Physics Letters, 2009. **95**(20).

25. Alu, A. and N. Engheta, *Input impedance, nanocircuit loading, and radiation tuning of optical nanoantennas.* Physical Review Letters, 2008. **101**(4).

26. Cubukcu, E., et al., *Split ring resonator sensors for infrared detection of single molecular monolayers.* Applied Physics Letters, 2009. **95**(4).

27. Adato, R., et al., *Ultra-sensitive vibrational spectroscopy of protein monolayers with plasmonic nanoantenna arrays.* Proceedings of the National Academy of Sciences of the United States of America, 2009. **106**(46): p. 19227-19232.

28. Aksu, S., et al., *High-Throughput Nanofabrication of Infrared Plasmonic Nanoantenna Arrays for Vibrational Nanospectroscopy.* Nano Letters, 2010. **10**(7): p. 2511-2518.

29. Rao, C.N.R., et al., *An Investigation of Well-Characterized Small Gold Clusters by Photoelectron-Spectroscopy, Tunneling Spectroscopy, and Cognate Techniques.* Journal of Physical Chemistry, 1993. **97**(43): p. 11157-11160.

30. Yi, F., et al., *Voltage tuning of plasmonic absorbers by indium tin oxide.* Applied Physics Letters, 2013. **102**(22).

31. Luk'yanchuk, B., et al., *The Fano resonance in plasmonic nanostructures and metamaterials.* Nature Materials, 2010. **9**(9): p. 707-715.

32. Fan, S.H., W. Suh, and J.D. Joannopoulos, *Temporal coupled-mode theory for the Fano resonance in optical resonators.* Journal of the Optical Society of America a-Optics Image Science and Vision, 2003. **20**(3): p. 569-572.

33. Haus, H.A., *Waves and fields in optoelectronics*. Prentice-Hall series in solid state physical electronics. 1984, Englewood Cliffs, NJ: Prentice-Hall. xii, 402 p.

34. Rahmani, M., et al., *Influence of plasmon destructive interferences on optical properties of gold planar quadrumers.* Nanotechnology, 2011. **22**(24).

CHAPTER 3: Silicon Nitride Membranes as Mechanical Oscillators

3.1. Introduction

Silicon nitride (Si_3N_4) is a chemically-inert ceramic materials with high melting point and hardness. It has been widely used in manufacturing industries as well as research. It used to be obtained by high temperature reaction of nitrogen with silicon or silica-carbon mixture. The introduction of chemical vapor deposition (CVD), e.g. low pressure CVD (LPCVD) and plasma enhanced CVD (PECVD), by silane (SiH_4) and other precursors decreased the temperature required for silicon nitride growth. Nowadays, silicon nitride membranes grown by LPCVD (Figure 3-12) are commercially available and widely used in transmission electron microscopy and X-ray microscopy, where samples for imaging are carried on silicon nitride membrane windows with thickness of tens of nanometers.

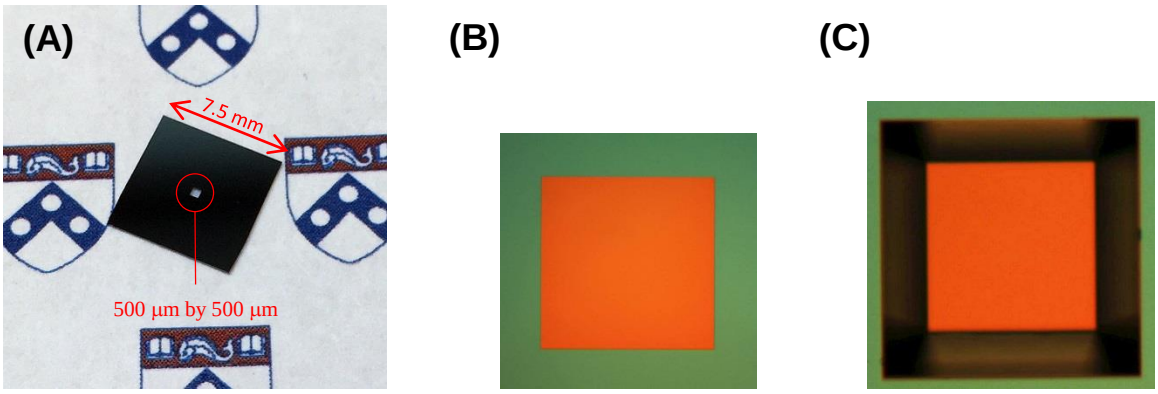

Figure 3-12. A silicon nitride membrane window on the frame. (A) The membrane of thickness of 100 nm appears transparent, sitting at the center of the silicon frame of 7.5 mm by 7.5 mm. A closer look under the microscope showing the (B) front and (C) back sides of the membrane window ("orange") of 500 μm by 500 μm. The membrane is leveled at the front side of the chip, so there are inclined side walls of silicon viewed from the back side. The colors of the micrographs are false due to white balance issues.

A free standing silicon nitride membrane on a square window is an ideal element in an optomechanical system, since it possesses suitable optical and mechanical properties. Thin membranes of silicon nitride are transparent in visible and infrared, with a refractive index of around 2. A silicon nitride membrane windows anchored by the frame is a natural mechanical oscillator with vibrational eigenmodes determined by the material stress and window geometry.

The motion of the membrane can be detected by laser interferometry. A measurement system was built to transduce the mechanical vibration to optical signals and then to electric signals. After amplification and filtering, the AC component of the electric signal is read by a spectrum analyzer. With proper calibration, the mechanical vibrational spectra are acquired, which is necessary for the optomechanical system study.

3.2. Vibrational Eigenmodes of a Square Membrane Oscillator

A free standing silicon nitride membrane on a square window is a natural mechanical oscillator, whose vibrational eigenmodes are determined by the stress, mass density and the geometric parameters of the window.

Considering the transverse vibrations of a square-shaped isotropic membrane, the motion of the membrane is governed by the wave equation [1]:

$$\frac{\partial^2 z(x,y,t)}{\partial x^2}+\frac{\partial^2 z(x,y,t)}{\partial y^2}=\frac{\rho}{\sigma}\frac{\partial^2 z(x,y,t)}{\partial t^2} \tag{57}$$

where ρ is the mass density of the material and σ is the stress of the membrane. The membrane is anchored to the square window frame of side length of l (Figure 3-13(B)), yielding the boundary conditions:

$$z\left(x=0,y,t\right)=z\left(x=a,y,t\right)=z\left(x,y=0,t\right)=z\left(x,y=a,t\right)=0 \tag{58}$$

Assume the membrane is at rest with the initial profile $z_0\left(x,y\right)$, yielding the initial conditions:

$$z\left(x,y,t=0\right)=z_0\left(x,y\right) \tag{59}$$

$$\frac{\partial z\left(x,y,t=0\right)}{\partial t}=0 \tag{60}$$

Using separation of variables, the solution is in the form:

$$z\left(x,y,t\right)=X\left(x\right)\cdot Y\left(y\right)\cdot T\left(t\right) \tag{61}$$

Insert the solution of equation (57), yielding three homogeneous Helmholtz equations:

$$\frac{\partial^2 X\left(x\right)}{\partial x^2}+\alpha^2 X\left(x\right)=0 \tag{62}$$

$$\frac{\partial^2 Y\left(y\right)}{\partial y^2}+\beta^2 Y\left(y\right)=0 \tag{63}$$

$$\frac{\partial^2 T\left(t\right)}{\partial t^2}+\frac{\sigma}{\rho}\left(\alpha^2+\beta^2\right)X\left(x\right)=0 \tag{64}$$

Considering the boundary and initial conditions, the solutions to the above equations are

$$X\left(x\right)=A_x\sin\alpha x \tag{65}$$

$$Y\left(y\right)=A_y\sin\beta y \tag{66}$$

$$T\left(t\right)=A_t\cos\left[\sqrt{\frac{\sigma}{\rho}\left(\alpha^2+\beta^2\right)}t\right] \tag{67}$$

where A_x, A_y, and A_t are constants, $\alpha = \frac{i\pi}{l}$, $\beta = \frac{j\pi}{l}$, and $i, j = 1, 2, 3, \cdots$.

Therefore the solution of the 2D wave equation (57) is given:

$$z(x, y, t) = \sum_{i=1}^{\infty} \sum_{j=1}^{\infty} A_{ij} \sin \frac{i\pi x}{l} \sin \frac{j\pi y}{l} \cos\left(\pi \sqrt{\frac{\sigma}{\rho} \cdot \frac{i^2 + j^2}{l^2}} t \right) \tag{68}$$

This is the superposition of all eigenmodes with index i, j. For each eigenmode, the frequency is

$$f_{i,j} = \frac{1}{2} \sqrt{\frac{\sigma}{\rho} \cdot \frac{i^2 + j^2}{l^2}} \tag{69}$$

and the amplitude profile is

$$z_{ij}(x, y) = A_{ij} \sin \frac{i\pi x}{l} \sin \frac{j\pi y}{l} \tag{70}$$

Figure 3-13(A) illustrates the amplitude profiles of the first few eigenmodes. It should be noticed that there are degenerate modes, i.e. $f_{i,j} = f_{j,i}$, in square membranes, comparing to normal rectangular ones.

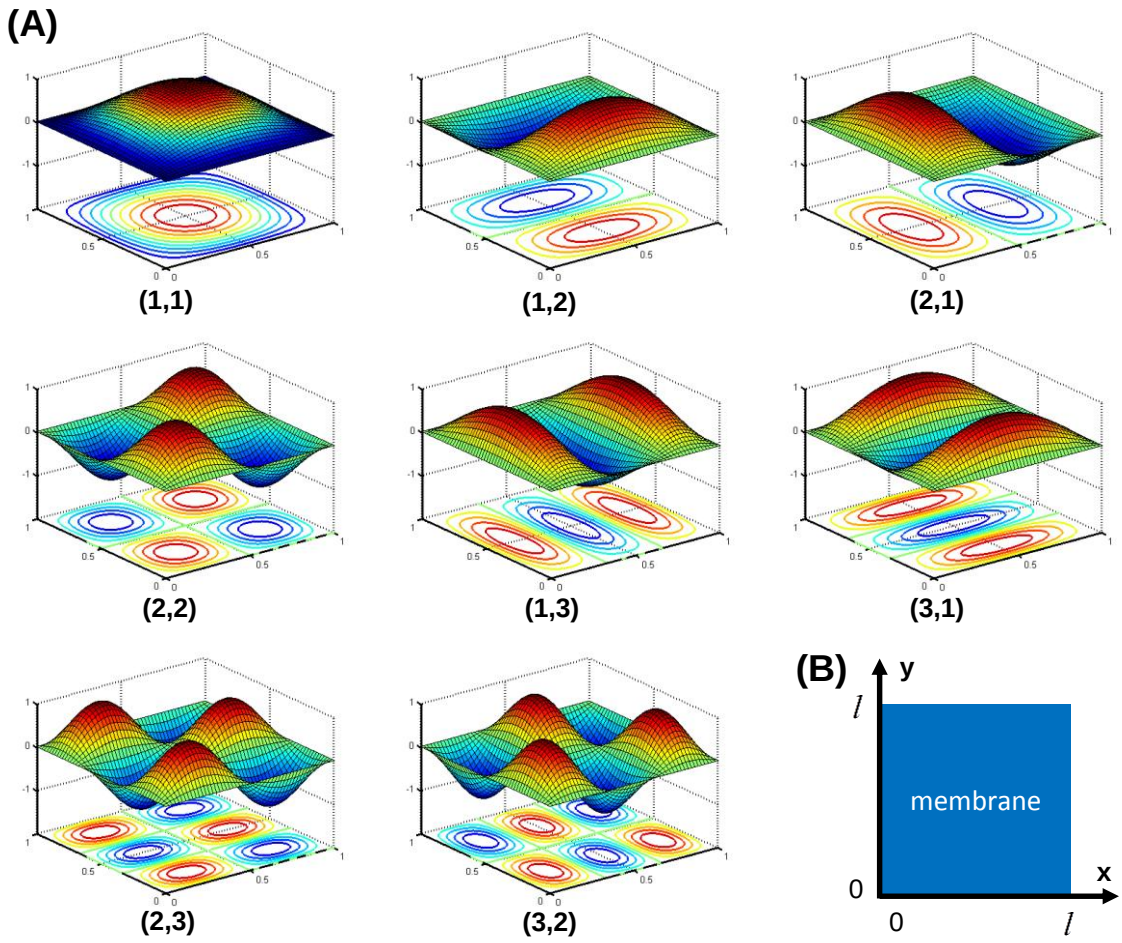

Figure 3-13. Demonstration of the vibrational eigenmodes of the square membrane oscillator. (A) The amplitude profiles of the lowest 8 eigenmodes. (B) The geometric parameters of the membrane in the Cartesian coordinate.

3.3. Membrane Motion Measurement by Laser Interferometry

A membrane oscillator in the air or even finite vacuum bears random impacts by molecules and microparticles, resulting in Brownian motion (vibration) of the membrane. The spectrum of such random vibration basically manifests multiple peaks at the eigenfrequencies (equation (69)). The amplitude of the Brownian motion depends on the mechanical Q factor and environmental temperature, and is usually very small, e.g. several

picometers for the device studied in this thesis. Laser interferometry is capable in detecting such weak motions.

A 1550 nm laser is used as the optical input for the plasmomechanical device, and demonstrates the mechanical oscillation amplification or cooling depending on the optical resonance detuning. With an optical fiber collimator and a convex lens, the 1550 nm laser is focused onto the center of the nanoantenna array. At the same time, the reflected optical power is collected by the convex lens and coupled back to the optical fiber. By adding a circulator in the input optical fiber, the reflected light is directed to a sensitive photodetector. The photodetector outputs electrical signal, which is amplified and sent to a spectrum analyzer. The electrical spectrum is then recorded. Figure 3-14 illustrates the setup of the measurement system.

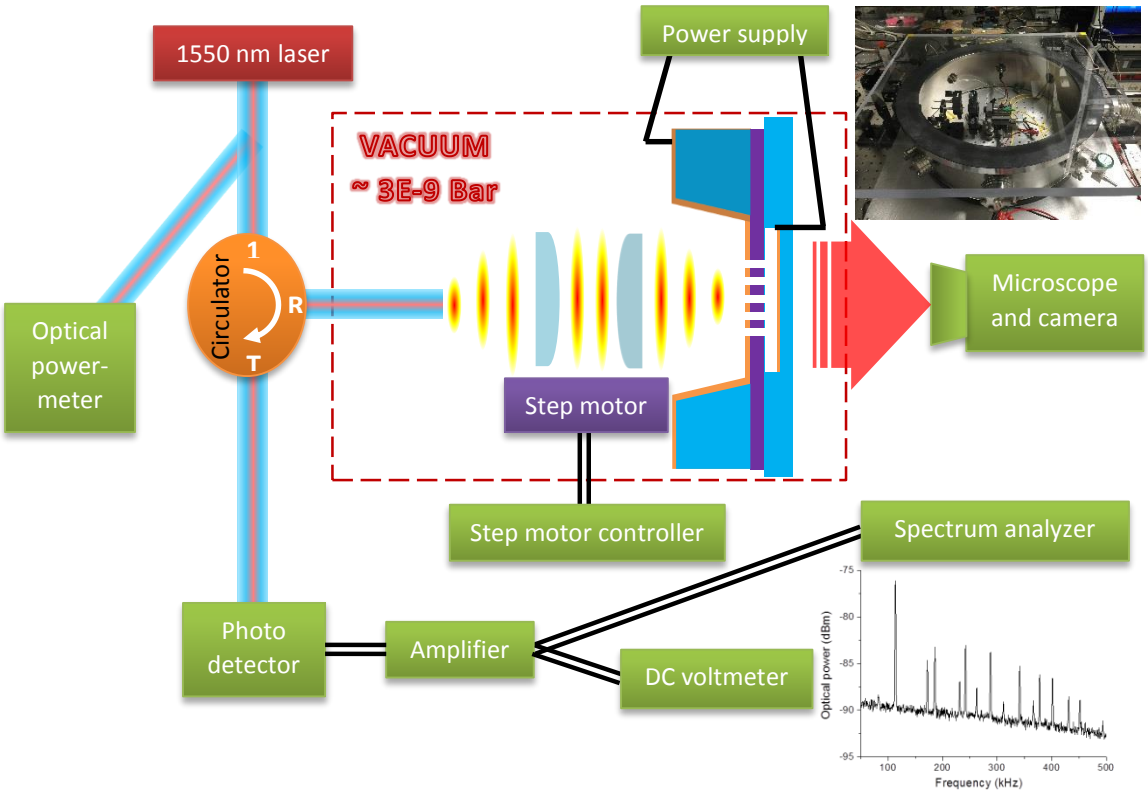

Figure 3-14. The schematic of the optomechanical measurement system. The area boxed by the red dash rectangular is in vacuum. The right bottom exemplifies a raw spectrum acquired by this system. The right top shows the major part of the vacuum chamber.

The optical reflection depends on the gap size between the membrane and bottom back reflector. When the membrane is oscillating, its displacement transduces to the AC variation of reflected optical power and eventually the electrical voltage signal. Therefore, the electrical spectrum represents the mechanical spectrum, by the following relation:

$$\sqrt{\langle x^2(f)\rangle} = \frac{V_{AC}(f)}{\beta_{fib}\eta_{PD}G_{amp}P_{in}S_{\%}} \tag{71}$$

where $x(f)$ is the displacement spectral density (unit is $m/\sqrt{Hz}$) at frequency f, $V_{AC}(f)$ is the measured electrical spectral density (unit is $V/\sqrt{Hz}$) at frequency f, η_{PD}

is the quantum efficiency of the photodetector (unit is V/W), G_{amp} is the gain of the electrical amplifier, P_{in} is the input optical power, β_{fib} is the transmission factor for the fiber coupled system, and $S_{\%}$ is the sensitivity quantifies the percentage reflectance change per differential absorber gap ($\frac{dR}{dx}$,unit is $1/m$).

Using the peak voltage and the conversion factor described above, we can determine the peak displacement for the acoustic mode. If the values of η_{PD} , β_{fib} , G_{amp} , P_{in} and $S_{\%}$ are accurately known, we can calculate the peak mechanical displacement x_{peak} based on the peak voltage $V_{\max}$ corresponding to the resonance mechanical frequency by using equation (71). We can measure η_{PD} easily, get G_{amp} from the amplifier, and measure P_{in} accurately. We can also measure $S_{\%}$ from the reflectance at 1550 nm for a range of electrostatically tuned absorber gap distances. To ensure the accuracy of $S_{\%}$ at any arbitrary tuning bias, we use numerical simulation to get an almost continuous curve of the reflectance at 1550 nm, and adjust this curve linearly so that it can match the discrete measured data as shown in Figure 3-15. A continuous $S_{\%}$ curve is acquired by taking the derivative. Now we are able to calculate the mechanical amplitude with equation (71). This calibration is limited by systematic errors in the experiment. Based on this we determine the conversion factor at 1 mW in units of nm/V as 4.2, assuming the device is biased at 3.2 V.

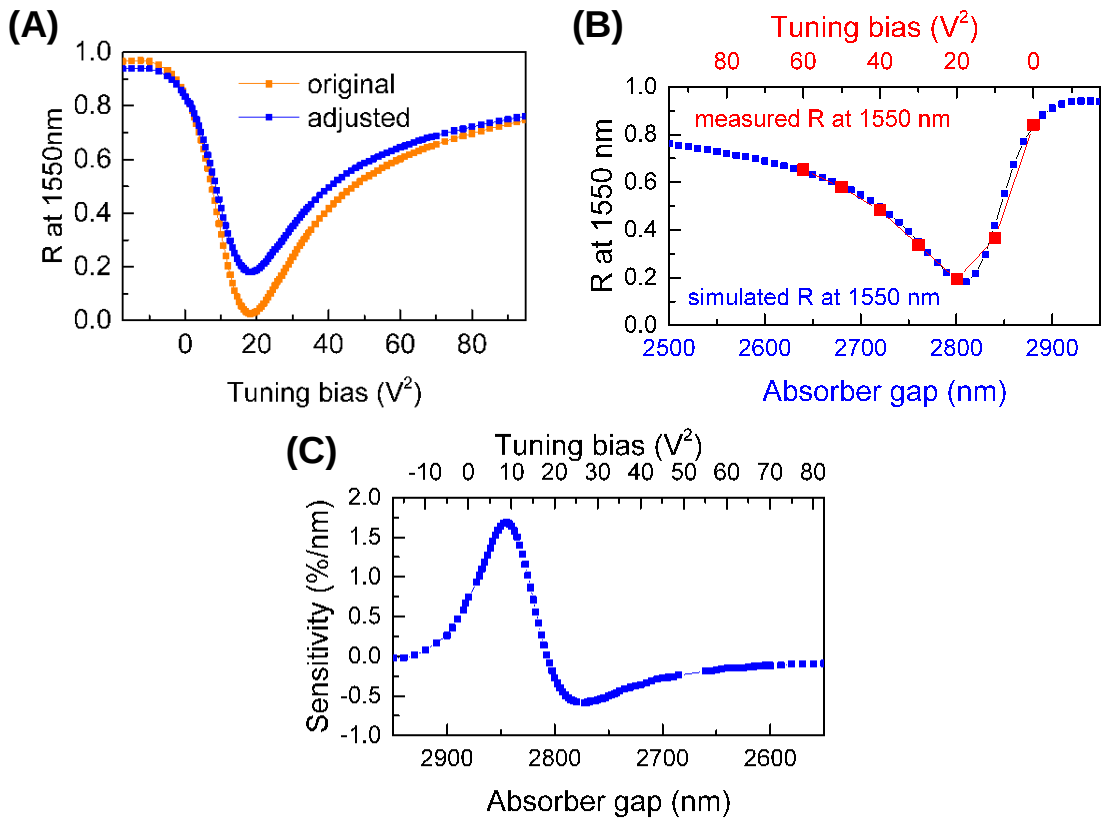

Figure 3-15. The procedure to calculate sensitivity data. (A) The original FDTD-simulated reflectance at 1550 nm wavelength is adjusted by a linear transformation, so that the adjusted simulation curve matches the measured results[5] in (B). (C) The sensitivities are calculated by taking the differential of the reflectance with respect to the absorber gap length.

3.4. Conclusions

The vibrational eigenmodes of a square membrane have been studied. We are able to characterize the mechanical oscillator by measure its mechanical spectrum through laser interferometry. In order to get the amplitude of the spectrum in the unit of length, a

[5] The optical reflection spectrum measurement will be discussed in details in Chapter 5.

calibration is needed to link voltage to meter. This can be done by consolidating optical reflection spectrum measurement and FDTD simulation data.

3.5. References

1. Timoshenko, S. and S. Woinowsky-Krieger, *Theory of plates and shells*. 2d ed. Engineering societies monographs. 1959, New York,: McGraw-Hill. 580 p.

CHAPTER 4: Opto-thermo-mechanical Coupling in the Device

4.1. Introduction

In Chapter 2, the plasmonic metamaterial absorber coupled with FP resonance has been introduced. By design, the near-perfect absorber can absorb light through the Fano resonance arising from the coupling between the plasmonic resonance and the FP resonance, which is tunable by adjusting the gap distance between the absorber and reflector plate. In Chapter 3, the membrane oscillator has been discussed. The vibrational eigenmodes of the square membrane oscillator is determined by the material properties and the geometric parameter of the square membrane.

In order to achieve optomechanical effects, optics and mechanics must be coupled to each other. The device studied in this thesis allows such coupling. The FP-coupled plasmonic resonance has mechanical dependence, since the motion of membrane causes the change in cavity length. As the light is absorbed and converted to heat, the temperature of the membrane rises. A thermal stress is then induced, causing the membrane to deflect. Therefore, the mechanics is influenced by the optics through the opto-thermo-mechanical coupling. The details of such coupling is to discuss through analytical study and FEA simulation. The thermally induced plasmomechanical force which is the root for the optomechanical effects is also explored.

4.2. Thermal Response of the Membrane

4.2.a. Heat Transfer Analysis by Green's Function

The nanoantenna array covers only a small area (~3%) of the bilayer membrane, so their impact on the mechanical and thermal properties is negligible. We will use the

uniform bilayer thin plate model to analyze the heat transfer characters, starting from solving the 2D heat equation [1]:

$$\frac{\partial^2}{\partial x^2}T(x,y,t)+\frac{\partial^2}{\partial y^2}T(x,y,t)+\frac{1}{\kappa}g(x,y,t)=\frac{1}{\alpha}\frac{d}{dt}T(x,y,t) \tag{72}$$

in $0 \le x, y \le l$, for $t > 0$,

where $T(x,y,t)$ is the temperature field, $g(x,y,t)$ is the heat generation power density in the unit of W/m^3, l is the side length of the square membrane, $\kappa \equiv \frac{t_1\kappa_1 + t_2\kappa_2}{t_1 + t_2}$ is the composite thermal conductivity, and $\alpha \equiv \frac{t_1\kappa_1 + t_2\kappa_2}{t_1\rho_1 C_1 + t_2\rho_2 C_2}$ is the composite thermal diffusivity, where $t_{1,2}$, $\kappa_{1,2}$, $\rho_{1,2}$ and $C_{1,2}$ are respectively the layer thickness, thermal conductivity, mass density and the specific heat. The membrane is placed in vacuum and its frame is in equilibrium with the ambient temperature T_0 . Therefore the second order partial differential equation (72) has the initial condition:

$$T(x,y,0)=T_0 \tag{73}$$

and the boundary condition:

$$T(0,y,t)=T(l,y,t)=T(x,0,t)=T(x,l,t)=T_0 \tag{74}$$

The heat generation density $g(x,y,t)$ is proportional to the absorbed optical power and has a spatial profile. $g(x,y,t)$ is turned on and then continually releases heat power for $t > 0$. For this type of equation and boundary conditions, the Green's function is given by [2]:

$$G\left(x,y,t\,|\,x',y',\tau\right)=\frac{4}{l^2}\sum_{m=1}^{\infty}\sum_{n=1}^{\infty}e^{-\alpha\left(\beta_m^2+\gamma_n^2\right)(t-\tau)}\sin\beta_m x\sin\gamma_n y\sin\beta_m x'\sin\gamma_n y' \tag{75}$$

where $\beta_m=m\pi/l$ and $\gamma_n=n\pi/l$. The solution of equation (72) is given by:

$$T\left(x,y,t\right)=T_0+\frac{\alpha}{\kappa}\int_{\tau=0}^{t}d\tau\int_{x'=0}^{l}\int_{y'=0}^{l}G\left(x,y,t\,|\,x',y',\tau\right)g\left(x',y',\tau\right)dx'dy' \tag{76}$$

In reality, the incident optical beam is a focused laser beam, so the heat generation function is best represented by a Gaussian profile:

$$g\left(x,y,t\right)=g_G e^{-\left[(x-l/2)^2+(y-l/2)^2\right]/r^2} \tag{77}$$

where $g_G=\dfrac{P_{abs}}{\pi r^2 d}$, where P_{abs} is the absorbed power, r and d are respectively the Gaussian beam waist size and membrane thickness, and the beam is centered at $x=y=l/2$.

Inserting the Green's function (equation (75)) and heat source (equation (77)) into equation (76), the temperature increase is readily computed by:

$$\Delta T\left(x,y,t\right)=T\left(x,y,t\right)-T_0=$$
$$\frac{4g_G}{\pi^2\kappa}\sum_{m=1}^{\infty}\sum_{n=1}^{\infty}\frac{1-e^{-\alpha\left(\beta_m^2+\gamma_n^2\right)t}}{m^2+n^2}\sin\beta_m x\sin\gamma_n y\int_{x'=0}^{l}\int_{y'=0}^{l}\sin\beta_m x'\sin\gamma_n y' e^{-\left[(x'-l/2)^2+(y'-l/2)^2\right]/r^2}dx'dy' \tag{78}$$

The above equation is the summation of all eigenfunctions, and each eigenfunction includes a time evolution term with time constant of $1/\alpha\left(\beta_m^2+\gamma_n^2\right)$. Since it is a convergent series, equation (78) can be evaluated by the adding up the most contributing low-order eigenfunctions.

At first, the temperature increase profile in steady state can be acquired by evaluating equation (78) at the limit of $t\to\infty$. For better visualization, we are to calculate

the 1D profile, e.g. the center cross section $y = l/2$, which is expressed as the following function:

$$\Delta T(x,y,t) = \frac{4g_G}{\pi^2\kappa}\sum_{m=1}^{\infty}\sum_{n=1}^{\infty}\frac{1}{m^2+n^2}\sin\beta_m x \sin\frac{\gamma_n l}{2}\int_{x'=0}^{l}\int_{y'=0}^{l}\sin\beta_m x' \sin\gamma_n y' e^{-\left[(x'-l/2)^2+(y'-l/2)^2\right]/r^2}dx'dy' \quad (79)$$

Secondly, we are interested in how the temperature increase evolves with respect to time, e.g. at the center point of the membrane $x = y = l/2$, which is basically:

$$\Delta T(x,y,t) = \frac{4g_G}{\pi^2\kappa}\sum_{m=1}^{\infty}\sum_{n=1}^{\infty}\frac{1-e^{-\alpha\left(\beta_m^2+\gamma_n^2\right)t}}{m^2+n^2}\sin\frac{\beta_m l}{2}\sin\frac{\gamma_n l}{2}\int_{x'=0}^{l}\int_{y'=0}^{l}\sin\beta_m x' \sin\gamma_n y' e^{-\left[(x'-l/2)^2+(y'-l/2)^2\right]/r^2}dx'dy' \quad (80)$$

The results of equations (79) and (80) are plotted in Figure 4-16. The relevant mechanical and thermal constants used in the computation are taken from Table 2.

Table 2. List of mechanical and thermal parameters of the materials in the bilayer membrane.

Material	Density ρ [kg m^{-3}]	Elastic Modulus E [10^{11} N m^{-2}]	Thermal Conductivity κ [W m^{-1} K^{-1}]	Thermal Expansion Coefficient γ [10^{-6} K^{-1}]	Specific Heat Capacity C [J kg^{-1} K^{-1}]	Thermal Diffusivity α [m^2 s^{-1}]
Au	19300	0.73	296	14.2	129	1.19×10^{-4}
Si_3N_4	3100	1.8	32	0.8	691	1.93×10^{-6}
Bi-L (1:4)			84.8			3.83×10^{-5}

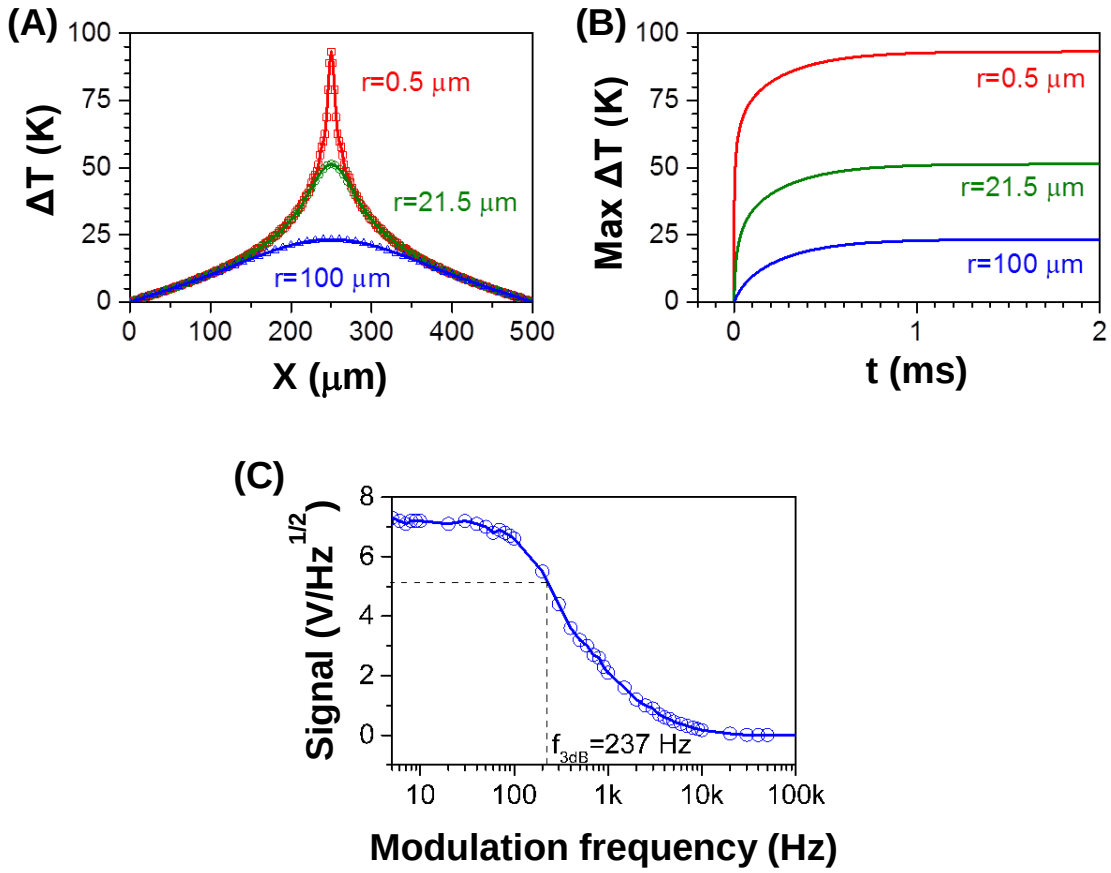

Figure 4-16. The solution of heat equation (72). (A) The steady state temperature increase distribution along the center line on the membrane by computing the series in equation (79) up to m=101 and n=101, the values of relevant mechanical and thermal constants are from Table 2. (B) The temporal evolution of max temperature increase by computing the series in equation (80) up to m=101 and n=101. (C) The thermal response of the device measured with a modulated input laser and lock-in amplifier, the 3dB frequency of 237 Hz is equivalent to a time constant of 0.67 ms.

4.2.b. Thermal Response Time Constant

The time constant for the fundamental eigenfunction is $\tau_{1,1} = \frac{l^2}{2\pi^2\alpha} = 0.33$ ms, and for the higher orders $\tau_{m,n} = \tau_{1,1} \Big/ \left(m^2 + n^2\right)$. The higher eigenfunctions reach steady state at a faster pace and meanwhile they have a smaller steady state value. As a result, the

summation of all costs a little bit less time to reach the steady state. 0.33 ms could be an estimation for the up limit of the thermal time constant. With concentrated source, the contributions from high order eigenfucntions become more significant, so the thermal time constant deviates more from 0.33 ms.

By modulating the input laser power at a spectrum of frequencies and detecting the mechanical oscillation with a lock-in amplifier, the magnitude of the thermal response was measured as a function of frequency (Figure 4-16(C)). The 3dB frequency is found to be 237 Hz and it is equivalent to a time constant of 0.67 ms. The measured result is on the same order of magnitude with the analytical one by Green's function method.

4.3. Thermomechanical Deflecion and Force on the Membrane Studied by FEM Simulations

4.3.a. Heat Transfer Results

The thermomechanical properties of the bilayer membrane have been studied by finite element simulations with COMSOL multi-physics software. The nanoantenna array covers only a small area (~3%) on the bilayer metasurface membrane, so its impact on the mechanical and thermal properties is negligible. Therefore we built the model for a uniform square membrane with a side length of 500 μm that consists of 100 nm thick silicon nitride and 25 nm thick gold layers. The mechanical and thermal properties of gold and silicon nitride are listed in Table 2.

The bilayer membrane is a thin film with very small heat capacity, and its four sides are anchored to the frame which has much larger heat capacity and quicker thermal conduction. Therefore, constant temperature boundary condition is set at the four sides.

The device is usually operated in vacuum, and its black body radiation is negligible due to relatively low temperature. Therefore, insulated boundary condition is set at the top and bottom surfaces. When light is focused onto the membrane, it is absorbed and converted into heat. The heat generation source spatial distribution depends on the optical field profile. Therefore, the heat source is assumed to be of Gaussian form ($\propto e^{-\left(\Delta x^2+\Delta y^2\right)/r^2}$, r is the optical beam waist size) centered in the middle of the membrane. Given the specifications of the optical fiber, collimator and convex lens used in the measurement system (Figure 3-14), the theoretical diameter of the focused beam spot on the membrane is about 43 μm. In practice, the beam spot size may be different. Observation with an infrared camera suggests that the focused beam spot diameter is about 41 μm (Figure 4-17), which proves the aforementioned estimation of 43 μm. Therefore, in the simulation model, the beam waist size of 21.5 μm is used for best approximation, although 0.5 μm and 100 μm are also applied to estimating the range of the results. In the following text, we will refer to the 0.5 μm, 21.5 μm and 100 μm beams as "sharp", "normal", and "wide" sources, respectively.

Figure 4-17. The IR images of the device region (left) and laser spot (right) for laser spot size estimation. The images were recorded with the same magnification and pixel configuration. The laser spot size is estimated as ~41μm based on the known width (200 μm) of electrode channel.

Setting the total heat power to 1 mW, after thermal equilibrium is reached, the temperature is highest at the center and gradually drops to room temperature at the membrane edges (Figure 4-18(A)). The max temperature increase (ΔT) is 53 K for normal source. For sharp source, ΔT reaches as high as 94 K at the center and drops rapidly if away from the center. For wide source, the max ΔT is only 24 K. The profiles of ΔT for different sources converges in the areas far away from the center. These results are consistent with the calculation by Green's function in Figure 4-16(A).

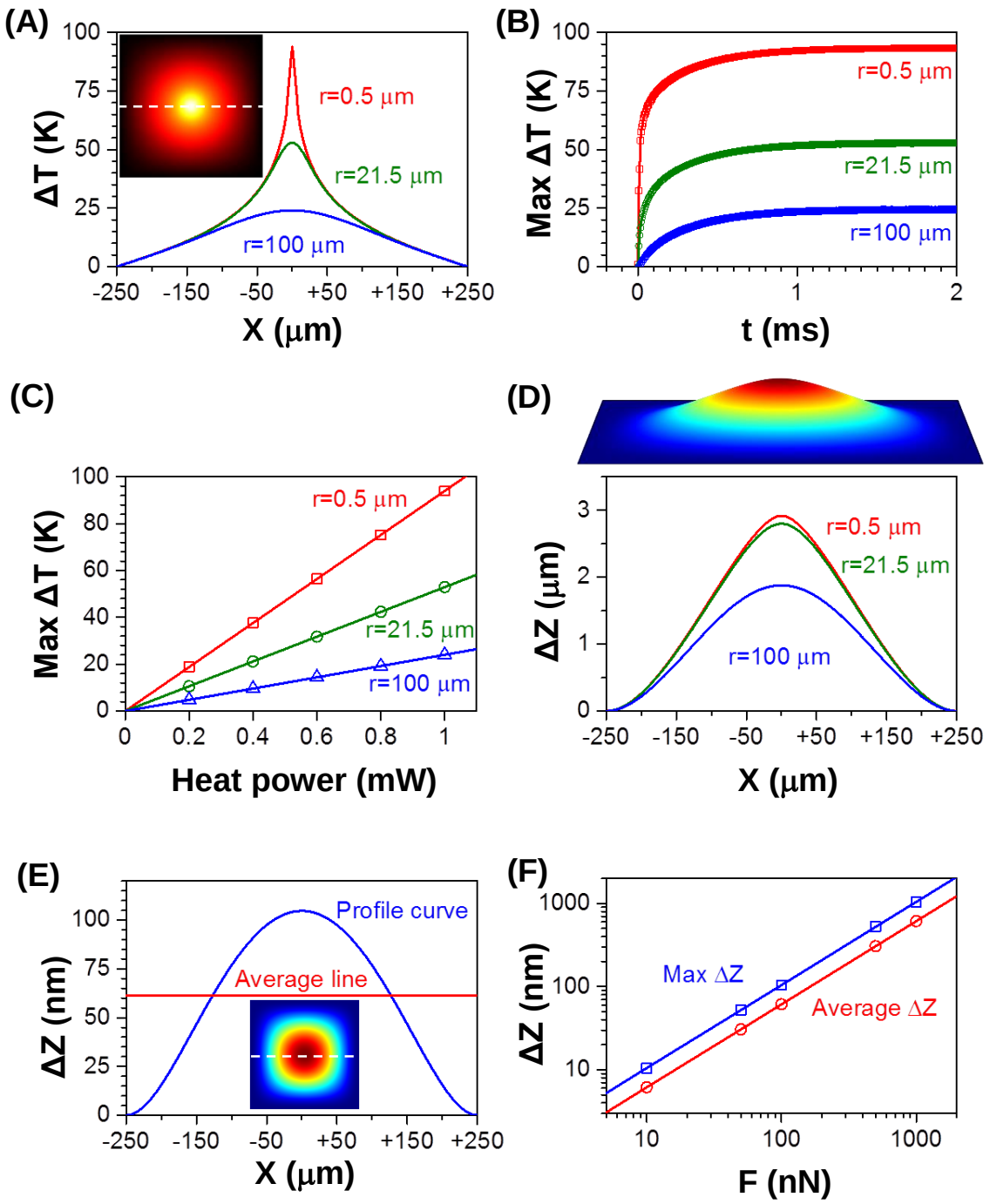

Figure 4-18. The FEA simulation results on the heat transfer and membrane deflection. (A) The steady state temperature increase ΔT distribution along the center line on the membrane (the dashed line on the inset), for different optical spot sizes but same total power of 1mW. The inset is the 2D ΔT distribution for a spot size of 21.5 μm. (B) The temporal evolution of max ΔT, which

is calculated at the center of the membrane, corresponding to (A). (C) The max ΔT scales linearly with heating absorbed optical power. (D) The typical membrane deflection profile (not up to scale). The curves are the membrane deflection (ΔZ) profiles, for the same cases as in (A). I The membrane deflection (ΔZ) profile when the membrane undergoes a uniform normal pressure of 0.4 Pa (100 nN on 500 μm by 500 μm area), and the average of the profile. (F) The max ΔZ , which occurs at the center of the membrane, and the average ΔZ scale linearly with the total uniform force. The spring constants calculated by the inverse of slope are 9.55 N/m based on max ΔZ and 16.3 N/m based on average ΔZ .

We can also estimate the thermal response in the time and frequency domains. Taking the ΔT at the center as example, Figure 4-18(B) shows the max ΔT reaches the steady state value in 2 ms. By fitting the data with $1-e^{-t/\tau}$ function, the time constant of the thermal equilibrium is found to be 0.27 ms for wide source, 0.12 ms for normal source and 0.04 ms for sharp source. The thermal time constant is an important parameter in the plasmomechanical feedback backaction force mechanism, which contributes to the optically induced mechanical damping. The thermal time constants by FEA, Green function, and measurement are all on the order of 0.1 ms.

4.3.b. Membrane Deflection and Force Estimation

Increased temperature causes material expansion, and then the membrane deflects since its edges are fixed to the rigid frame. In the case of bilayer materials, the mismatch of thermal expansion coefficients leads to the static thermoplasmonically-induced plasmomechanical forces. The multi-physics model in COMSOL can simulate the membrane deflection profile for the same heating condition. With the sharp, normal and wide sources, the deflection (ΔZ) profiles are given in Figure 4-18(D). Experiments with

similar bilayer structures have shown 5.8 times smaller deflection than the evaluation directly by COMSOL, so the results of ΔZ have been scaled down by a factor of 5.8. By analyzing the ΔZ profile curves over 50 μm range near the center, we find the averaged radius of curvature of the membrane is about 1.9 mm for the sharp and normal source and 4.5 mm for the wide source.

The deflection of the membrane is the result of the balance between the plasmomechanical compressive stress and the intrinsic elastic tensile stress. Due to symmetry, the plasmomechanically-induced stress adds up into a normal force pushing the membrane to deflect toward the gold layer while the intrinsic elastic stress adds up into a normal force pulling the membrane back to non-deflection position. The mechanical elastic force is determined by the properties of the materials, and should follow Hooke's law in the case of very small deflection. In COMSOL, a pressure force is exerted uniformly over the square membrane, and the membrane deflects until the elastic and the external forces are balanced. In this case the membrane shows a deflection profile (Figure 4-18I) very similar to that caused by heating. The spring constant of the membrane can be determined from the slope of the calculated force-deflection curve (Figure 4-18(F)). Taking the average deflection as the deflection of the membrane mechanical oscillator, we estimate that the spring constant of the membrane as 16.3 N/m. Based on this spring constant value, we can estimate the static plasmomechanical force per unit optical power to be 23 μN/mW for normal source, 24 μN/mW for sharp source, and 11 μN/mW for wide source.

4.4. An Optomechanical Device Supporting Opto-thermo-mechanical Interactions

4.4.a. Plasmomechanical Force on the Membrane Oscillator

The optomechanical device studied in this thesis consists of a silicon nitride membrane oscillator as the mechanical element and a plasmonic metamaterial absorber coupled with FP resonance as the optical element (Figure 1-1). A low-noise laser of 1550 nm wavelength is incident on the membrane. The plasmonic metamaterial absorber transforms light to thermal energy. The temperature of the membrane is raised, and a thermal stress is built. The collective effect of the thermal stress is equivalent to a normal force, named plasmomechanical force F_{pm}, and causes the membrane to deflect. The silicon nitride membrane of 100 nm in thickness is modified with a gold thinfilm in order to prepare plasmonic nanostructures. 25 nm thickness of gold thinfilm was selected, as the result of optimization of maximum deflection of the bilayer. For this bilayer membrane, the direction of thermally induced deflection is always toward the gold side. The deflection leads to the increase of elastic force pulling the membrane back, and eventually reaches balance with the plasmomechanical force (Figure 4-19(A)).

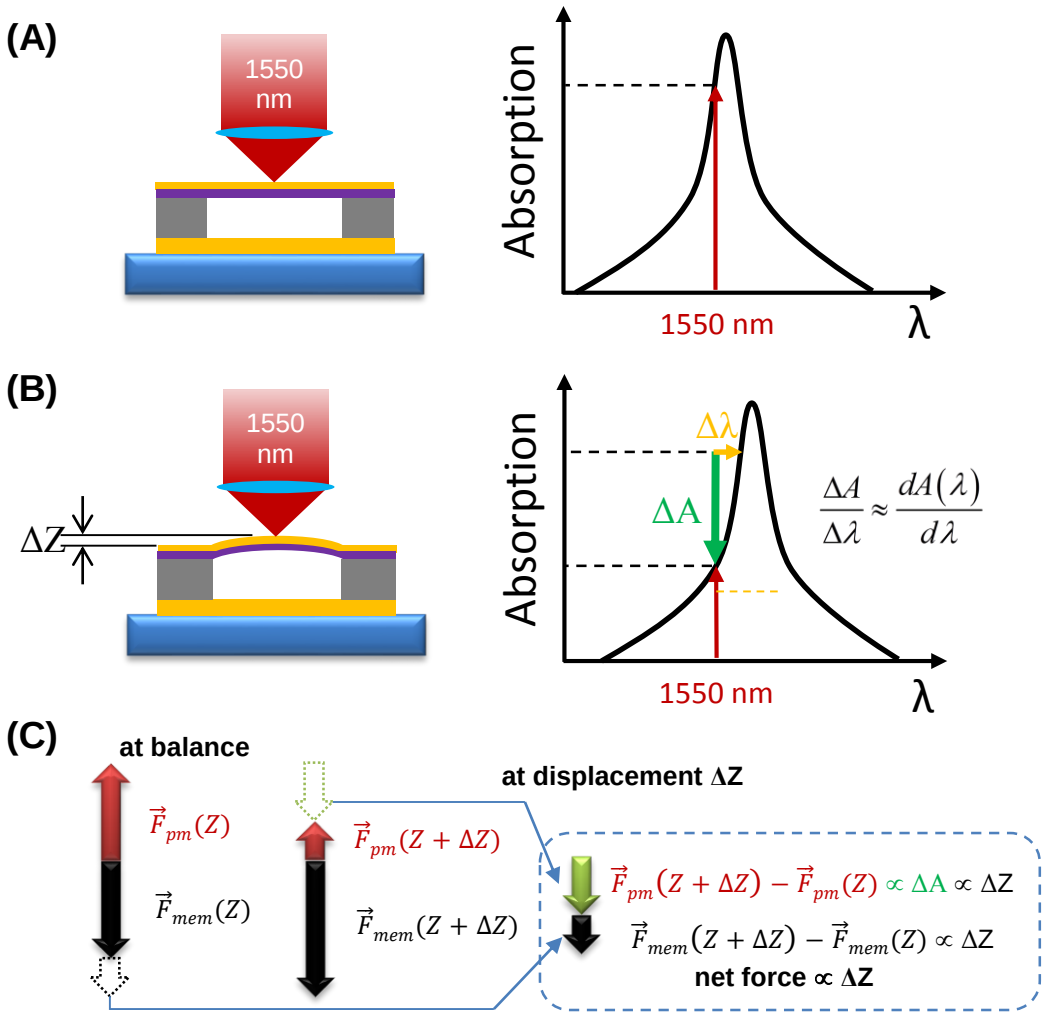

Figure 4-19. Plasmomechanical force arises from the opto-thermo-mechanical interactions. Compare to (A) the membrane at balance position, (B) the membrane at a small displacement of ΔZ exhibits a decreased absorption. Their force compositions are shown in (C), revealing that the membrane is subjected to the net plasmomechanical force $F_{pm}(\Delta Z) \propto \Delta Z$ in addition to the net membrane elastic force $F_{mem}(\Delta Z) \propto \Delta Z$.

The flexible membrane is subjected to random displacements, i.e. Brownian motion. Figure 4-19(B) illustrates the membrane deviating from the balance position by a small distance of ΔZ. Since the absorber in this device is based on the plasmonic-FP hybrid

resonances, in which the peak wavelength depends on the cavity length, the absorption peak is redshifted by $\Delta\lambda$. Both simulation and measurement results suggest that it is a linear dependence relation if the cavity length change is within a small range $\Delta\lambda \propto \Delta Z$. The shift in absorption spectrum leads to a decrease in absorption ΔA and, consequently, a decrease in the plasmomechanical force. The change in plasmomechanical force is proportional to ΔA and also ΔZ, because $\Delta A \approx \Delta\lambda \frac{dA(\lambda)}{d\lambda}$ providing $\Delta\lambda$ is very small. Meanwhile, the membrane elastic force increases due to the deflection. Figure 4-19(C) illustrates the changes of the force components. Consider the balance position as reference, the membrane is now subjected to a net plasmomechanical force and membrane elastic force, both of which are proportional to ΔZ.

The net plasmomechanical force serves as an extra elastic force and modifies the spring constant of the membrane oscillator. Different from the membrane elastic force, which is always a restoring force, the elastic plasmonmechanical force has two possible directions depending on the detuning conditions. In the case that the laser wavelength of 1550 nm is blue-detuned from the Fano resonance peak (Figure 4-19), an increase in deflection ($\Delta Z > 0$) results in a decrease in absorption ($\Delta A < 0$), so the elastic plasmomechanical force is along the direction of the restoring force and stiffens the mechanical oscillator. In the opposite case that the laser wavelength is red-detuned from the Fano resonance, an increase in deflection results in an increase in absorption ($\Delta A > 0$), so the elastic plasmomechanical force is against the direction of the restoring force and softens the mechanical oscillator.

4.4.b. Phase-delayed Plasmomechanical Forces and Their Interaction with the Osicllator System

In practice, the membrane needs some time (thermal response time τ) to be heated up to the equilibrium temperature. Therefore, the plasmomechanical force is usually delayed from the membrane elastic force by τ . In the aforementioned analysis, the delay leads to a backaction force that either amplifies or dampens the mechanical oscillations, depending on the direction of the force. A simplified harmonic oscillator model can help to understand the physical picture of the backaction effects. In an ideal lossless harmonic oscillator, the displacement and velocity vary as a sine function with the same period but a phase difference of $\frac{\pi}{2}$ (Figure 4-20(A)). The membrane elastic force is precisely synchronized to the displacement, so it can be represented by the same curve on the graph. The rate of work done by a force to the mechanical oscillator is expressed by $P(t)=\vec{F}(t)\cdot\vec{v}(t)$. $\vec{F}(t)$ and $\vec{v}(t)$ are both sine functions, so is their inner product. Usually $P(t)$ varies between positive and negative values. On the condition that the phase difference between $\vec{F}_{mem}(t)$ and $\vec{v}(t)$ is $\frac{\pi}{2}$, the time average of the rate of work $\langle P(t)\rangle = 0$ (Figure 4-20(C)). This indicates that the membrane elastic force never changes the total energy of the oscillation system.

Using this model to analyze the plasmomechanical force. If the thermal response is instantaneously $\tau << T_m$, $\vec{F}_{pm}(t)$ is in-phase with $\vec{F}_{mem}(t)$ and $\vec{v}(t)$. $\vec{F}_{pm}(t)$ is a purely elastic force and behaves like $\vec{F}_{mem}(t)$, generating zero work (Figure 4-20I). If the thermal

response is comparable to the oscillation period, $\vec{F}_{pm}(t)$ exhibits a delay in phase from $\vec{F}_{mem}(t)$ and $\vec{v}(t)$. Figure 4-20(B) exemplifies this case and shows that the work done by $\vec{F}_{mem}(t)$ is positive during the majority of one period. As a result, the mechanical oscillation is amplified with the force. If the direction of $\vec{F}_{mem}(t)$ is revered, an opposite result is obtained in Figure 4-20(D), which corresponds to the optomechanical cooling.

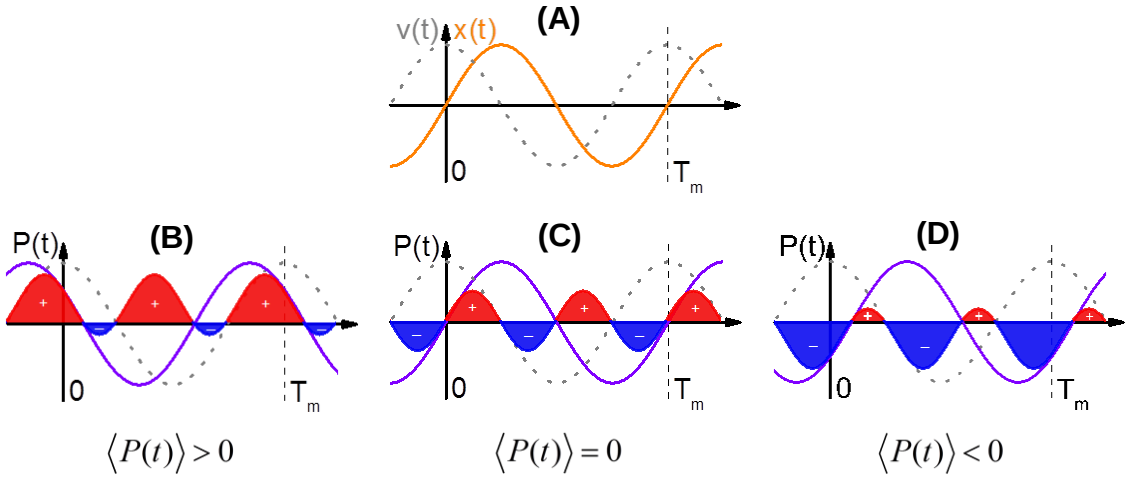

Figure 4-20. Time-varying reactive plasmomechanical force and its rate of work to the mechanical oscillator. (A) In a damping-free harmonic oscillator, the velocity $\vec{v}(t)$ (grey dashed curve) is $\frac{\pi}{2}$ after the displacement $\vec{x}(t)$ (orange curve). The rate of work done by the plasmomechanical force to the mechanical oscillator is $P(t)=\vec{F}_{pm}(\vec{x}(t))\cdot\vec{v}(t)$, and its time-varying values are exemplified in several cases where $\vec{F}_{pm}(\vec{x}(t))$ (purple curve) has different phases. (B) The optomechanical amplification scenario: $\vec{F}_{pm}(\vec{x}(t))$ is out-of-phase with $\vec{v}(t)$, and $P(t)$ is positive during most of the time in one period. (C) The unperturbed scenario: $\vec{F}_{pm}(\vec{x}(t))$ is in-phase with $\vec{v}(t)$, and $P(t)$ is positive during half of the time in one period. (D) The

optomechanical cooling scenario: $\vec{F}_{pm}\left(\vec{x}(t)\right)$ is out-of-phase with $\vec{v}(t)$ but the direction is reversed from (B), and $P(t)$ is negative during most of the time in one period.

As discussed previously, the thermal response time of this device is about 0.67 ms, orders of magnitudes longer than the oscillation period time, so there exists effective optomechanical amplification as well as cooling. In this device, the length of the FP cavity is adjustable by applying a bias voltage between the metal-coated membrane and the gold reflector. Therefore, by applying a DC voltage, the optomechanical device is able to operate at a particular mode, amplification or cooling. The same laser used for optical pumping can serve as the probe light to detect the motion of the membrane, which effectively simplifies the whole system.

4.5. Plasmomechanical-Force-Induced Optomechanical Effects Analyzed by Coupled-mode Theory

4.5.a. Coupled-mode Equations and Their Solutions

The dynamics of this opto-thermo-mechanical system coupled through the plasmomechanical effect is studied with the coupled-mode theory. The equation of motion for the high-Q membrane resonator includes a plasmomechanical force term, which couples it to the metamaterial Fano resonances described by optical temporal coupled-mode formalism [3, 4]. The optical absorption serves as a heat source term in the lumped thermal circuit model.

In this device plasmomechanical force dominates all optical forces, the following equations describe the acoustic fundamental mode coupled with optical modes through plasmomechanical effects:

$$\ddot{x} = -\Gamma_{m,0}\dot{x} - \Omega_{m,0}^2 x + \frac{B_{th}\Delta T}{m_{eff}} - \frac{F_{es}}{m_{eff}} \tag{81}$$

$$\dot{a} = -[i(\Delta_0 - g_{pm}x) + \frac{\gamma}{2}]a + \sqrt{\kappa}s \tag{82}$$

$$\Delta\dot{T} = -\gamma_{th}\Delta T + \frac{\gamma_{ant}|a|^2}{C_{th}} \tag{83}$$

where x is the membrane's displacement from equilibrium (upward is the positive direction), $\Gamma_{m,0}$ is the mechanical damping rate, $\Omega_{m,0}$ is the mechanical resonance frequency, m_{eff} is the effective mass for the fundamental acoustic membrane resonance, ($m_{eff}\Omega_{m,0}^2$ is therefore the mechanical spring constant), B_{th} is the plasmomechanical force per unit temperature , F_{es} is the electrostatic force determined by the tuning bias voltage, a is the normalized optical field in the cavity in the units of $\sqrt{J}$, $\Delta_0 = \omega_L - \omega_C$ is the frequency detuning of the laser from the Fano resonance, $g_{pm} \equiv d\omega/dx$ is the plasmomechanical coupling coefficient, γ is the optical cavity decay rate, κ is the coupling rate of the incident optical power into the metamaterial absorber, s is the incident normalized optical field in units of $\sqrt{W}$, ($\kappa|s|^2$ is the optical power injected into the metamaterial absorber), ΔT is the membrane's temperature increase, γ_{th} is the thermal

equilibrium rate of the membrane, γ_{ant} is the coupling rate of the optical power into heat and relates to the metamaterial absorbance, and C_{th} is the heat capacity of the membrane.

To solve those equations perturbatively, we set small parameter ε and expand the mechanical, optical and thermal variables to their first order:

$$x(t) = x_0 + \varepsilon x_1(t) \tag{84}$$

$$a(t) = a_0 + \varepsilon a_1(t) \tag{85}$$

$$\Delta T(t) = \Delta T_0 + \varepsilon \Delta T_1(t) \tag{86}$$

Inserting them into coupled mode equations (81-83), yielding:

$$\varepsilon \ddot{x}_1 = -\Omega_{m,0}^2 x_0 + \frac{B_{th}\Delta T_0}{m_{eff}} - \frac{F_{es}}{m_{eff}} - \varepsilon \Gamma_{m,0}\dot{x}_1 - \varepsilon \Omega_{m,0}^2 x_1 + \frac{\varepsilon B_{th}\Delta T_1}{m_{eff}} + \mathrm{O}(\varepsilon^2) \tag{87}$$

$$\varepsilon \dot{a}_1 = -[i(\Delta_0 - g_{pm}x_0) + \frac{\gamma}{2}]a_0 + \sqrt{\kappa}s - \varepsilon[i(\Delta_0 - g_{pm}x_0) + \frac{\gamma}{2}]a_1 + \varepsilon i g_{pm}x_1 a_0 + \mathrm{O}(\varepsilon^2) \tag{88}$$

$$\varepsilon \Delta \dot{T}_1 = -\gamma_{th}\Delta T_0 + \frac{\gamma_{ant}|a_0|^2}{C_{th}} - \varepsilon \gamma_{th}\Delta T_1 + \varepsilon \frac{\gamma_{ant}(a_0 a_1^* + a_0^* a_1)}{C_{th}} + \mathrm{O}(\varepsilon^2) \tag{89}$$

Keeping terms to zeroth order of ε and defining the equilibrium laser detuning $\Delta_0' \equiv \Delta_0 - g_{pm}x_0$ yields the unperturbed solutions of the coupled mode equations (81-83):

$$x_0 = \frac{B_{th}\Delta T_0 - F_{es}}{m_{eff}\Omega_{m,0}^2} \tag{90}$$

$$a_0 = \frac{\sqrt{\kappa}s}{i\Delta_0' + \gamma/2} \tag{91}$$

$$\Delta T_0 = \frac{\gamma_{ant}|a_0|^2}{\gamma_{th}C_{th}} \tag{92}$$

Keeping terms to first order of ε yields:

$$\ddot{x}_1 = -\Gamma_{m,0}\dot{x}_1 - \Omega_{m,0}^2 x_1 + \frac{B_{th}\Delta T_1}{m_{eff}} \tag{93}$$

$$\dot{a}_1 = -[i\Delta_0' + \frac{\gamma}{2}]a_1 + ig_{pm}x_1 a_0 \tag{94}$$

$$\Delta\dot{T}_1 = -\gamma_{th}\Delta T_1 + \frac{\gamma_{ant}\left(a_0 a_1^* + a_0^* a_1\right)}{C_{th}} \tag{95}$$

Take the Fourier transform of those first-order perturbation equation (94) and its conjugate, and (95) as well, yielding these algebraic equations:

$$i\omega a_1 = -[i\Delta_0' + \frac{\gamma}{2}]a_1 + ig_{pm}x_1 a_0 \tag{96}$$

$$i\omega a_1^* = -[-i\Delta_0' + \frac{\gamma}{2}]a_1^* - ig_{pm}x_1^* a_0^* \tag{97}$$

$$i\omega\Delta T_1 = -\gamma_{th}\Delta T_1 + \frac{\gamma_{ant}\left(a_0 a_1^* + a_0^* a_1\right)}{C_{th}} \tag{98}$$

Writing a_1 and a_1^* in terms of a_0 and a_0^* respectively with equations (96) and (97), we can get:

$$a_0 a_1^* + a_0^* a_1 = ig_{pm}x_1\left[\frac{1}{i\left(\omega + \Delta_0'\right) + \gamma/2} - \frac{1}{i\left(\omega - \Delta_0'\right) + \gamma/2}\right]\cdot\left|a_0\right|^2 \tag{99}$$

Defining the constant:

$$C \equiv \frac{g_{pm}\gamma_{ant}B_{th}}{C_{th}} \tag{100}$$

and the transfer function:

$$f\left(\omega,\Delta_0'\right)=\frac{1}{i\omega+\gamma_{th}}\left[\frac{1}{i\left(\omega+\Delta_0'\right)+\gamma/2}-\frac{1}{i\left(\omega-\Delta_0'\right)+\gamma/2}\right] \tag{101}$$

By inserting Eq. (S.34-36) back into Eq. (S.33), we have:

$$\Delta T_1=i\frac{C}{B_{th}}\left|a_0\right|^2\cdot f\left(\omega,\Delta_0'\right)x_1 \tag{102}$$

We assume the membrane is oscillating harmonically near the equilibrium position with an amplitude of ε , so

$$x_1=1\cdot\cos\left(\Omega_{m,0}t\right)\text{ and }x_1=\sqrt{\pi/2}\left[\delta\left(\omega+\Omega_{m,0}\right)+\delta\left(\omega-\Omega_{m,0}\right)\right].$$

In addition, $f\left(\omega\right)$ is an anti-Hermitian function, i.e. $f\left(-\omega\right)=-f^*\left(\omega\right)$. To obtain the solution in time domain, we take the inverse Fourier transform of equation (102):

$$\Delta T_1=i\frac{C}{B_{th}}\left|a_0\right|^2\cdot\frac{1}{\sqrt{2\pi}}\int_{-\infty}^{+\infty}f\left(\omega,\Delta_0'\right)\sqrt{\frac{\pi}{2}}\left[\delta\left(\omega+\Omega_{m,0}\right)+\delta\left(\omega-\Omega_{m,0}\right)\right]e^{+i\omega t}d\omega \tag{103}$$

which is then reduced to:

$$\Delta T_1=i\frac{C}{B_{th}}\left|a_0\right|^2\cdot\frac{1}{2}\left[f\left(\Omega_{m,0},\Delta_0'\right)e^{i\Omega_{m,0}t}-f^*\left(\Omega_{m,0},\Delta_0'\right)e^{-i\Omega_{m,0}t}\right] \tag{104}$$

which is then reorganized to:

$$\Delta T_1=-\frac{C}{B_{th}}\left|a_0\right|^2\cdot\left\{\mathrm{Im}\left[f\left(\Omega_{m,0},\Delta_0'\right)\right]\cos\left(\Omega_{m,0}t\right)+\mathrm{Re}\left[f\left(\Omega_{m,0},\Delta_0'\right)\right]\sin\left(\Omega_{m,0}t\right)\right\} \tag{105}$$

and, finally, is rewritten as a function of x_1:

$$\Delta T_1=-\frac{C}{B_{th}}\left|a_0\right|^2\cdot\left\{\mathrm{Im}\left[f\left(\Omega_{m,0},\Delta_0'\right)\right]x_1-\mathrm{Re}\left[f\left(\Omega_{m,0},\Delta_0'\right)\right]\frac{\dot{x}_1}{\Omega_{m,0}}\right\} \tag{106}$$

In equation (81), we introduced the thermoplasmonic force $F_{th} = B_{th}\Delta T = B_{th}\left(\Delta T_0 + \varepsilon \Delta T_1\right)$. The dynamic reactive part ($\propto \Delta T_1$), revealed by equation (106), consists of in-phase and quadrature contributions. As a result, we expect such plasmomechanical force to modify the spring constant and damping rate of the membrane. To quantify these effects, we use equation (91) to substitute the $\left|a_0\right|^2$ term in equation (106) and then insert it into equation (93) to yield:

$$\begin{aligned}\ddot{x}_1 = &-\left\{\Gamma_{m,0} - \frac{C}{m_{eff}\Omega_{m,0}}\kappa\left|s\right|^2 \frac{\mathrm{Re}\left[f\left(\Omega_{m,0},\Delta_0'\right)\right]}{\Delta_0'^2 + \gamma^2/4}\right\}\dot{x}_1 \\ &-\left\{m_{eff}\Omega_{m,0}^2 + C\kappa\left|s\right|^2 \frac{\mathrm{Im}\left[f\left(\Omega_{m,0},\Delta_0'\right)\right]}{\Delta_0'^2 + \gamma^2/4}\right\}\frac{x_1}{m_{eff}}\end{aligned} \tag{107}$$

By defining the overall transfer function:

$$h\left(\Omega_{m,0},\Delta_0'\right) = \frac{f\left(\Omega_{m,0},\Delta_0'\right)}{\Delta_0'^2 + \gamma^2/4} \tag{108}$$

the effective damping rate and spring constant (normalized to mass) are:

$$\Gamma_{m,eff} = \Gamma_{m,0} - \frac{C}{m_{eff}\Omega_{m,0}}\kappa\left|s\right|^2 \cdot \mathrm{Re}\left[h\left(\Omega_{m,0},\Delta_0'\right)\right] \tag{109}$$

$$\Omega_{m,eff}^2 = \Omega_{m,0}^2 + \frac{C}{m_{eff}}\kappa\left|s\right|^2 \cdot \mathrm{Im}\left[h\left(\Omega_{m,0},\Delta_0'\right)\right] \tag{110}$$

Equations (109) and (110) indicate that the plasmomechanically induced modifications to mechanical damping rate and spring constant depend on the following parameters:

B_{th} (plasmomechanical force coefficient, determined by the material properties),

g_{pm} (plasmomechanical coupling strength, determined by the absorber gap),

γ_{ant} (heat generation rate, determined by the metamaterial absorbance),

$1/C_{th}$ (inverse of thermal mass, determined by the material properties),

κ (input-output coupling rate, determined by optical damping),

and the incident optical power $|s|^2$, which can be controlled in experiment.

Equations (109) and (110) also show that the plasmomechanically induced dampingis modulated by an odd function of detuning Δ_0', ($h(-\Delta_0') = -h(\Delta_0')$). Therefore red and blue detunings lead to opposite plasmomechanical effects.

4.5.b. The Solutions in unresolved sideband limit and adiabatic limit

For the device of study, $\gamma \sim 10^{12}$ Hz, $\Omega_{m,0} \sim 10^5$ Hz, $\gamma_{th} \sim 10^3$ Hz, which is in the unresolved sideband limit ($\Omega_{m,0} \ll \gamma$) and the adiabatic limit ($\Omega_{m,0} \gg \gamma_{th}$). With these approximations along with $\Omega_{m,0}^2 / \gamma_{th}\gamma \ll 1$ and $\Delta'_{0,\max} \sim \gamma$, we can approximate the overall transfer function equation (108), and then rewrite equations (109) and (110) to get:

$$\Gamma_{m,eff} \simeq \Gamma_{m,0} + \frac{g_{pm}\gamma_{ant}B_{th}}{C_{th}m_{eff}\Omega_{m,0}^2}\kappa|s|^2 \cdot \frac{2\Delta_0'}{\left(\Delta_0'^2 + \gamma^2/4\right)^2} \tag{111}$$

$$\Omega_{m,eff}^2 \simeq \Omega_{m,0}^2 - \frac{g_{pm}\gamma_{ant}B_{th}\gamma_{th}}{C_{th}m_{eff}\Omega_{m,0}^2}\kappa|s|^2 \cdot \frac{2\Delta_0'}{\left(\Delta_0'^2 + \gamma^2/4\right)^2} \tag{112}$$

Equation (111) is useful to fit measured mechanical resonance linewidth data for a fixed incident optical power at different detunings.

For a Lorentzian absorption resonance:

$$L(\xi) = \frac{Const}{2\pi} \frac{\Gamma}{(\xi - \xi_0)^2 + (\Gamma/2)^2} \tag{113}$$

the slope of the lineshape is:

$$\frac{dL(\xi)}{d\xi} = -\frac{Const\Gamma}{\pi} \frac{(\xi - \xi_0)\Gamma}{(\xi - \xi_0)^2 + (\Gamma/2)^2} \tag{114}$$

Assume the spectral absorbance is:

$$A(\omega) = \frac{Const}{2\pi} \frac{\gamma}{\Delta_0'^2 + (\gamma/2)^2} \tag{115}$$

We can derive the gradient of plasmomechanical force F_{th}:

$$\nabla F_{th} = \frac{dF_{th}(x)}{dx} \propto \frac{dA(\omega_0)}{dx} = \frac{dA(\omega_0)}{d\omega_0} \cdot \frac{d\omega_0}{dx} \propto \frac{\Delta_0'}{\Delta_0'^2 + (\gamma/2)^2} \cdot g_{pm} \tag{116}$$

This result suggests that the plasmomechanically induced damping depends linearly on the force gradient:

$$\Gamma_{m,eff} - \Gamma_{m,0} \propto \nabla F_{pth} \tag{117}$$

$$\Omega_{m,eff}^2 - \Omega_{m,0}^2 \propto \nabla F_{pth} \tag{118}$$

Equation (81) implies that $m_{eff}\Omega_{m,0}^2 = K_m$ is the mechanical spring constant. Equations (111) and (112) indicate:

$$\Gamma_{m,eff} - \Gamma_{m,0} \propto K_m^{-1} \tag{119}$$

$$\Omega_{m,eff}^2 - \Omega_{m,0}^2 \propto K_m^{-1} \tag{120}$$

The conclusions in equations (117-120) agree with the time-delayed force model by Karrai et al. [5, 6]

In summary, the plasmomechanical coupling modifiesthe mechanical damping rate and the resonance frequency. Larger metamaterial absorbance and plasmomechanical deflection produce larger effects. The modification is inversely proportional to the mechanical spring constant, therefore softer or more flexible mechanical resonators are preferable. The plasmomechanical damping is largest at $\Delta' = \pm\gamma/2$ where ∇F_{th} is maximized. Finally, $\Gamma_{m,eff}$ and $\Omega_{m,eff}^2$ scale linearly with incident optical pump power at any given detuning.

4.6. Conclusions

Through the plasmonic metamaterial absorber, the light is absorbed to heat up the membrane. The analytical solution and FEA simulation give consistent result on the membrane temperature rise. It is estimated that the maximum temperature rise is about 53 K per mW of absorbed light power if a Gaussian light spot of a similar size is assumed. The time constant for the system to reach thermal equilibrium is estimated to be on the order of 0.1 ms, and the measurement with a modulated laser confirms that the thermal time constant is 0.66 ms. FEA simulation also shows that the thermally induced stress causes the membrane to deflect. Such deflection is proportional to the maximum temperature rise and, hence, to the absorbed light power.

By integrating the FP-coupled plasmonic metamaterial absorber and the membrane oscillator, this device allows opto-thermo-mechanical couplings. The intimate interactions

between optics and mechanics lead to a reactive plasmomechanical force, which may do positive work to the oscillator, i.e. decreasing the damping rate or amplifying the mechanical oscillation, or do negative work to the oscillator, i.e. increasing the damping rate or cooling the mecahnical oscillation.

4.7. References

1. Bergman, T.L., et al., *Fundamentals of heat and mass transfer*. 7th ed. 2011, Hoboken, NJ: Wiley. xxiii, 1048 p.
2. Özışık, M.N., *Heat conduction*. 2nd ed. 1993, New York: Wiley. xvii, 692 p.
3. Fan, S.H., W. Suh, and J.D. Joannopoulos, *Temporal coupled-mode theory for the Fano resonance in optical resonators.* Journal of the Optical Society of America a-Optics Image Science and Vision, 2003. **20**(3): p. 569-572.
4. Woolf, D., et al., *Optomechanical and photothermal interactions in suspended photonic crystal membranes.* Optics Express, 2013. **21**(6): p. 7258-7275.
5. Metzger, C.H. and K. Karrai, *Cavity cooling of a microlever*. Nature, 2004. **432**(7020): p. 1002-1005.
6. Metzger, C., et al., *Optical self cooling of a deformable Fabry-Perot cavity in the classical limit.* Physical Review B, 2008. **78**(3).

CHAPTER 5: Device Fabrication and Electrostatic Tuning Test

5.1. Introduction

Although the modern nanofabrication techniques derived from the semiconductor manufacture industry have developed capabilities of making precise and fine patterns for plasmonic nanostructures, it is still difficult to fabricate this novel optomechanical device based on plasmonic metamaterial absorber. The major challenge is from the substrate: a suspended silicon nitride membrane of 100 nm in thickness. Silicon nitride is a robust material in all physical properties, but very fragile in the form of a nanometer thin membrane on a small window frame. Besides handling the substrate and sample cautiously, the conditions or recipes for individual processes need optimization, as the nanomembranes are very different from common silicon wafers/chips.

During the fabrication and after the device is completed, necessary characterization needs performing in order to ensure the device meets the design requirement and prepare for the optomechanical effect measurement.

5.2. Fabrication Flow of the Device

5.2.a. The Fabrication Process of the Membrane Chip

Figure 5-21 illustrates the major steps for the membrane chip fabrication. The membrane chip is fabricated with a commercially available LPCVD-grown low-stress silicon nitride membrane on silicon frame. The silicon frame is a square chip of 7.5 mm by 7.5 mm by 200 μm, and there is a square window in the center making the membrane suspended freely. The freestanding membrane on the window is 500 μm by 500 μm by 100

nm and leveled to the front surface of the chip, while the back surface has a square hole with sloped sidewalls. At first, 23 nm of gold film is deposited after 2 nm adhesive layer of titanium is deposited by e-beam evaporation on the back surface of the chip. Because of the sloped sidewall of the window, the gold film on the (back surface of) membrane and the (back surface of) silicon frame are electrically conducting.

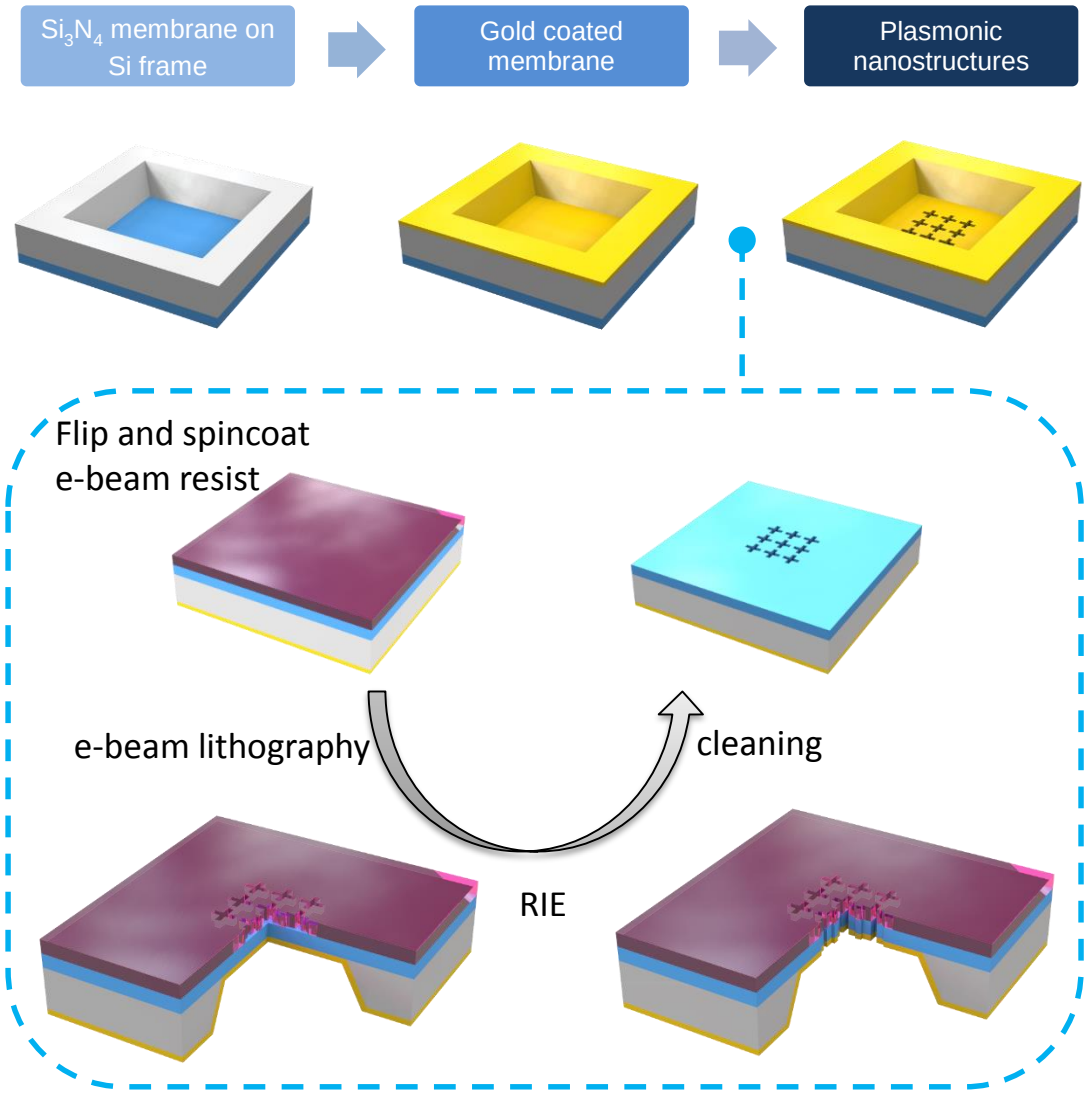

Figure 5-21. The major fabrication steps for the membrane chip.

The second step is to use e-beam lithography to define nanoantenna patterns on the front surface of the membrane. The typical film thickness of ZEP-520A and PMMA 495 A8 after spin-coating are about 400 ~ 500 nm, which is adequate as the mask for the subsequent dry etch step. ZEP-520A requires lower exposure dose (~200 $\mu C/cm^2$) but exhibits poor adhesion to common hard substrates. PMMA 495 A8 requires higher exposure dose (~600 $\mu C/cm^2$) but is more adhesive. The Elionix ELS-7500EX e-beam writer system with max acceleration voltage of 50 kV has a minimum e-beam spot diameter of 2 nm. It is capable to handle patterns required for the nanoslot antennas in this device, which are 360 nm in length and 100 nm in width, and are arranged in square lattice with a period of 800 nm. There are totally 300 by 300 antenna elements exposed at the center of the membrane. After exposure, the ZEP-520A resist is developed in O-xylene for 1 min at room temperature and cleaned in IPA for 30 seconds; the PMMA 495 A8 resist is developed in the MIBK:IPA 1:3 solution for 1 min at room temperature and cleaned in IPA for 30 seconds. Usually there is an offset of the product feature from the mask pattern, so the mask design must be corrected after one or two trial exposures.

Finally, the membrane chip undergoes a dry etch step that removes the 100 nm of silicon nitride and 25 nm of metal under the mask opening. The remaining e-beam resist and any organic residues are removed afterwards by solvents and Piranha solution. At this stage, the nanoantenna fabrication is completed.

After the gold/titanium thinfilm is deposited on the back side of the membrane chip, the membrane window is inspected with an optical profilometer in order to detect whether the physical vapor deposition process introduced a large stress in the hetero-material

interface if the deposition is at a higher temperature. The optical profilometer tests suggest that the 25 nm of gold/titanium thinfilm deposited by e-beam evaporation did not introduce excessive stresses on the 100 nm of silicon nitride membrane, on the condition of a deposition rate of 0.2 Å/s and sufficient water cooling stage.

After the membrane chip fabrication is completed, optical microscope exam should be done first to make sure there is no major defect or contamination on the structure. An optical reflection spectrum test is acquired to verify the optical property of plasmonic nanostructures. The nanoscale features of the nanoslot antenna array is revealed in high resolution in Figure 5-22.

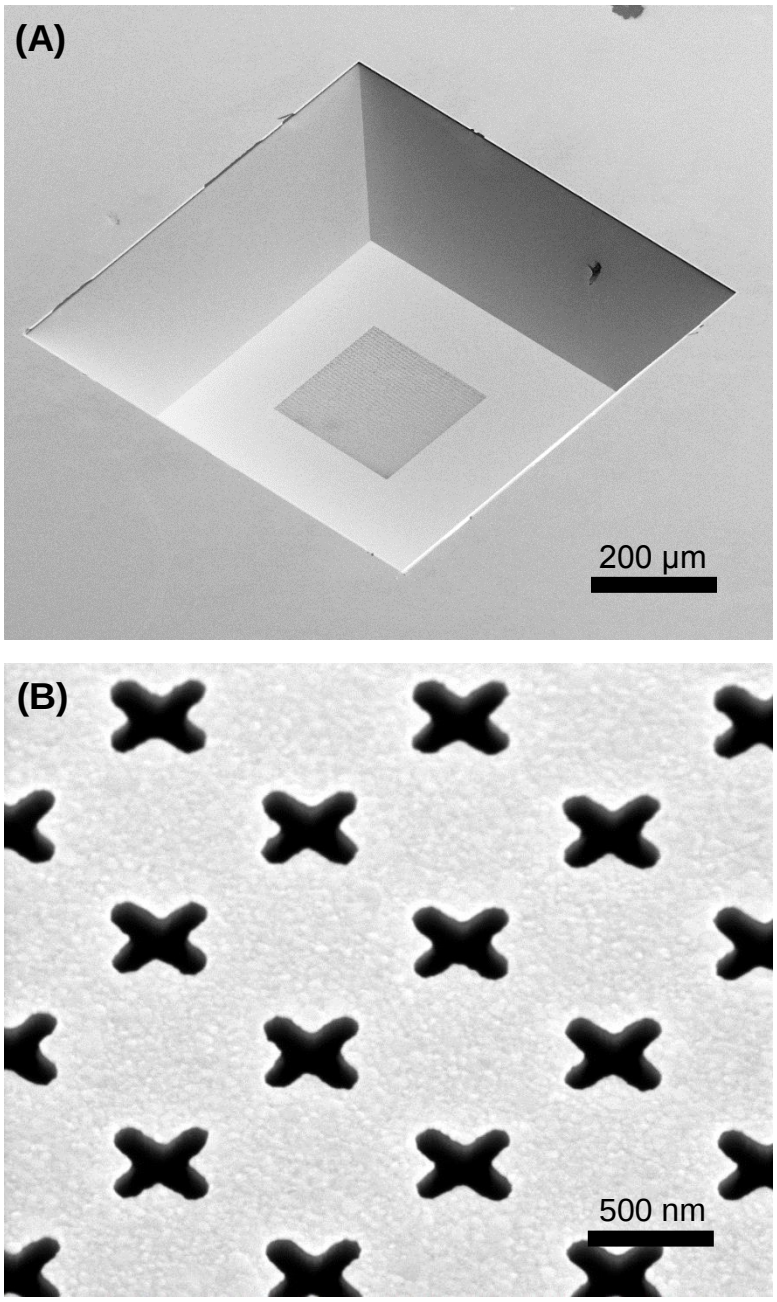

Figure 5-22. SEM images of the absorber. (A) The square area (240 μm by 240 μm) at the center of the membrane window is the plasmonic nanostructures (metasurface). (B) The close-up of cross-shaped hole array on the bilayer membrane, wherein length is about 360 nm, the width is about 100 nm, and the period of the square array is 800 nm.

5.2.b. The Fabrication Process of the Device Base

Figure 5-23 illustrates the major steps for the device base fabrication. The device base fabrication starts from a high-resistivity silicon substrate. In order to complete the alignment in infrared for the optomechanical test, a double-polished silicon substrate is required. At first, 2 μm of silicon dioxide is deposited on the silicon substrate by PECVD.

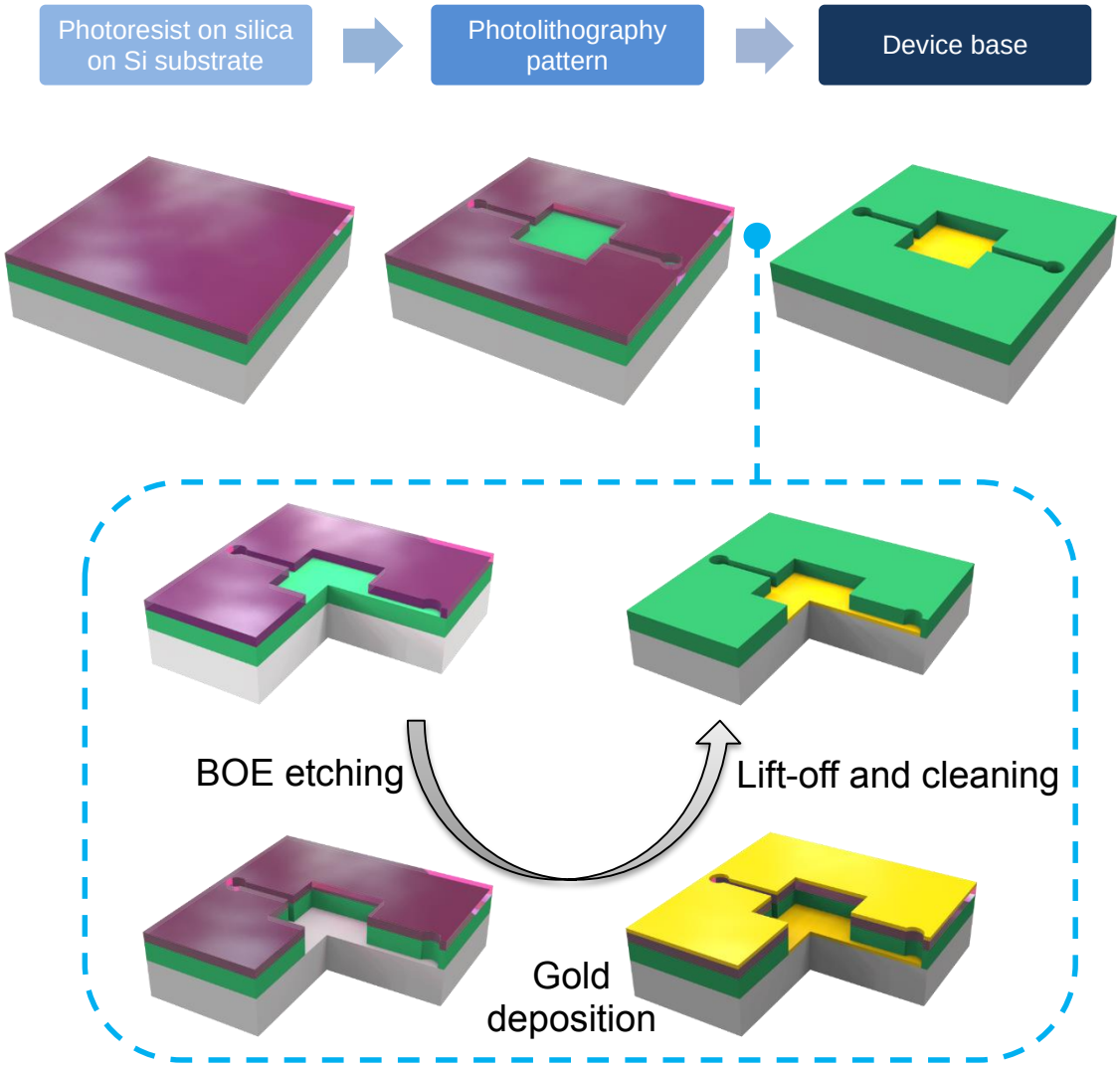

Figure 5-23. The major fabrication steps for the device base.

The second step is to define the pattern of the trench and channel by photolithography. A layer of positive photoresist (S1818) is spin-coated on the substrate with oxide and exposed with g-line under the mask. After developed in MF-319 solution and cleaned in DI water, the substrate is dipped in buffered oxide etch (BOE) to remove the silicon dioxide under the mask opening. The etching stops at the silicon substrate and the substrate is then washed in de-ionized (DI) water. After it is dried, 45 nm of gold after 5 nm of titanium thinfilm is deposited onto the substrate by e-beam evaporation. The excess gold is then removed by a lift-off process in the Remover 1165 solution, leaving the substrate with gold pattern as the back reflector and electrode. It should be noticed that gold pattern is much lower than the substrate surface because the oxide film thickness is about 2 μm but the gold/titanium film thickness is only 50 nm.

5.2.c. The Bonding Process

The device is finally completed by bonding the membrane chip (front surface of the frame) to the base (surface of the oxide layer) with minimum amount of low-viscosity polymer adhesives, e.g. cyanoacrylate. The membrane window is precisely aligned to the back reflector. The gold back reflector is 2 μm below the oxide surface and the polymer layer between the oxide surface and membrane frame is usually less than 1 μm. Figure 5-24 illustrates the bonding process as well as an example of a completed device.

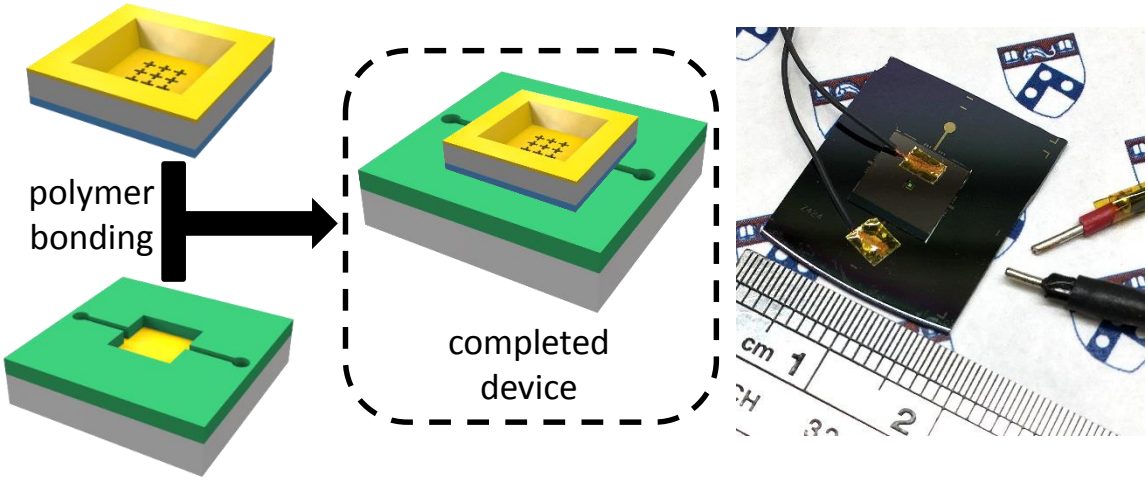

Figure 5-24. The membrane chip is bonded to the device base to make the completed device, the right photo demonstrates a real device wherein the "green lighting spot" at the center is the plasmonic metamaterial absorber area.

5.3. Optical Spectroscopy Study of the Device

5.3.a. Parallel Plate Capacitor Model

The metamaterial absorber supports tunable Fano resonances, which is produced by the coupling between the FP and plasmonic modes. The absorption spectral peak depends on the PF resonance and, hence, sensitively depends on the absorber gap distance, which can be tuned by electrostatic forces induced by a bias voltage applied between the metasurface electrode and the reflector electrode.

A parallel plate capacitor model is adequate to estimate the electrostatic force acting on the membrane. If a bias voltage V_{DC} is applied between the membrane and bottom plate separated by a distance D_{gap}, the electrostatic force given by Coulomb's law is

$F_{es} = \frac{A\varepsilon_0 V_{DC}^2}{2D_{gap}^2}$, where A is the area and ε_0 is the vacuum permittivity. The membrane would be displaced by δD where the electrostatic force is in balance with the elastic force due to intrinsic tensile stress:

$$\frac{A\varepsilon_0 V_{DC}^2}{2\left(D_{gap} - \delta D\right)^2} = K_m \delta D \tag{121}$$

In the small displacement limit $\delta D \ll D_{gap}$, equation (121) yields $\delta D \propto V_{DC}^2$. The displacement of the membrane approximately scales with the square of the tuning bias voltage, and the absorber gap distance exhibits linear relation with the square of bias voltage:

$$D_{gap} = A_1 + A_2 V_{DC}^2 \tag{122}$$

5.3.b. Linking the Gap Distance to the Bias Voltage by Optical Spectra

In order to verify the tuning function and prepare for the optomechanical tests, optical absorption spectra of the device for various voltages are measured. The absorbance is acquired by the directly measured reflection spectra, based on the fact that the absorption and reflection add up to unity because there is nearly zero transmission in the device. Figure 5-26(A) shows the absorption spectra by simulation for the optomechanical device in the condition of bias voltage tuning at 5.5 V. The measured spectrum shown in Figure 5-26(B) exhibits good agreement with the simulation. At 5.5 V, the laser of 1550 nm is detuned from the Fano peak to the red side. The so called red-detuning corresponds to the optomechanical cooling effect. At 3.2 V, the laser of 1550 nm is detuned from the Fano

peak to the blue side. The so called blue-detuning corresponds to the optomechanical amplification effect.

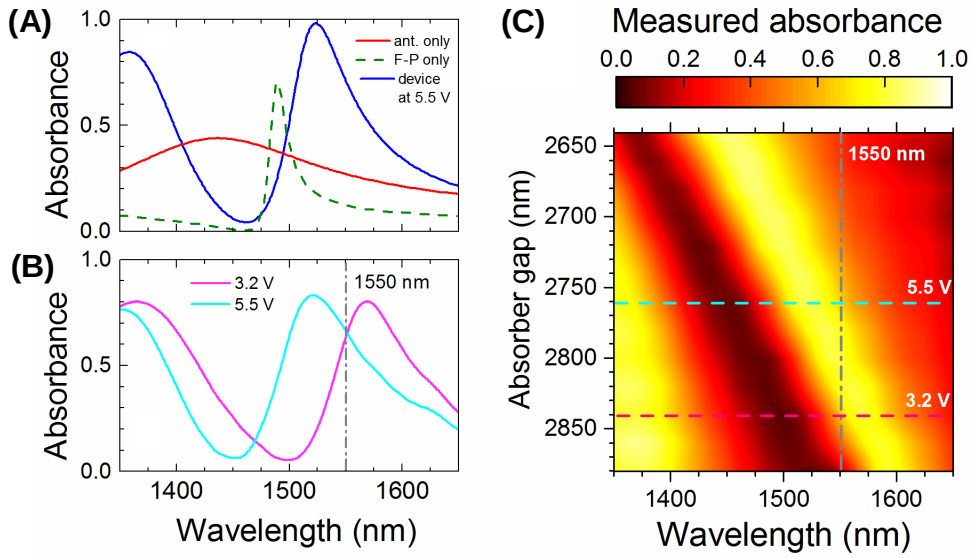

Figure 5-25. Blue and red detuning of the Fano resonance in the device. (A) Simulated spectral absorbance for the optomechanical device (blue curve): The Fano resonance arises from the coupling between the FP (green dashed curve) and plasmonic resonance (red curve). The Fano resonance peak position is voltage tunable, and the results shown are for the device biased at 5.5 V, where the absorbance peak nearly reaches unity. (B) Measured metamaterial absorption spectra of the device biased at 3.2 V (magenta dashed line in (C)) and 5.5 V (cyan dashed line in (C)) corresponding, respectively, to the cases where the 1550 nm laser (vertical grey line) is detuned to the blue and red side from the Fano peak. (C) Measured spectral absorbance for a range of absorber gaps. The Fano peak wavelength (yellow-white region) tunes linearly with the absorber gap.

The aforementioned simulation results (Figure 2-10) showed that the peak shift is linear to the change of the cavity length providing such change is within a relative small range. Therefore, a linear relation between the spectral peak wavelength and the square of the bias voltage is expected. In the tuning spectral measurements, the applied bias voltages are selected so that the square of voltage are evenly spaces, e.g. $0\,\mathrm{V}$, $\sqrt{10}\ \mathrm{V}$, $\sqrt{20}\ \mathrm{V}$,…

The absorption spectra at those bias voltages indeed show a linearly blueshift in the peak positions (Figure 5-25). By the fabrication design, the initial absorber gap distance is between 2 μm to 3 μm, because the thickness of the cyanoacrylate adhesive layer is not precisely controllable. In order to estimate the absorber gap of the device, FDTD simulations were ran for the absorber gap at every 10 nm in that range. As expected, the simulated spectra are blueshifted linearly in respect to evenly decreased absorber gap distances.

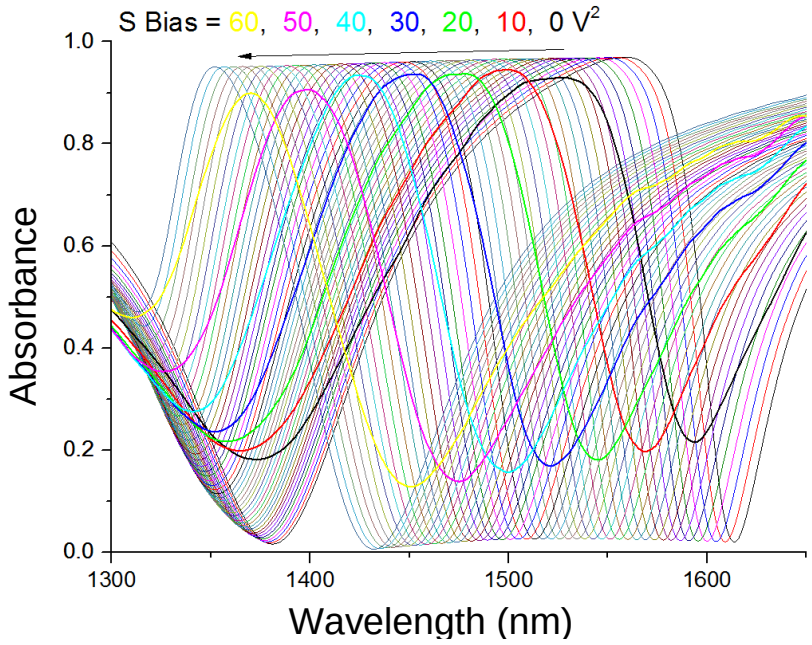

Figure 5-26. Device absorbance spectra by measurement and simulation. The measured spectra at 0, 10, 20, 30, 40, 50, and 60 in the unit of square of voltage are plotted with the bold curves, showing a linear blueshift. The simulated spectra are corresponding to the absorber gap distances from 2950 nm to 2500 nm with 10 nm change step between each spectrum, also exhibiting a linear blueshift.

In order to relate absorber gap distance and the square of the bias voltage, the reflection at 1550 nm from simulation and measurement are collected. At first, the

simulated reflection data are adjusted (normalized) to match the shape of the measured data (Figure 3-15). By interpolation, the absorber gap distance $D_{gap,itpl}$ for the measured reflection are obtained. The constants A_1 and A_2 are found by minimizing the sum of the squared residuals $\frac{1}{N}\sum_{i=1}^{N}\left[D_{gap,itpl,i} - D_{gap}\left(V_{DC,i}\right)\right]^2$ in Matlab. For this device, the relation is found: $D_{gap} = 2880 - 4V_{DC}^2$ (nm).

Although the device is always directly set to a bias voltage in experiments, absorber gap is used to represent the tuning because it is more intuitive. Figure 5-26(C) shows the measured spectral absorbance over a range of absorber gaps.

5.4. Conclusions

The optomechanical device integrated by plasmonic metamaterial absorber on a membrane oscillator and a gold reflector and electrode is able to be fabricated by metal deposition, lithography, and etching processes. The membrane chip and device base are fabricated separately and bonded by low-viscosity adhesives. Imaging inspection confirms the plasmonic nanostructures were successfully formed. Optical spectroscopy characterization is carried to verify the existence of the Fano resonance and its tunability under bias voltage. By comparing the spectra measured at different bias voltages and simulated for different absorber gap distances, an approximate relation between the absorber gap and tuning voltage is found.

Fano spectral peaks shift linearly in respect to absorber gap distance change, and the peak wavelength scans over 1550 nm which is the pump laser wavelength. For instance,

at 5.5 V, the laser of 1550 nm is red-detuned from the Fano resonance and the device exhibits optomechanical cooling effect. At 3.2 V, the laser of 1550 nm is blue-detuned from the Fano resonance and, in opposite, the device exhibits optomechanical cooling effect.

CHAPTER 6: Phonon Lasing and Optomechanical Cooling in the Device

6.1. Introduction

This optomechanical device simultaneously supporting optical and mechanical resonances coupled through opto-thermo-mechanical interactions, the plasmomechanical force arises from the incident 1550 nm laser being absorbed resonantly by the plasmonic nanostructures on the bilayer membrane oscillator. According to the previous analysis, the plasmomechanical force exerted on the membrane is an elastic force in regard to a very small displacement from the balance position. Due to the finite thermal response time constant of the membrane oscillator, the plasmomechanical force is delayed and exhibits a velocity dependent contribution to the equation of motion, yielding modifications on the damping rate of the mechanical oscillator. Depending on the direction of the plasmomechanical force, which is controlled by the detuning direction, the damping rate is either decreased or increased. In a fixed detuning condition, the damping rate modification depends on several factors, of which the power of pumping laser and the coupling optomechanical coupling coefficient are most interesting.

By studying the mechanical oscillation characters, e.g. the damping rate and amplitude, at different detuning conditions and incident laser powers, the influence on the mechanics by optics is observed and analyzed. Figure 6-27 exemplifies the mechanical spectra at different detuning conditions. As the tuning voltage increases and the absorber gap decreases, the device is adjusted from blue-detuning to red-detuning and exhibits optomechanical amplification and cooling respectively. Comparing the mechanical spectra, the amplified mechanical mode has a larger mechanical amplitude and narrower peak, while the cooled mechanical mode has a smaller amplitude and wider peak.

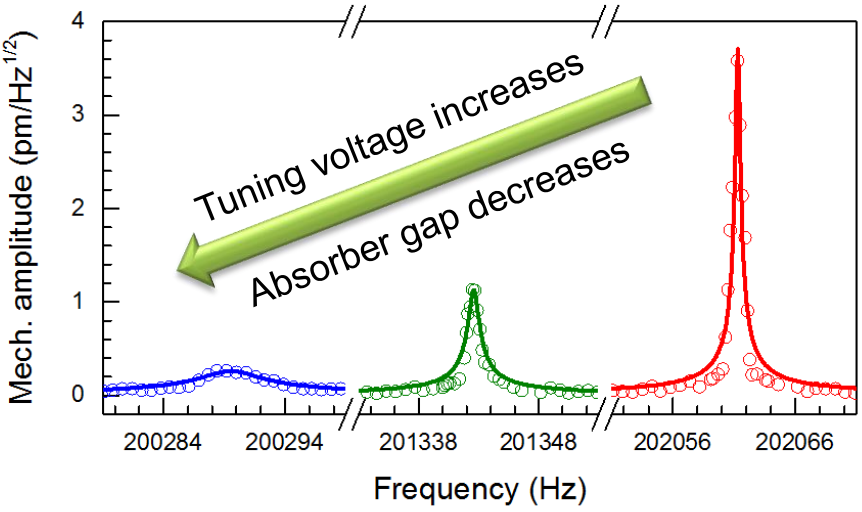

Figure 6-27. Mechanical spectra of optomechanical amplification (red), weak interaction (green), and cooling (blue) for the deivce under different bias voltages. The incident laser power of 17 μW is used for the measurement.

For optomechanical cooling, the mechanical oscillation is further dampened with increased optical pump power, resulting in a wider and lower mechanical spectral peak. The amplification case is basically opposite. However, when the damping rate decreases to zero, the line-width of the oscillation becomes infinitesimal and the loss-less oscillation can build up a very large amplitude. This optomechanical phenomenon analogous to a laser is called phonon lasing [1-4].

6.2. Two Optomechanical Effects in One Device

By solving the coupled-mode theory equations in Chapter 4, the optomechanical modification on the mechanical damping rate is found proportional to the gradient of the plasmomechanical force: $\Gamma_{pm} = \Gamma_{m,eff} - \Gamma_{m,0} \propto \nabla_z F_{pm}$. The force itself depend on the

temperature rise or the absorption power in the membrane, so $F_{pm} \propto A(\omega_0) \cdot P_{in}$, where $A(\omega_0)$ is the absorbance at 1550 nm wavelength and a function of the Fano resonance frequency ω_0, and P_{in} is the incident laser power. Now the force gradient is expressed as:

$$\nabla_z F_{pm} \propto \frac{dA\ \omega_0}{dz} P_{in} = \frac{dA\ \omega_0}{d\omega_0} \frac{d\omega_0}{dz} P_{in} = \frac{dA\ \omega_0}{d\omega_0} g_{pm} P_{in} \tag{123}$$

Equation (123) implies that the force gradient scales linearly with the differential spectral absorbance $dA/d\omega_0$, the input laser power P_{in}, and $g_{pm} \equiv d\omega_0/dz$, a measure of optical resonance shift for a change in the absorber gap distance. For this device, the measured $g_{pm} \approx$ -340 GHz/nm yields $\nabla_z F_{pm} \approx 66$ pN/nm for $P_{in} = 1$ mW.

The differential spectral absorbance $dA/d\omega_0$ was derived from the simulated absorbance at 1550 nm for a range of frequencies and is plotted in Figure 6-28(A). $dA/d\omega_0$ appears opposite signs and different values, due to the asymmetric lineshape of the Fano resonance, on the blue and red sides of the Fano resonance. For the blue-detuning case, the maximum of $\nabla_x F_{pm}$ is about 3 times larger compared to that for the red-detuning, indicating that optomechanical amplification is more efficient than the cooling in this device.

The square membrane oscillator of 500 μm by 500 has the fundamental resonance frequency $f_{1,1} \approx$ 201 kHz and linewidth $\Gamma_0 \approx 2\pi \times$ 3.4 Hz ($Q_0 \approx$ 60000). Once the 1550 nm laser is incident on the absorber, the opto-thermo-mechanical interactions immediately influence the mechanical linewidth.

The mechanical spectra of the membrane oscillator are measured at $P_{in} = 17.5$ μW for different detuning conditions. At negative (blue) resonance detuning, the measured linewidths are smaller than Γ_0, indicating a negative modification on the damping rate. At positive (red) resonance detuning, the measured linewidths are larger than Γ_0, indicating a positive modification on the damping rate. The measured results are successfully fitted by equation (111), shown in Figure 6-28 (B). The asymmetric lineshape of the Fano resonance is treated as two different optical damping rate on the two sides of the resonance peak.

After fitting the 17.5 μW data, the constants are saved to generate the curve for $P_{in} = 20.3$ μW at the negative detuning and $P_{in} = 70.0$ μW at the positive detuning. These cases are then measured and the data show agreement to the theory curves (Figure 6-28 (B)). This agreed results proves that the optomechanical modification of the damping rate scales with the incident laser power. The data of 20.3 μW near the detuning of −2 THz seems deviating from the theory curve. The measured linewidth data are locked to about 0.58 Hz because of the minimum resolution limit of the spectrum analyzer.

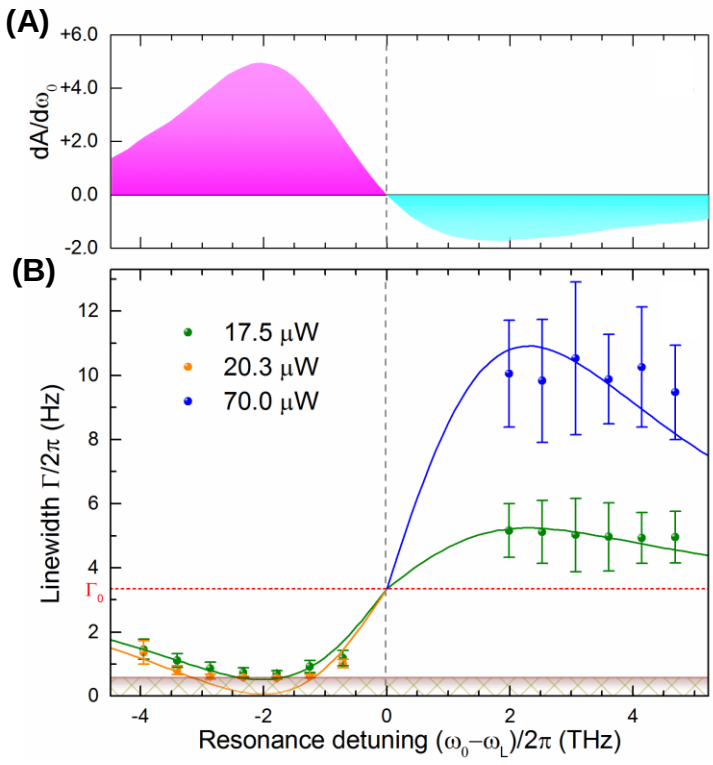

Figure 6-28. Optomechanical amplification and cooling in one device. (A) The differential spectral absorbance vs frequency detuning. (B) The total mechanical damping $\Gamma = \Gamma_0 + \Gamma_{pm}$ vs frequency detuning. The measured data (dots) is in excellent agreement with theory (solid lines). The mechanical linewidth is decreased ($\Gamma_{pm} < 0$) at negative (blue) detuning and increased ($\Gamma_{pm} > 0$) at positive (red) detuning.

6.3. Coherent Mechanical Oscillations: Phonon Lasing

6.3.a. Phonon Laser Theory by Laser-Rate-Equations

When the device is blue-detuned, the optomechanical modification of the mechanical damping rate is negative. As the optomechanical amplification effect is enhanced, e.g. by increased laser pump power, the damping rate may decrease to zero. In that case, the mechanical oscillation gains energy from the light and the power gain is sufficient to overcome the power loss, i.e. the intrinsic mechanical damping. This process

is very much similar to an optical laser. Since the energy being amplified is mechanical oscillation energy, this coherent mechanical oscillator is named “phonon laser”.

Khurgin et al. has proposed the theory framework for phonon lasers [3]. The coherent mechanical oscillation introduced by plasmomechanical coupling can be described in the form of standard laser rate equation set:

$$\frac{dU_{st}}{dt} = \frac{U_{st,0}}{\tau_t'}\left(1-\frac{U_m}{U_{sat}}\right)-\frac{U_{st}}{\tau_t'} \tag{124}$$

$$\frac{dU_m}{dt} = \left(\frac{U_{st}}{\tau_t' U_{sat}}-\gamma\right)U_m + \tfrac{1}{2}\gamma kT \tag{125}$$

where g is the gain (per unit of time), τ_t' is the modified thermal response time, γ is the mechanical damping rate, U_m is the total energy of mechanical vibrations, U_{sat} is the saturation value of U_m, $U_{st} = g\tau_t' U_{sat}$ is the stored energy of the coherent phonons available for lasing, and $U_{st,0}$ is the unsaturated value of U_{st} when $g = g_0$.

In the case of week vibrations (far from reaching saturation), after defining the pumping efficiency $\eta_p = U_{st,0}/P_{in}\tau_t'$, equation (124) can be approximated as:

$$\frac{dU_{st}}{dt} = \eta_p P_{in} - \frac{U_{st}}{\tau_t'} - \frac{U_{st}}{\tau_t'}\frac{U_m}{U_{sat}} \tag{126}$$

By defining the relative energies and power $u_{st} = U_{st}/U_{st,th}$, $u_m = U_m/U_{sat}$, and $p_{in} = P_{in}/P_{th}$, where $P_{th} = U_{st,th}/\eta_p\tau_t'$ is the threshold pump power, we have the laser equations in dimensionless forms:

$$\frac{du_{st}}{dt} = \frac{1}{\tau_t}\left[\, p_{in}\left(1-u_m\right)-u_{st}\,\right] \tag{127}$$

$$\frac{du_m}{dt} = \gamma\left(u_{st} - 1\right)u_m + \gamma\frac{kT}{2U_{sat}} \tag{128}$$

When $P_{in} > P_{th}$, u_{st} is fixed at 1, and the steady-state solution for the mechanical oscillation energy is:

$$u_m = \left(p_{in} - 1\right)/p_{in} \tag{129}$$

Therefore we get the equation for output mechanical power:

$$P_{out} = \gamma U_m = \eta_p \frac{P_{th}\left(P_{in} - P_{th}\right)}{P_{in}} \tag{130}$$

6.3.b. Phonon Lasing in the Device

The differential spectral absorbance curve in Figure 6-28(A) suggests that the optomechanical amplification is most efficient near the detuning of −2 THz, which is achieved by applying a bias voltage of about 3 V. The mechanical spectra of the device tuned at 3.2 V are measured under increased incident power, and their linewidth and amplitude are shown in Figure 6-29 (A) and (B). As the optical pump power increases, the mechanical linewidth decreases linearly, because the (negative) optomechanical modification on the damping rate is proportional to the incident laser power (equation (123)). Above a threshold power of about 19 μW, the mechanical linewidth saturates at 0.58 Hz, which is the resolution limit of the spectrum analyzer. At the same threshold, the mechanical amplitude increases drastically for about 3 orders of magnitude. The threshold power implies a condition when the intrinsic damping and optomechanical gain in the mechanical oscillator reaches equilibrium.

Mechanical output power, which is basically the mechanical dissipated power defined as $P_{out} = E_m \times \Gamma_{m,0}$, where E_m is the energy of the mechanical mode and $1/\Gamma_{m,0}$ characterizes the average time for the mechanical oscillator to lose its mechanical energy. For the same mechanical oscillator, the intrinsic damping rate $\Gamma_{m,0}$ is basically constant. Therefore P_{out} scales with the energy of the mechanical mode, which scales with the area under the peak of the squared amplitude spectrum. In order to estimate the absolute power value, the energy of the mechanical oscillator under the lowest optical pump power is approximated as an unperturbed mechanical oscillator, whose energy is $\frac{1}{2}k_B T_{room}$. By this calibration methods, the mechanical output powers with increase optical pump power is plotted in Figure 6-29(C), which are close to zero below the threshold. The mechanical output power increases rapidly above the threshold. The measured data are successfully fitted by equation (130), giving the value of the threshold power as 18.7 μW. The measured saturation power is lower than the theory, due to higher order effects neglected in the theory.

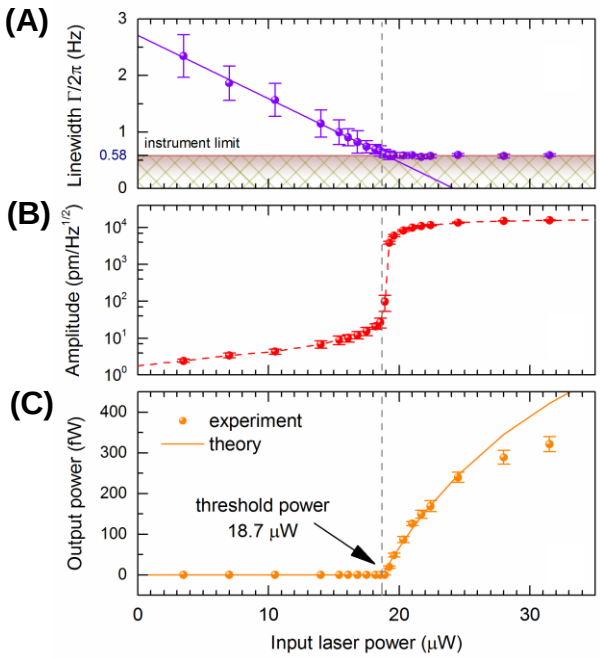

Figure 6-29. Phonon lasing in the device tuned at 3.2 V. (A) The mechanical linewidth decreases linearly until it reaches below the instrument limit of 0.58 Hz at the threshold pump power of about 19 μW (B) The mechanical peak amplitude increases with the optical pump power. Above the same threshold pump power, the mechanical amplitude increases drastically until it saturates. (C) The mechanical output power, generally proportional to the square of the amplitude, increases with the optical pump power. The measurements (dots) are fitted by equation (130), yielding the theory curve and giving the power threshold value of 18.7 μW.

6.3.c. Broadband Capability

The nature of the broadband Fano resonances allows phonon lasing over an extremely broad range of optical pump frequencies, i.e. over 3 THz. Figure 6-30 shows the phonon lasing measurements over various blue-detuning conditions. The device receives different optomechanical gains from the collective contributions by the differential spectral absorbance and the laser pump power. In the detuning condition where $\frac{dA}{d\omega_0}$ is small, a large power threshold is expected to intrigue phonon lasing. In the detuning condition

where $\frac{dA}{d\omega_0}$ is large, a small power threshold is sufficient to start phonon lasing. Figure 6-30(A) compares the phonon lasing thresholds and $\frac{dA}{d\omega_0}$ for various detuning conditions. In addition to the device at 3.2 V, three more detuning conditions were measured. The results demonstrate phonon lasing at different thresholds (Figure 6-30 (B)).

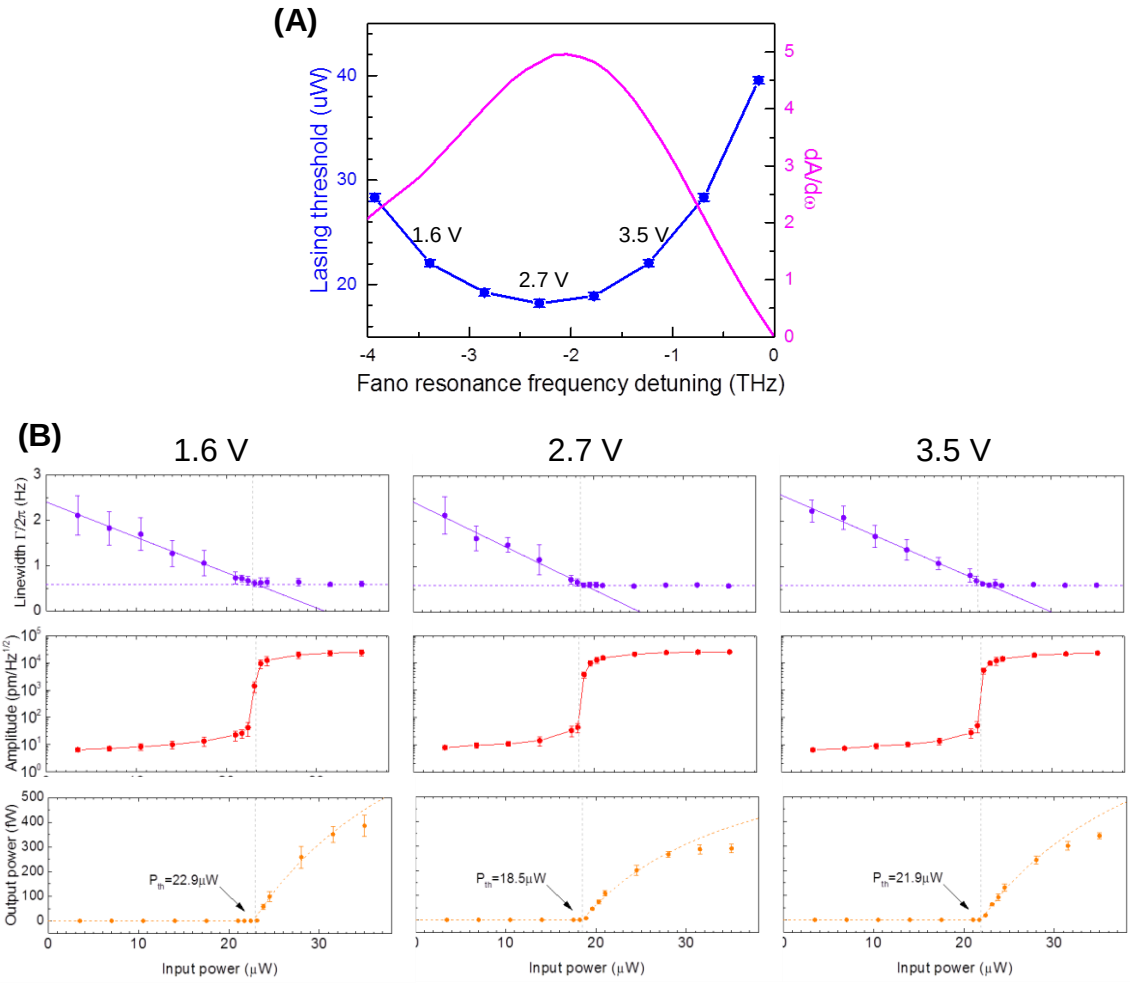

Figure 6-30. Phonon lasing in different detuning conditions. (A) The threshold pump power for phonon lasing in the device (blue disks) follows the inverse trend of the differential spectral absorbance (magenta curve). (B) The phonon lasing results measured at the tuning voltage of 1.6 V, 2.7 V, and 3.5 V. The linewidth, mechanical amplitude, and mechanical output power all exhibit

a transition at the threshold power. The output power data are fitted by equation (130), giving the threshold power for each condition.

6.4. Optomechanical Cooling

The displacement power spectral density $\left\langle x^2(f)\right\rangle$ is fitted by the "Lorentzian" lineshape:

$$\left\langle x^2(f)\right\rangle = A_0 + \frac{2A}{\pi}\cdot\frac{wf_0^2}{\left(f_0^2 - f^2\right)^2 + w^2 f^2} \tag{131}$$

where f_0 is the resonant frequency, w is the full width at half maximum (the damping rate is $\Gamma = 2\pi w$), A is the area under the spectral density for the resonance peak, and A_0 is the background white noise level. The peak mechanical amplitude is $x_{peak} = \sqrt{2A/\pi w}$. For unperturbed mechanical oscillator, we have $\frac{1}{2}k_B T_{eff} = \frac{1}{2}K_m x_{rms}^2$. We can determine the spring constant K_m from the measured resonance frequency and the calculated effective mass of the fundamental mode. We can then estimate $x_{rms} = \sqrt{\left\langle x^2\right\rangle}$ for $K_m = 0.205$ N/m and $T_{eff} = 300$ K, which yields $x_{rms} = 142$ pm. The mechanical peak amplitude is related to the mechanical root mean square (rms) amplitude by:

$$x_{peak} = \sqrt{\frac{1}{\pi w}}x_{rms} \tag{132}$$

We can then calculate the effective temperature, which is proportional to the area under the power spectral density curve:

$$E \propto T_{eff} \propto K_{m,eff}x_{rms}^2 \propto \frac{K_{m,eff}}{w}x_{peak}^2 \propto A \tag{133}$$

For optomechanical cooling, the damping rate of the mechanical oscillator increases as the input laser power increases. Suffered by a stronger damping, the mechanical mode losses its energy, i.e. reduces its effective temperature. *w* is used to represent the linewidth, which is in essence the damping rate, and A is used to track the change of the oscillator's effective temperature or energy.

Figure 6-28(A) tells that the optomechanical cooling effect is most efficient at between 5 V and 5.5 V. Figure 6-31 shows the results for the optomechanical cooling in the device tuned at 5.5 V. The effective temperature of the mechanical mode decreases with increased laser pump power. For the laser power of 210 μW, the effective temperature is reduced to below 50 K, assuming the environment temperature is 300 K. The linewidth of the mechanical mode, i.e. the damping rate, increases linearly to the increase optical pump power. Although the opto-thermo-mechanical interaction mechanism involves heating of the membrane oscillator, its Brownian vibrational mode is still suppressed by the reactive plasmomechanical force. However, further optomechanical cooling is ultimately limited by the heating effect, for Brownian motion becomes strenuous.

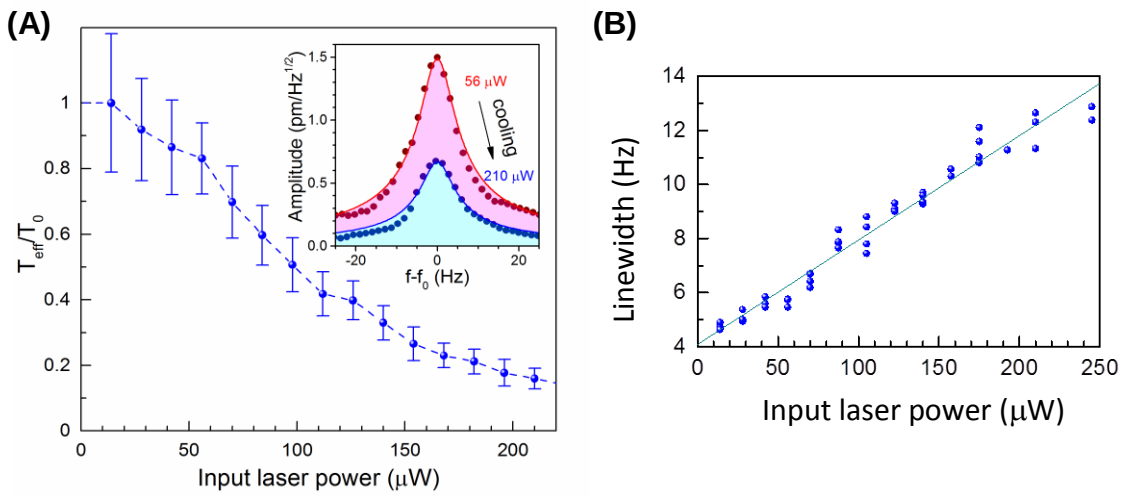

Figure 6-31. Optomechanical cooling in the device tuned at 5.5 V. (A) The effective temperature of the mechanical mode, a character of energy, is reduced to below 50K by 210 μm laser pump power in the environment of 300 K. Inset: the mechanical resonance spectra and their Lorentzian fits for 56 μW and 210 μW laser pump powers exemplify the reduction in mechanical energy, i.e. cooling, which is related to the area under the mechanical resonance peak.

6.5. Conclusions

This integrated optomechanical device based on plasmonic metamaterial absorber supports both optomechanical amplification and cooling operations depending on the detuning conditions. For both effects, the measured mechanical linewidth data are inconsistent with the coupled-mode theory model, proving that the optomechanical modification on the damping rate scales with and laser pump power and differential spectral absorbance.

The extreme case of optomechanical amplification, i.e. phonon lasing, is studied. The mechanical linewidth, amplitude, and output power all exhibit a threshold as they vary with the increased optical pump power, manifesting the relations very similar in lasers. Compared to high Q factor (~ GHz linewidth) dielectric systems, this substantially relaxes

the stringent frequency locking requirements and allows broadband (~ 3 THz linewidth) light sources as the optical pump. This device may offer a unique possibility for free space phonon manipulation with incoherent light sources. The plasmonic metamaterial approach can extend these effects across the electromagnetic spectrum by design. This device will pave the way to new physics based on plasmonic metamaterial backaction effects and will lead to applications in novel inertial sensors and coherent acoustic phonon source for ultrasonic imaging modalities.

6.6. References

1. Vahala, K., et al., *A phonon laser.* Nature Physics, 2009. **5**(9): p. 682-686.
2. Grudinin, I.S., et al., *Phonon Laser Action in a Tunable Two-Level System.* Physical Review Letters, 2010. **104**(8).
3. Khurgin, J.B., et al., *Laser-Rate-Equation Description of Optomechanical Oscillators.* Physical Review Letters, 2012. **108**(22).
4. Mahboob, I., et al., *Phonon Lasing in an Electromechanical Resonator*. Physical Review Letters, 2013. **110**(12).

PART B: NOVEL PLASMONIC AND NANOPHOTONIC DEVICES FOR SENSING APPLICATIONS

CHAPTER 7: An Infrared Detector Based on Thermomechanical Plasmonic Membranes

This chapter is majorly adopted from:

"Plasmonically Enhanced Thermomechanical Detection of Infrared Radiation", Fei Yi, Hai Zhu, Jason C. Reed, Ertugrul Cubukcu, Nano Letters, 13 (4), (2013)

"Thermoplasmonic Membrane-Based Infrared Detector", Fei Yi, Hai Zhu, Jason C. Reed, Alexander Y. Zhu, Ertugrul Cubukcu, IEEE Photonics Technology Letters, vol. 26, issue 2, (2014)

7.1. Introduction

The nanoscale light concentration and near-field enhancement available to resonant metallic nanostructures have been a driving force in nanoplasmonics [1, 2]. Along these lines, plasmonic nanoantennas have been utilized in a broad range of applications involving strong light-matter interactions [3-12]. Recently, thermoplasmonics, which take advantage of photothermal effects induced by resonant light absorption in metallic nanostructures [13-17], has emerged as a new research direction enabling nanoscale heat sources. These effects have been investigated for different applications, such as photothermal cancer therapy [18-20] and thermophotovoltaics [21, 22]. On a different front, nanomechanics is a vibrant research field in nanoscience that has generated both academic and industrial interest for its promise in novel sensor applications [23-29]. Inspired by the Golay cell, an optomechanical thermal detector [30], thermally actuated bilayer cantilever based micromechanical structures have been invented and used as optomechanical focal plane arrays for detection of infrared [31-34] and terahertz [35] radiation.

We proposed a new plasmo-thermomechanical device platform, which integrates thermoplasmonic effects with nanomechanics using light absorption by plasmonic

nanoantennas as the nanoscale heat source inducing thermomechanical actuation. As one specific example of the platform, we report a novel room temperature thermal infrared detector that integrates a nanoplasmonic absorber on a beam type nanomechanical structure. Our nanoplasmonic thermomechanical device relies on efficient absorption of infrared radiation by an array of nanoslot antennas as an active component that converts optical power into heat. The nanoslot configuration provides the best thermomechanical coupling due to its uniform bilayer material coverage as compared to an array of discrete nanoantenna elements. The generated heat is then converted to a temperature increase on the integrated nanomechanical bimaterial structure. In response to this temperature increase, the bimaterial nanomechanical beam bends as a result of the differences in the thermal expansion coefficients of the two constituent materials. An integrated fiber-based interferometric readout, which offers the best displacement sensitivity, then converts this mechanical bending into an electrical signal [36].

7.2. Device Design and Simulations

7.2.a. Optical Absorber Design

Figure 7-32 illustrates the active structure of the plasmo-thermomechanical IR detector (PlasMIRD) is a suspended 100μm by 500μm bilayer membrane as a nanobeam integrated with a plasmonic metamaterial absorber. The bilayer membrane consists of a 22 nm of gold layer with 3 nm of titanium adhesion layer on a 100nm of silicon nitride membrane. The plasmonic absorber, embedded in the metal layer, consists of an array of nanoslot antennas etched into the bilayer mechanical beam, which is designed to enhance the absorption of the IR radiation with a spectrum centered around a wavelength λ = 6μm

[37]. Typical nanoslots are 100 nm wide and 1600 nm long. We refer to the absorption efficiency of the bilayer structure with integrated nanoantenna absorber as η_{ant} and the absorbed IR power as $P_{abs} \equiv P_{IR} \times \eta_{ant}$, where P_{IR} is the total incident IR power. In previous studies, it has been reported that a single layer of an array of plasmonic nanoantennas can be used as an efficient infrared absorber without a back reflector metal plate used in perfect metamaterial based absorbers [38-40]. The plasmonic nanoslot antenna absorber used in this study converts the freely propagating IR radiation into a localized current that is dissipated into heat due to the finite conductance of gold at these frequencies, similar to Ohmic dissipation in a resistive electrical circuit. The mechanical deflection of the bilayer nanobeam driven by the thermal energy is then read out optically, as diagramed in Figure 7-32(A).

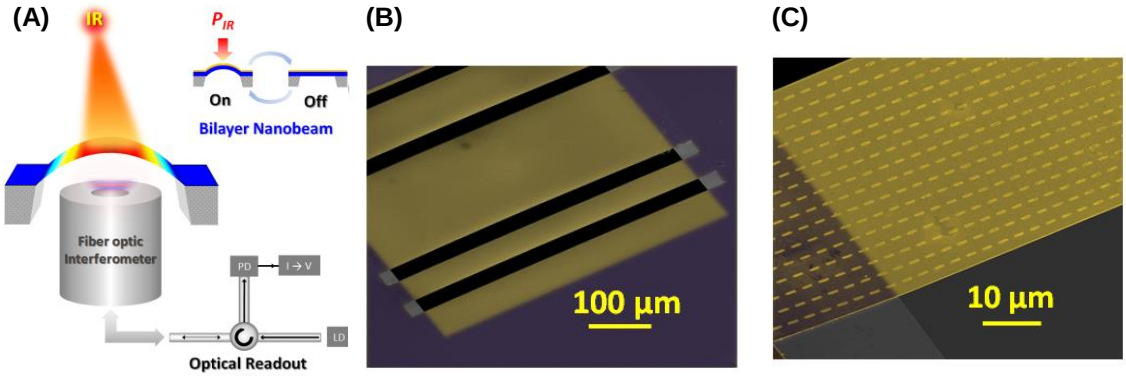

Figure 7-32. An overview of the plasmo-thermomechanical IR detector (PlasMIRD). (A) A nanoslot antenna array is embedded in the gold layer of a bi-metalic beam structure. The IR radiation is converted into heat by the nanoantenna array and causes temperature increase in the bilayer structure. The increased temperature causes the bilayer structure to deflect due to the mismatch between the thermal expansion coefficients of the gold and silicon nitride layers. The bilayer beam is one of the two reflectors of a fiber optic Fabry-Perot interferometer (FFPI). The deflection of the bilayer beam is read out optically by the FFPI. (B) and (C) are the false color SEM images of the nanobeam and plasmonic nanoantennas.

In order to optimize the photothermal conversion efficiency of the plasmonic antenna absorber, we first used a finite element based simulation software COMSOL to numerically study the optical properties of nanoslot antenna absorber employing periodic boundary conditions and plane wave excitation. Figure 7-33(A) shows the simulated unit cell that consists of a nanoslot antenna in a 25-nm-thick metal layer on top of a 100-nm-thick silicon nitride membrane. The nanoslot antennas were excited by a plane electromagnetic wave polarized along the short axis of the antenna, as opposed to the case of a nanorod antenna that requires the electric field to be polarized along its length for resonance excitation [37]. The power transmission (T) and reflection (R) coefficients are first calculated to determine the absorption efficiency defined as $\eta_{ant} = 1\text{-}T\text{-}R$, which was confirmed to be valid through near-field power dissipation calculations for the structure. Figure 7-33(B) shows the induced near field distribution in the slot region, clearly showing that the electromagnetic energy is strongly localized in the slot region. We followed the same procedure as in our previous study [37] to optimize the dimensions of the nanoslot antennas.

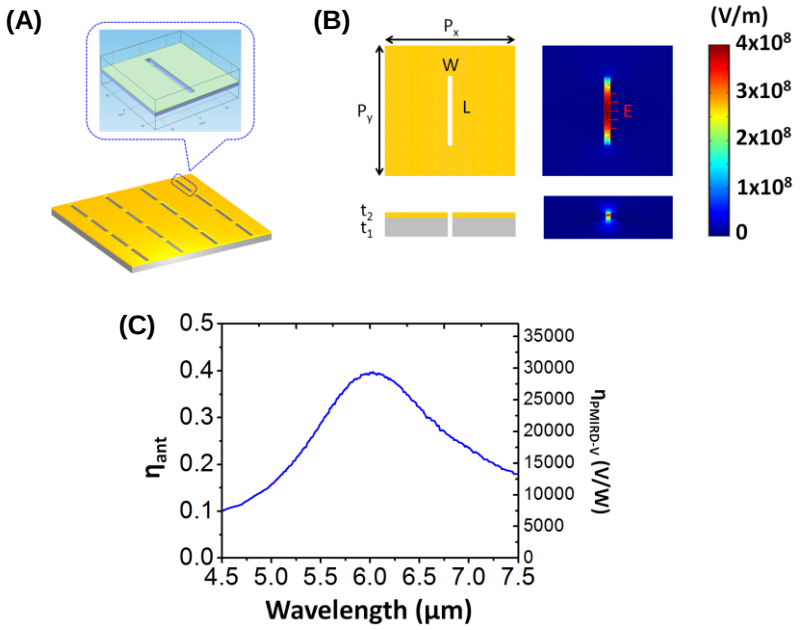

Figure 7-33. The simulation and measurement of the resonant nanoslot plasmonic antennas (A) A unit cell of the studied nanoslot antennas etched into the gold layer with periodic boundary conditions. The thicknesses of the silicon nitride and metal layers are t_1 = 100nm and t_2 = 25nm, respectively (Ti / Au = 3nm / 22nm). b, The schematic diagram of the unit cell and the near field distribution in the slot. c, The typical measured absorption spectrum and the corresponding detector responsivity of the nanoslot antennas with p_x = p_y= 3μm, W = 100nm and L = 1.6μm.

The nanoslot antennas were optimized by these numerical calculations and fabricated by etching all the way through into the free standing bilayer mechanical beam. A thickness ratio between the gold and nitride of 1:4 was previously reported to be the optimized value for maximum mechanical deflection [32, 33]. Figure 7-33(C) shows the typical measured absorption spectrum of the nanoslot antenna array. The measured peak absorption of 40% occurs at a resonant wavelength of 6μm in agreement with absorption for a single layer of resonant nanostructured metal sheet on a substrate without a metal back reflector [41]. Since the metal thickness is constrained by the thickness ratio of gold and silicon nitride for maximum mechanical deflection, the nanoslot design offers about

10 times larger absorption compared to that of a uniform metal layer of the same thickness. The gold nanoantennas resonantly capture the incident energy and effectively dissipate it into heat [42]. Unity optical absorption can be achieved using a metal back reflector on the other side of the silicon nitride layer to enhance the plasmonic resonance. However, adding the back reflector on the other side of the bilayer structure would reduce its mechanical deflection.

7.2.b. Thermal and Mechanical Analysis

The second stage of the plasmo-thermomechanical IR detection is the thermomechanical actuation of the bilayer nanobeam. The absorbed IR power causes an increased temperature ΔT in the bilayer nanobeam. The rate of temperature increase in a bilayer nanobeam of length l and width w per unit absorbed IR power, defined as $\eta_{T/P} \equiv \Delta T / P_{abs}$, is found by solving the 1D heat transfer equation: [43-45]

$$\frac{d^2}{dx^2}T(x,t)+\frac{1}{\kappa}g(x,t)=\frac{1}{\alpha}\frac{d}{dt}T(x,t) \tag{134}$$

In our thermal analysis, we assumed that the midpoint located at $x=0$ is initially held at a constant temperature $T(x, t = 0) = T_0 = 300$ K, same as the two ends of the beam modeled to be perfect heat sinks. Here, $\kappa = (\kappa_1 t_1 + \kappa_2 t_2)/(t_1+t_2)$ is the thermal conductivity and $\alpha = (\kappa_1 t_1 + \kappa_2 t_2)/(\rho_1 C_1 t_1 + \rho_2 C_2 t_2)$ is the thermal diffusivity of the composite beam averaged over the thickness, where ρ, C, and t are, respectively, the mass density, the specific heat, and the layer thickness. The subscripts 1 and 2 refer to the gold and nitride layers, respectively. The heat generation density $g(x,t)$ is proportional to the absorbed infrared power P_{abs} and can have different spatial profiles depending on the illumination

source; i.e. point source at the center of the beam, uniform source along the beam, or Gaussian beam source. The steady state solution of equation (134) for the uniform heating case (shown in Figure 7-34(A)) is given by:

$$T(x) = \frac{[(l/2)^2 - (x/2)^2]P_{abs}}{2(\kappa_1 n + \kappa_2)t_2 wl} + T_0 \tag{135}$$

for $-\frac{l}{2} \le x \le \frac{l}{2}$.

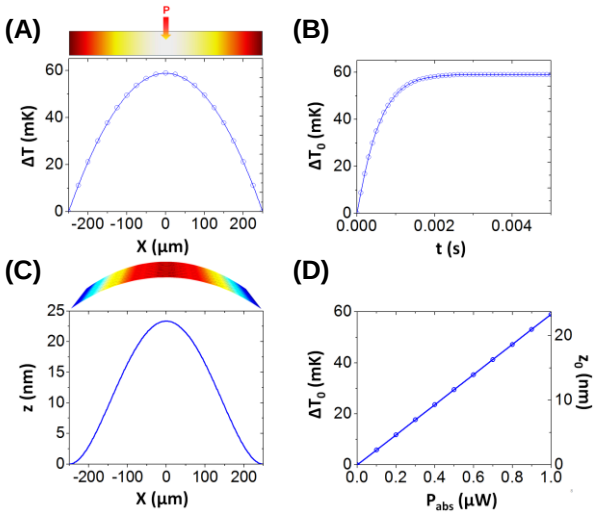

Figure 7-34. The FEA simulation results for the heat transfer and mechanical deflection (A) The steady state temperature difference distribution ΔT along a bilayer beam under uniform infrared illumination and the corresponding line-scan at the center point. The total absorbed power P_{abs} = 1μW. (B) The temporal evolution of temperature increases ΔT_0 at the center of the beam. (C) The 2D distribution of steady state deflection z in a bilayer beam caused by the temperature increase. The bilayer beam is fixed at the two edges. (D) The steady state temperature increase ΔT_0 and the resulted mechanical deflection z_0 as a function of the absorbed power P_{abs}.

The Green's function method solutions for point source and Gaussian beam source heating are given in the Supporting Information. We also used a finite element method code to solve the heat transfer problem in the bilayer structure and found perfect agreement

with the analytical solution. Figure 7-34(B) shows the exponential increase of the temperature difference $\Delta T_0(t)$ at the center of the beam. The *1/e* time constant τ was found to be about 0.55 ms for all the three heating profiles. From the linear relationship between ΔT_0 and P_{abs}, as shown in Figure 7-34(D), we found $\eta_{T/P}$ to be 1.18×10^5 K/W for point source heating, 9.13×10^4 K/W for Gaussian source heating and 5.9×10^4 K/W for uniform heating. The induced temperature difference ΔT in turn causes the bilayer structure to expand and deflect due to the mismatch between the thermal expansion coefficients γ of silicon nitride and gold. The temperature induced bending of the bilayer beam can be calculated analytically using the following differential equation: [46]

$$\frac{d^2z}{dx^2} = 6\times(\gamma_2-\gamma_1)\frac{t_1+t_2}{t_2^2K}\Delta T(x) \tag{136}$$

Here, the dimensionless parameter $K = \frac{E_2}{E_1}n^{-1} + 4 + 6n + 4n^2 + \frac{E_1}{E_2}n^3$ is defined in terms of the Young's moduli of the two materials $E_{1,2}$ and the thickness ratio $n = t_1/t_2$. Figure 7-34(C) shows the rigorous 3D numerical simulation results of the mechanical deflection along the bilayer structure for uniform source. The thermomechanical conversion factor $\eta_{z/P}\equiv z/P_{abs}$ is found to be 0.047 m/W, 0.036 m/W, and 0.023 m/W for the point source, Gaussian beam, and uniform heating, respectively.

7.3. Nanobeam Deflection Detection

7.3.a. Deflection Measured by Fiber-optic Interferometer

In order to measure the bilayer nanobeam deflection, *z,* we use a fiber optic interferometer that offers the best displacement sensitivity [36] based on a FP cavity formed between the facet of a cleaved fiber and the nanobeam. Output of a very low noise external cavity diode laser of 1550 nm wavelength is coupled into the cleaved probe fiber through a fiber-optic circulator whose return port is connected to a shot-noise limited small area PIN photodiode. The light reflected by the cleaved end facet of the fiber and the nanobeam will interfere with each other. Therefore, the total reflected optical power, P_{FPr}, is very sensitive to the change *z* in the distance between the bilayer mechanical beam and the facet of the fiber, *i.e. the cavity length,* allowing us to measure the nanobeam deflection *z*. The power sensitivity of the interferometer, η_{FP}, is the change in reflected power per unit deflection, i.e. $\eta_{FP} = dP_{FPr}/dz$, which reaches its maximum value for cavity lengths equal to an integer multiple of a quarter wavelength. The changes in the mechanical bending of the bilayer structure yields changes in the photocurrent given by $\Delta I_{PD} \equiv \eta_{PD} \times \eta_{FP} \times z$, where η_{PD} is the quantum efficiency of the photodiode. For an interferometer input of 1mW, η_{PD} = 0.886 A/W, and R = 0.037 (the power reflection coefficient for the end facet of a bare fiber). The maximum power sensitivity at the quadrature point of interferometer is therefore η_{FP} = 0.318 μW/nm and the current sensitivity $\eta_{FP\text{-}I} = \eta_{PD} \times \eta_{FP}$ = 0.282 μA/nm, which agrees well with the measurements. In the last stage of the plasmo-thermomechanical detector, the signal current I_{PD} is converted by a current to voltage converter with a resistance R_{IV} into an output voltage $V_{OUT} = I_{PD} \times R_{IV}$. The signal voltage V_{OUT} is therefore related to the input IR power P_{IR} by:

$$V_{OUT} = P_{IR} \times \eta_{ant} \times \eta_{T/P} \times \eta_{z/T} \times \eta_{FP} \times \eta_{PD} \times R_{IV} \equiv P_{IR} \times \eta_{PlasMIRD} \quad (137)$$

where $\eta_{PlasMIRD}$ is defined as the voltage responsivity of the PlasMIRD.

One of the important characteristics for a detector is its responsivity, the measure of how efficiently the detector can convert optical power to electrical power. We experimentally characterized the responsivity of the fabricated devices using two different lasers. A 405 nm diode laser that can be sinusoidally modulated is used as the heat source for the measurement of the temporal characteristics of the photothermal response. The typical normalized frequency response of the PlasMIRD is shown in Figure 7-35(B). The 3 dB cutoff frequency, f_{3dB}, is found to be 23 Hz corresponding to a time constant $\tau = 1 / (2\pi f_{3dB}) = 6.9$ ms.

For the infrared photoresponse of PlasMIRD, we use the output of a continuous wave quantum cascade laser (QCL) of ~6μm wavelength modulated by a mechanical chopper. The chopper frequency is set at 1000 Hz. In order to study the dependence of the PlasMIRD response on the input IR power, we reduced the P_{IR} from 0.45 mW and monitored I_{PD}. Figure 7-35(C) shows that there is a linear relationship between the normalized response of PlasMIRD and the input IR power in agreement with the theoretical prediction. By using the measured frequency dependence of the photothermal response in Figure 7-35(B), we can estimate the voltage responsivity as 29kV/W for $R_{IV} = 10^5$ V/A in the low frequency limit.

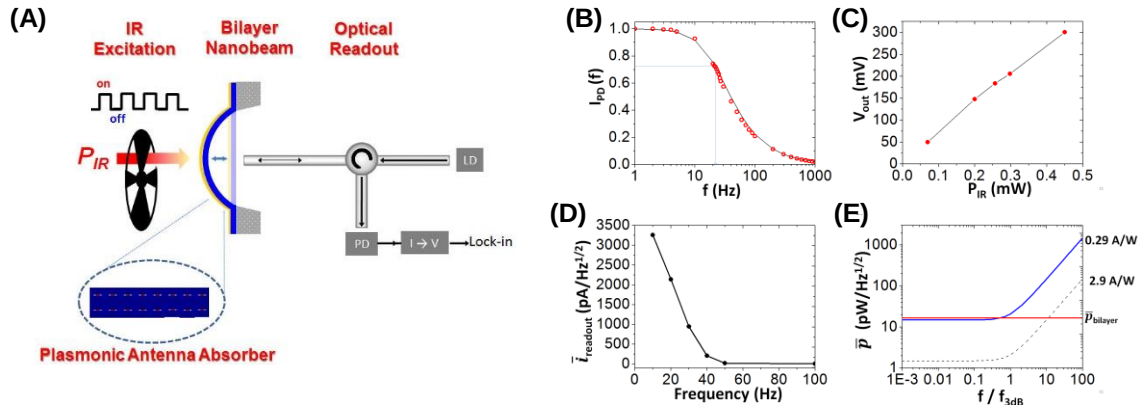

Figure 7-35. Characterization of the IR detector. (A) The schematic of the measurement system. (B) The normalized frequency response of the PlasMIRD measured using a modulated 405nm laser as the excitation. (C) The relationship between the response of the PlasMIRD at 1000 Hz and the input IR power. The vertical axis is the output voltage of the current to voltage converter, measured by the lock-in amplifier. The horizontal axis is the IR power received by the nanobeam. (C) 1/f spectral density noise of the readout system. (D) The total bilayer noise density $\bar{p}_{bilayer}$, including thermal fluctuation noise, background fluctuation noise, and thermomechanical vibration noise (the red solid line), and the optical readout noise equivalent power $\bar{p}_{readout}$. (the blue solid line for $\eta_{PlasMIRD}$ =0.29 A/W and the black dash line for $\eta_{PlasMIRD}$ =2.9 A/W).

Since in many applications the primary objective is measuring small signals, the most important performance parameter for a detector is, arguably, its noise equivalent power (NEP), which is a direct measure of the smallest optical power that can be measured. The NEP of a detector is limited by the fluctuations in the output voltage, without any input infrared power, originating from non-equilibrium thermodynamical processes and quantum statistics of photons and electrons in the detection system. In our detector there are two main parts of the detection system, namely, the interferometric read out system and the bilayer nanobeam, that contribute to the detector noise. For the bilayer nanobeam, the fundamental sources of noise are (1) the thermal fluctuation noise, similar to Johnson noise in a resistor due to the finite thermal conductance of the bilayer structure, (2) background

fluctuation noise due to the radiative heat exchange with the environment, and (3) thermomechanical noise originating from the thermal energy of the mechanical modes [47]. The thermal fluctuation noise $\overline{p}_{th}$ due to the heat exchange between the bilayer beam and the supporting silicon frame through the two "legs" of the bilayer beam amounts to 6.5 pW/Hz$^{-1/2}$. The background fluctuation noise $\overline{p}_{RAD}$ which accounts for the random fluctuations in temperature due to the heat exchange between the bilayer beam and the environment through radiation is found to be 1.2 pW/Hz$^{-1/2}$. The off-resonance thermomechanical [48, 49] vibration noise $\overline{p}_{vib}$ arising from the thermal energy of the bilayer beam can be calculated as 17 fW/Hz$^{1/2}$ using the measured mechanical to optical conversion efficiency along with the mechanical resonance frequency (146.6 kHz) and the quality factor (Q~980). We can define the total noise from the bilayer structure as

$$\overline{p}_{bilayer} = \frac{1}{\eta_{ant}} \sqrt{\overline{p}_{th}^2 + \overline{p}_{RAD}^2 + \overline{p}_{vib}^2} \tag{138}$$

By plugging in the values calculated above and the measured η_{ant}, $\overline{p}_{bilayer}$ is calculated to be 16.5 pW/Hz$^{1/2}$ in the low frequency limit. It is clear that the main contribution to $\overline{p}_{bilayer}$ is from the thermal fluctuation noise $\overline{p}_{th}$.

7.3.b. Noise Measurement and Limit Analysis

The interferometric read-out setup is limited by two fundamental noise sources: 1) the shot noise of the PIN photodetector and 2) the relative intensity noise (RIN) of the 1550 nm laser originating from spontaneous emission. We find the total read-out current noise, dominated by the photodetector shot noise, to be $\overline{i}_{readout}$ = 4.3 pA/Hz$^{1/2}$. In the low

frequency limit, this corresponds to an NEP, $\overline{p}_{readout}$ = 14.8 pW/Hz$^{1/2}$. For higher frequencies the thermal responsivity needs to be taken into account.

We also need to consider the 1/*f* noise for the low frequency region. As seen in the measured noise spectrum (Figure 7-35(D)), our optical readout system is dominated by the 1/*f* noise when the operation frequency is below 50 Hz. Above 50 Hz, shot noise and RIN noise are the major contributions. Therefore the requirement imposed by 1/*f* noise is that the operation frequency of the PlasMIRD should be above 50 Hz.

Figure 7-35(E) shows the frequency dependence of $\overline{p}_{readout}$ and $\overline{p}_{bilayer}$. Since $\overline{p}_{readout}$ also depends on the responsivity of the PlasMIRD due to the frequency dependence of the thermal responsivity. It can be seen that for the measured responsivity of 0.29 A/W, the dominant noise originates from the bilayer nanobeam in the low frequency limit ($f < f_{3dB}/2$) and from the read-out setup for $f > f_{3dB}/2$. Since the operation frequency needs to be above 50 Hz due to the 1/*f* noise and the measured f_{3dB} = 23Hz, the PlasMIRD is limited by the readout noise when $\eta_{PlasMIRD}$= 0.29 A/W. At 50 Hz we have $\overline{p}_{total} = (\overline{p}_{bilayer}^{2} + \overline{p}_{readout}^{2})^{1/2}$ = 39pW/Hz$^{1/2}$ dominated by $\overline{p}_{readout}$ = 35 pW/Hz$^{1/2}$. If the responsivity is increased by 10 times by optimizing the sensitivity of the interferometer, $\overline{p}_{readout}$is reduced to 1.48 pW/Hz$^{1/2}$ and $\overline{p}_{total}$is limited by $\overline{p}_{bilayer}$ = 16.5 pW/Hz$^{1/2}$ when $f < 11 \times f_{3dB}$ = 253Hz. Therefore when $\eta_{PlasMIRD}$ = 2.9A/W, the PlasMIRD is thermal fluctuation noise limited if the operation frequency is between 50Hz and 253Hz, and the thermal fluctuation noise equivalent power $\overline{p}_{bilayer}$ = 16.5 pW/Hz$^{1/2}$.

In order to reach the thermal fluctuation noise limit, there are several ways to increase the responsivity; 1) Coating the fiber with metal layer to increase the reflectivity

R of the end surface of the fiber. As discussed in the Supporting Information about the fiber-optic FP interferometer (FFPI), if R of the two reflectors in the interferometer is increased from 0.037 to 0.6, the sensitivity of the interferometer η_{FP} will increase by 18 times. 2) Increase the power of the detecting light P_{1550}, because the sensitivity of the interferometer also increases linearly with the power of the detecting light. 3) Optimizing the bilayer structure to achieve larger deflection.

In the current version of the PlasMIRD, we measured the NEP to be 5nW/Hz$^{1/2}$ at 1 kHz, which is already comparable to that of commercially available thermal infrared detectors. We believe that the NEP of this initial device is limited by the microphonic pickup of ambient noise by the cleaved fiber of ~1 cm length used in the interferometer setup. In a commercial implementation of our detector, the silicon bench technology [50] can be used to reduce the length of the fiber extension length to ~100 μm, substantially eliminating the microphonic noise.

There are several approaches that can be taken to optimize the responsivity and the speed of our detector. For example, to improve the responsivity employing a distributed nanorod antenna absorber with back reflector can achieve unity IR absorption without reducing the mechanical deflection. The nanobeam can be modified to nanocantilever to obtain larger deflection. As discussed before, the sensitivity of the fiber optic interferometric readout can also be improved. The time constant, τ, like other thermal IR detectors, is on the order of miliseconds, but it can be optimized by shortening the length L of the nanobeam or cantilever since $\tau \sim 1/L^2$, although the responsivity will be reduced as a trade-off. Compared to quantum detectors in this range of the electromagnetic

spectrum, our thermal detector has the advantage of room temperature (uncooled) operation.

7.4. Conclusions

We have demonstrated detection of infrared radiation with a performance comparable to the state-of-the-art thermal detectors by a plasmo-thermomechanical detector that utilizes a plasmonic nanoantenna based infrared absorber as an integrated part of a nanomechanical resonator with a novel interferometric fiberoptic read-out. With further improvement in the device implementation, our simulations predict that the minimum detectable optical power can be decreased by two orders of magnitude outperforming commercially available thermal infrared detectors. Although the demonstrated PlasMIRD detects mid-IR radiation at 6μm, its working wavelength range can be tuned to near infrared or terahertz region by modifying the dimensions of the nanoantenna absorber [35, 51]. Broadband IR detection can be realized by integrating nanoantennas with different resonant wavelengths onto the detector. We believe that our approach that uniquely combines advantages of nanoplasmonics and nanomechanics on a compact device platform will open up innovative research directions in on-chip surface enhanced biomolecular infrared and mass spectroscopies.

7.5. Contributions

In this project of plasmo-thermomechanical IR detector, I have explored the preliminary design of the IR absorption component by FDTD simulation. I have designed and built the high-vacuum measurement chamber, as well as some parts of the optical

measurement system. I have performed the focused ion beam (FIB) milling to cut the membrane into nanobeams, and SEM characterization of the sample.

7.6. References

1. Bharadwaj, P., B. Deutsch, and L. Novotny, *Optical Antennas.* Advances in Optics and Photonics, 2009. **1**(3): p. 438-483.
2. Novotny, L. and N. van Hulst, *Antennas for light.* Nature Photonics, 2011. **5**(2): p. 83-90.
3. Tang, L., et al., *Nanometre-scale germanium photodetector enhanced by a near-infrared dipole antenna.* Nature Photonics, 2008. **2**(4): p. 226-229.
4. Cubukcu, E., et al., *Plasmonic Laser Antennas and Related Devices.* Ieee Journal of Selected Topics in Quantum Electronics, 2008. **14**(6): p. 1448-1461.
5. Cubukcu, E. and F. Capasso, *Optical nanorod antennas as dispersive one-dimensional Fabry-Perot resonators for surface plasmons.* Applied Physics Letters, 2009. **95**(20).
6. Cao, L.Y., et al., *Resonant Germanium Nanoantenna Photodetectors.* Nano Letters, 2010. **10**(4): p. 1229-1233.
7. Cubukcu, E., et al., *Plasmonic laser antenna.* Applied Physics Letters, 2006. **89**(9).
8. Pillai, S., et al., *Surface plasmon enhanced silicon solar cells.* Journal of Applied Physics, 2007. **101**(9).
9. Anker, J.N., et al., *Biosensing with plasmonic nanosensors.* Nature Materials, 2008. **7**(6): p. 442-453.
10. De Wilde, Y., et al., *Thermal radiation scanning tunnelling microscopy.* Nature, 2006. **444**(7120): p. 740-743.
11. Schuller, J.A., T. Taubner, and M.L. Brongersma, *Optical antenna thermal emitters.* Nature Photonics, 2009. **3**(11): p. 658-661.
12. Novotny, L. and S.J. Stranick, *Near-field optical microscopy and spectroscopy with pointed probes.* Annual Review of Physical Chemistry, 2006. **57**: p. 303-331.
13. Govorov, A.O. and H.H. Richardson, *Generating heat with metal nanoparticles.* Nano Today, 2007. **2**(1): p. 30-38.
14. Richardson, H.H., et al., *Thermooptical properties of gold nanoparticles embedded in ice: Characterization of heat generation and melting.* Nano Letters, 2006. **6**(4): p. 783-788.

15. Wang, J., et al., *Photothermal reshaping of gold nanoparticles in a plasmonic absorber.* Optics Express, 2011. **19**(15): p. 14726-14734.

16. Baffou, G., R. Quidant, and C. Girard, *Heat generation in plasmonic nanostructures: Influence of morphology.* Applied Physics Letters, 2009. **94**(15).

17. Baffou, G., R. Quidant, and F.J.G. de Abajo, *Nanoscale Control of Optical Heating in Complex Plasmonic Systems.* Acs Nano, 2010. **4**(2): p. 709-716.

18. Loo, C., et al., *Nanoshell-enabled photonics-based imaging and therapy of cancer.* Technology in Cancer Research & Treatment, 2004. **3**(1): p. 33-40.

19. Lal, S., S.E. Clare, and N.J. Halas, *Nanoshell-Enabled Photothermal Cancer Therapy: Impending Clinical Impact.* Accounts of Chemical Research, 2008. **41**(12): p. 1842-1851.

20. O'Neal, D.P., et al., *Photo-thermal tumor ablation in mice using near infrared-absorbing nanoparticles.* Cancer Letters, 2004. **209**(2): p. 171-176.

21. Han, S.E. and D.J. Norris, *Beaming thermal emission from hot metallic bull's eyes.* Optics Express, 2010. **18**(5): p. 4829-4837.

22. Wu, C.H., et al., *Metamaterial-based integrated plasmonic absorber/emitter for solar thermo-photovoltaic systems.* Journal of Optics, 2012. **14**(2).

23. Sun, X.K., et al., *Femtogram Doubly Clamped Nanomechanical Resonators Embedded in a High-Q Two-Dimensional Photonic Crystal Nanocavity.* Nano Letters, 2012. **12**(5): p. 2299-2305.

24. Naik, A.K., et al., *Towards single-molecule nanomechanical mass spectrometry.* Nature Nanotechnology, 2009. **4**(7): p. 445-450.

25. Yang, Y.T., et al., *Zeptogram-scale nanomechanical mass sensing.* Nano Letters, 2006. **6**(4): p. 583-586.

26. Jensen, K., K. Kim, and A. Zettl, *An atomic-resolution nanomechanical mass sensor.* Nature Nanotechnology, 2008. **3**(9): p. 533-537.

27. Teufel, J.D., et al., *Nanomechanical motion measured with an imprecision below that at the standard quantum limit.* Nature Nanotechnology, 2009. **4**(12): p. 820-823.

28. LaHaye, M.D., et al., *Approaching the quantum limit of a nanomechanical resonator.* Science, 2004. **304**(5667): p. 74-77.

29. Knobel, R.G. and A.N. Cleland, *Nanometre-scale displacement sensing using a single electron transistor.* Nature, 2003. **424**(6946): p. 291-293.

30. Kenny, T.W., et al., *Novel Infrared Detector Based on a Tunneling Displacement Transducer.* Applied Physics Letters, 1991. **59**(15): p. 1820-1822.

31. Barnes, J.R., et al., *Photothermal Spectroscopy with Femtojoule Sensitivity Using a Micromechanical Device.* Nature, 1994. **372**(6501): p. 79-81.

32. Barnes, J.R., et al., *A Femtojoule Calorimeter Using Micromechanical Sensors.* Review of Scientific Instruments, 1994. **65**(12): p. 3793-3798.

33. Lai, J., et al., *Optimization and performance of high-resolution micro-optomechanical thermal sensors.* Sensors and Actuators a-Physical, 1997. **58**(2): p. 113-119.

34. Toda, M., et al., *Evaluation of bimaterial cantilever beam for heat sensing at atmospheric pressure.* Review of Scientific Instruments, 2010. **81**(5).

35. Tao, H., et al., *Microwave and Terahertz wave sensing with metamaterials.* Optics Express, 2011. **19**(22): p. 21620-21626.

36. Rasool, H.I., et al., *A low noise all-fiber interferometer for high resolution frequency modulated atomic force microscopy imaging in liquids.* Review of Scientific Instruments, 2010. **81**(2).

37. Zhu, H., F. Yi, and E. Cubukcu, *Nanoantenna Absorbers for Thermal Detectors.* Ieee Photonics Technology Letters, 2012. **24**(14): p. 1194-1196.

38. Shchegolkov, D.Y., et al., *Perfect subwavelength fishnetlike metamaterial-based film terahertz absorbers.* Physical Review B, 2010. **82**(20).

39. Wu, C.H., et al., *Large-area wide-angle spectrally selective plasmonic absorber.* Physical Review B, 2011. **84**(7).

40. Liu, X.L., et al., *Infrared Spatial and Frequency Selective Metamaterial with Near-Unity Absorbance.* Physical Review Letters, 2010. **104**(20).

41. Bosman, H., Y.Y. Lau, and R.M. Gilgenbach, *Microwave absorption on a thin film.* Applied Physics Letters, 2003. **82**(9): p. 1353-1355.

42. Muhlschlegel, P., et al., *Resonant optical antennas.* Science, 2005. **308**(5728): p. 1607-1609.

43. Ozisik, M.N., *Heat conduction*. 2nd ed. 1993, New York ; Toronto: J. Wiley. xvii, 692 p.

44. Bergman, T.L., et al., *Fundamentals of heat and mass transfer*. 2011: Wiley.

45. Bergman, T.L., et al., *Fundamentals of heat and mass transfer*. 7th ed. 2011, Hoboken, NJ: Wiley. xxiii, 1048 p.

46. Roark, R.J. and W.C. Young, *Formulas for stress and strain*. 5th ed. 1975, New York: McGraw-Hill. xvi, 624 p.

47. Kruse, P.W., *Uncooled thermal imaging : arrays, systems, and applications*. Tutorial texts in optical engineering. 2001, Bellingham, Wash., USA: SPIE Press. xviii, 89 p.

48. Gabrielson, T.B., *Mechanical-Thermal Noise in Micromachined Acoustic and Vibration Sensors.* Ieee Transactions on Electron Devices, 1993. **40**(5): p. 903-909.

49. Majorana, E. and Y. Ogawa, *Mechanical thermal noise in coupled oscillators.* Physics Letters A, 1997. **233**(3): p. 162-168.

50. Kwon, H., et al., *Micro-optical fiber coupler on silicon bench based on microelectromechanical systems technology.* Japanese Journal of Applied Physics Part 1-Regular Papers Brief Communications & Review Papers, 2007. **46**(8B): p. 5473-5477.

51. Tao, H., et al., *A metamaterial absorber for the terahertz regime: Design, fabrication and characterization.* Optics Express, 2008. **16**(10): p. 7181-7188.

CHAPTER 8: A BIOSENSOR BASED ON LEAKY CAVITY MODE RESONANCES IN SILICON NANOWIRES

This chapter is majorly adopted from:

"Silicon-on-Glass Graphene-Functionalized Leaky Cavity Mode Nanophotonic Biosensor", Qiushi Guo, Hai Zhu, Feng Liu, Alexander Y. Zhu, Jason C. Reed, Fei Yi, and Ertugrul Cubukcu, *ACS Photonics*, 1 (3), (2014)

8.1. Introduction

Nanoscale dielectric structures have recently attracted significant interest for optical waveguiding and enhanced light absorption [1-8] utilizing low loss and geometry-dependent leaky modes [9-14]. This strong Mie-like resonance results from the excitation of large displacement currents inside the dielectric cavity. They are thus ideal candidates for a broad range of applications, such as light-trapping in solar cells [15, 16] and enabling optical antennas for ultra-compact photodetectors [13, 16, 17]. In particular, owing to their small feature sizes, the fundamental resonance property of deep-subwavelength dielectric structures is leaky. This is in contrast to the interface dominated surface plasmon (SP) type effects present in their metallic counterparts [18-23]. The significant extension of the electric near-field into the bulk environment effectively associates the spectral position of the resonance to the surrounding refractive index, opening up the possibility for such structures to be used for sensing applications via time and cost efficient optical signal transduction methods.

Silicon is an ideal material of choice for resonant Mie cavities in the visible spectrum due to its high refractive index, relatively low intrinsic losses, and ease of integration with existing opto-electronic infrastructure. Here, we experimentally

demonstrate a graphene functionalized Si LCMR biosensor with a label-free protein detection floor of approximately 300 pM, which is limited by spectrometer resolution. Graphene is known to possess a relatively high affinity for various biomolecules such as nucleic acids [24, 25] and proteins [26, 27] by virtue of $\pi - \pi$ and Van der Waals' interactions [28, 29]. Furthermore, the atomically thin graphene exhibits low absorption in the visible [30], preserving the excellent near field properties and thus the sensing ability of leaky Si based resonators. The biosensing framework eliminates the need for complicated alignment-sensitive coupling schemes, which is widely used in high quality factor dielectric microcavities, such as photonic crystals [31] and whispering gallery mode microtoroid resonators [32]. Moreover, the proposed sensor platform is fully compatible with the standard complementary metal oxide semiconductor (CMOS) fabrication process, which can enable a new generation of chip-based ultraportable bioanalysis systems.

8.2. Design and Principles of the Leaky Cavity Mode Resonance Biosensor

8.2.a. Overview of the Silicon Nanowire Biosensor

The LCMR biosensor relies on an optical coupling scheme distinct from the leaky waveguide mode biosensor [33], high quality factor microcavity based sensors [31, 32] and surface plasmon resonance (SPR) sensors [34]. In this scheme, normally incident light is free-space coupled to the LCMR sensor and scattered light is collected through the excitation optics similar to schemes employed for localized surface plasmon resonance (LSPR) sensors. As previously mentioned in the introduction, this eliminates the need for alignment sensitive coupling schemes, where coupling and extraction losses on both ends

must be taken into account, while enabling the use of inexpensive visible optical components. Figure 8-36(A) illustrates the sensing scheme and the structure of the graphene functionalized silicon nanowire (SiNW) LCMR biosensor. The biosensor comprises a top-down fabricated SiNW array on a glass substrate, which couples the normally incident light to LCMR modes. This resonance wavelength is strongly dependent upon the effective refractive index of the surrounding medium. Thus when biomolecules bind to the graphene/sensor surface, the effective local refractive index increases and leads to a redshift of the LCMR, which is directly observable via far-field measurement techniques. The close-up scanning electron microscopy (SEM) images of the fabricated SiNW array are given in Figure 8-36(B) and (C). The SEM images reveal the excellent uniformity in both the nanowire shape and size.

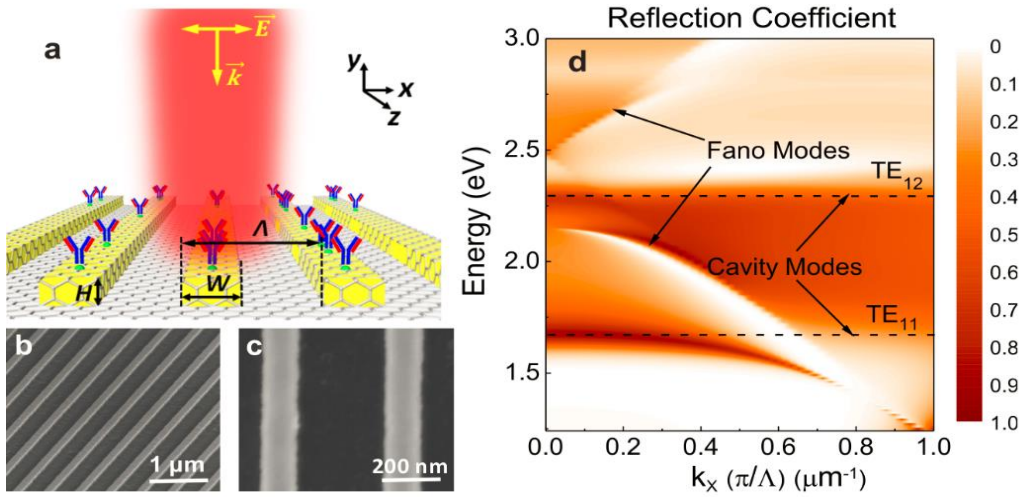

Figure 8-36. An overview of the LCMR sensor and its optical properties. (A) Schematic representation of a SiNW array on a glass substrate, oriented transverse to the light polarization. The graphene monolayer overlaid on the SiNW array facilitates the adsorption of various biomolecules. The array period, nanowire height, and width are denoted by Λ, H, and W, respectively. (B) SEM image of the 60° tilted SiNW array. The overall extent is 100 μm × 100 μm. (C) Magnified top view of SiNW array under SEM. The nanowires have a width of 140 nm, with a

periodicity of 500 nm. (d) Photonic band diagram showing the reflection coefficient for the periodic SiNW array in the (ω, k_x) plane. The dashed lines correspond to analytically derived resonance positions for TE_{11} and TE_{12} mode. The parameters of the structure are Λ=500 nm, W=H=140 nm. The TE_{11} resonance remains the same up to k_x=0.5 μm^{-1} , corresponding to an incidence angle of ~48° and a numerical aperture of ~0.375, before diffractive effects become pronounced.

8.2.b. Microscopic Mechanisms for Light Absorption

Figure 8-36 (D) shows the photonic band diagram of the structure for the *E*-field polarized along the *x* direction (TE polarization), which was calculated from the angle dependence of the optical reflection by employing the 2D transfer matrix method. The parameters of the simulated structure are Λ=500 nm, W=H=140 nm. The two bands corresponding to the cavity modes are clearly visible in Figure 8-36 (D), which are flat in shape since the resonance conditions are primarily determined by the geometry of the cavity. Also present are narrow bands due to Fano or guided-mode resonances [35, 36] that are sensitive to the incidence angle, with low reflection intensity under normal incidence. The excitation of Fano mode results from the interplay between the incident light and the excited guided waves in the *x* direction [37-41].

Analytically, since the nanowire is infinitely long but finite in x and y, the solution is two dimensional ($\partial \mathbf{E} / \partial z = 0$): the SiNW can be considered as a two-dimensional rectangular resonator with standing waves in both x and y axes, which satisfy the requirement of momentum conservation:

$$\left(n_{Si} \frac{\omega}{c} \right)^2 = k_x^2 + k_y^2 \tag{139}$$

, where n_{Si} is the complex refractive index of silicon, ω is the complex resonance frequency (ω=Re(ω)+iIm(ω)) of the cavity. Re(ω) represents the oscillation frequency of the optical

field in the visible regime and Im(ω) is the attenuation due to the loss (both material and radiation). c is the speed of light in vacuum, and k_x and k_y are the wavevectors in the x and y directions, respectively. The SiNW is both absorptive and radiative, giving rise to the complex solutions of k_x=Re(k_x)+iIm(k_x) and k_y=Re(k_y)+iIm(k_y). From the boundary conditions, the imaginary parts of the wavevectors inside nanowire enable the boundary radiation, leading to radiation loss outside, which have been termed "leaky mode resonances" in the literature [16, 42, 43]. Re(k_x) and Re(k_y) can be determined by the standing wave condition:

$$\mathrm{Re}(k_x)W + 2\varphi_1 = m\pi, (m = 1, 2, \cdots) \tag{140}$$

$$\mathrm{Re}(k_y)W + \varphi_1 + \varphi_2 = n\pi, (n = 1, 2, \cdots) \tag{141}$$

, where φ_1 is the reflection associated phase shift at the interface between silicon and air, φ_2 is that between silicon and silica, and m and n are integers defining the mode orders in the x and y directions, respectively. The phase shifts of the resonances at the nanowire boundaries can be attributed to the absorptive features of SiNW in the visible light regime. It can be determined by solving the reflection coefficient r under normal incidence using standard Fresnel equations:

$$r_1 = |r_1| e^{i\varphi_1} = \frac{n_{Si} - 1}{n_{Si} + 1} \tag{142}$$

$$r_2 = |r_2| e^{i\varphi_2} = \frac{n_{Si} - n_{SiO_2}}{n_{Si} + n_{SiO_2}} \tag{143}$$

, where r_1 and r_2 are the complex reflection coefficients at Si-air and Si-SiO_2 interfaces, respectively. n_{SiO2} denotes the refractive index of glass. From the above

equations, the rectangular cavity resonance position with different orders can be analytically derived. For instance, the TE_{11} cavity mode corresponds to 743 nm and the mode TE_{12} corresponds to 549 nm in the reflection spectra (dashed lines in Figure 8-36(D)), which are in good agreement with the calculated band diagram.

8.2.c. Resonance Wavelength and Nanowire Cross-section Shape

As predicted by the above theoretical description, the LCMR wavelength can be tuned simply by changing the nanowire width and height. Tuning of leaky mode resonances with feature sizes is readily observable under an optical microscope: Figure 8-37(A) illustrates four amorphous SiNW arrays, each covering a 100 μm × 100 μm area, fabricated on a glass substrate. The nanowire widths are varied from 150 nm to 180 nm in steps of 10 nm. The progressive color change of SiNW arrays with varied sizes and periods can be seen in Figure 8-37(A). At a fixed interspacing of 350 nm, a light yellow color is observed for a 150 nm SiNW array, and the color gradually changes to orange and then to red as the NW size increases to 180 nm. Through the inspection of the reflection spectra of corresponding SiNW arrays, more quantitative measurements consistent with the observed color variation are illustrated in Figure 8-37(C). Figure 8-37(C) reveals that nanowires with widths of 150, 160, 170, and 180 nm give rise to resonance peaks at λ_0 = 722, 751, 777, 808 nm, respectively, with an average spectral shift of 28.7 nm for each 10 nm step.

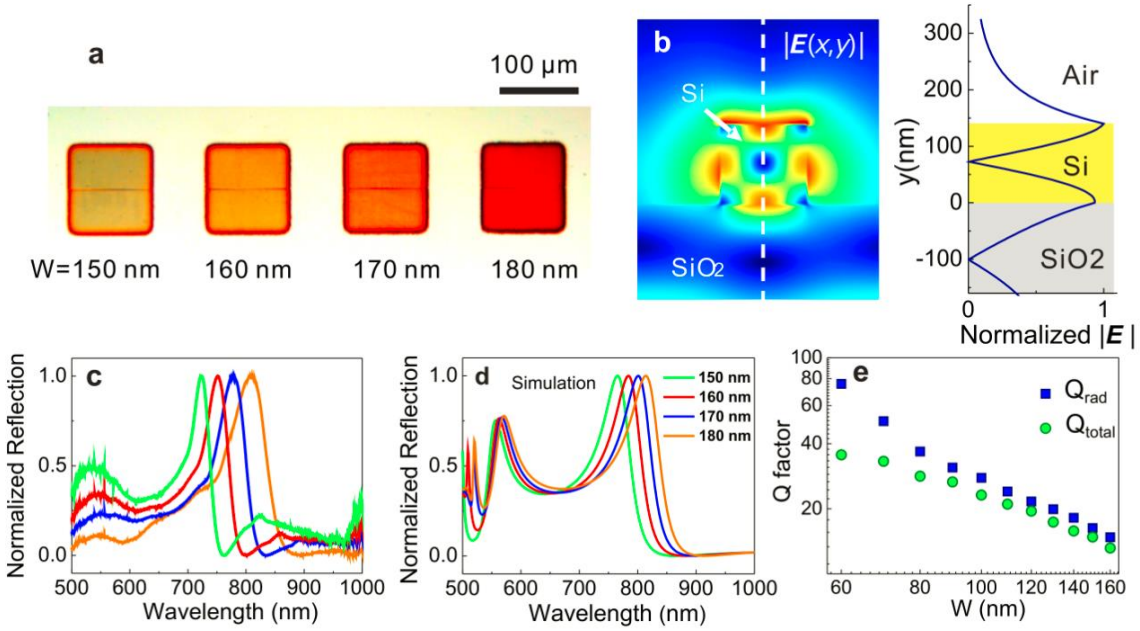

Figure 8-37. Size-dependent multicolor reflection of SiNW arrays. (A) Bright-field optical microscope images showing SiNW arrays of different widths, and constant NW interspacing of 350 nm. (B) The simulated electric field intensity distribution of TE_{11} leaky cavity mode for a typical nanowire array with $W \times H$=150 nm × **140** nm, Λ=500 nm at λ=765 nm. The near-field distribution along the broken line in (B) illustrates the strong field localization with sufficient modal overlap with the surrounding medium. (C) Measured normalized reflection coefficient under TE incident light for representative SiNWs with W=150 nm (green), 160 nm (red), 170 nm (blue), and 180 nm (orange). (D) The corresponding simulated reflection spectra of the same arrays. (E) FDTD calculated total quality factor (Q_{total}) and radiation quality factor (Q_{rad}) as functions of the cavity side length W.

The FDTD-simulated reflection spectrum is in good qualitative and reasonable quantitative agreement with the experiment in terms of the resonance position as well as the line shape, as shown in Figure 8-37 (C) and (D). It is worth noting that tabulated data for crystalline silicon was used in the simulation since the optical property of amorphous silicon varies greatly for different compositions. In addition, simulated spectra by incorporating the crystalline silicon data show better agreement with the experimental. As can be seen from Figure 8-37 (C) and (D), the differences in peak positions between

experimental and simulation results originate from two factors. First, the fabricated silicon nanostructures are amorphous and thus have inferior optical properties than those tabulated for single crystal materials. Second, the etched SiNW structures are not perfectly rectangular in cross-section.

As revealed by the experimental results, the LCMR are spectrally narrow (FWHM as narrow as 50-60 nm) with quality (Q) factors of 18.5 15.1, 13.9, and 11.9 for 150, 160, 170, and 180 nm nanowire arrays, respectively. It is expected that the Q factor of LCMR can be further improved by optimizing the structure since the linewidth of dielectric Mie resonance is strongly size dependent. In fact, low dissipation resonators with high Q factors are particularly favorable for monitoring perturbations of the resonance signal and thus for detecting biomolecules of low concentrations. It ought to be noted here that in our LMCR system with a feature size above 70 nm, the dominant loss mechanism is the radiation loss of the cavity mode due to lack of total internal reflection. The radiation quality factor (Q_{rad}) can be found by setting the imaginary part of the Si refractive index to be zero in computer simulations and thereby removing the intrinsic loss. Figure 8-37(E) shows the simulated radiation Q factor and total Q factor (Q_{total}) values as functions of the cavity side length W for the TE_{11} cavity mode, plotted with a logarithmic scale. Both Q_{rad} and Q_{total} increase as the cavity shrinks, but Q_{total} increases much slower since material loss becomes more pronounced for smaller resonance wavelengths. This unique behavior of Q_{rad} and Q_{total} for the 2-D leaky subwavelength cavity is significantly different from that for dielectric optical cavities with dimensions larger than the wavelength, such as in microtoroids [44], where the total internal reflection induced Q_{rad} decreases when the cavity becomes smaller due to

the larger surface curvature leading to increased radiation leakage. Shrinking of nanowire cross-section gives rise to larger values of stored electromagnetic energy and thus higher *Q* factor [45]. The easily-tunable LCMR excited in deep-subwavelength dielectric NW structures becomes intriguing because dielectric materials, for instance, silicon, have much lower optical losses compared to metals.

8.2.d. Refractive Index Sensitivity of the Leaky Cavity Mode Resonance

For sensing applications, the near-field confinement is the key feature. Figure 8-37(B) shows a plot of the TE_{11} total near field profile $|E(x,y)|$ for a periodic SiNW array calculated based on the fabricated nanowire geometry assuming TE-polarized plane wave illumination. The nanowire confined TE_{11} mode with a significant near field intensity at the interface extends into the surrounding medium with an exponential decay constant δ_d=62 nm (Figure 8-37(B)). Owing to its leaky nature and spectrally sharp far-field properties, the LCMR sensor can be used to sense the refractive index changes in the surrounding environment. Figure 8-38 shows the responses of four SiNW arrays for a finely controlled refractive index range (n = 1.40 – 1.45). Measuring the resonance peak shift as a function of the index, we determine the bulk refractive index sensitivity $d\lambda/dn$ to be as high as 213 nm/RIU, which is greater than that of localized surface plasmon resonance (LSPR) sensors [46]. This is as expected due to the larger field decay length δ_d (~60 nm) compared to the LSPR sensors (~20 nm). This characteristic of LCMR allows for better near-field overlap with the surrounding media. With a spectrometer-limited

resolution of 0.6 nm and the sensitivity of approximately 200 nm/RIU, the minimum detectable refractive index change can be estimated as 3×10^{-3} RIU.

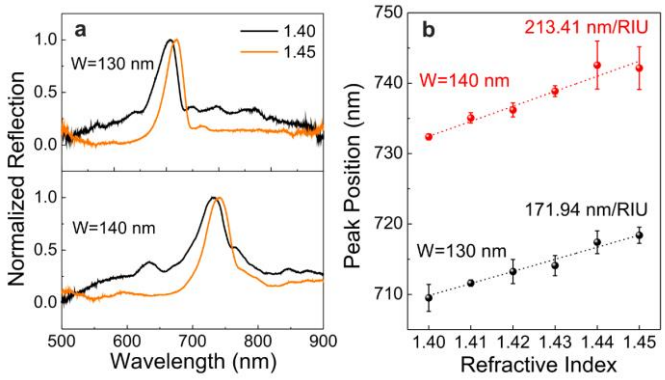

Figure 8-38. Experimental bulk sensitivities of the LCMR sensor over a small index range. The sensitivities of the spectral shifts (dλ/dn) for the SiNW arrays with widths of 130, 140 nm are 171.94 nm/RIU, 213.41 nm/RIU, respectively. Error bars represent standard deviation of 4 individual arrays with identical sizes.

8.3. Graphene-functionalized Surface Molecule Binding and Its Detection

We also investigate the ability of SiNW LCMR sensor to detect low concentration label-free protein binding events. This requires the functionalization of the silicon sensor for target-receptor type sensing as done with field-effect transistor (FET) silicon nanowire sensors [47, 48]. Conventionally, Si surfaces are functionalized through a time-consuming process by introducing amino groups or carboxylic functional groups [47] such as 3-Aminopropyltriethoxysilane (APTES) (9 ± 1 Å for monolayer) , which is capable of vertically polymerizing in the presence of water [49]. As a result, this method potentially suffers from the disadvantages of grating efficiency degradation [50] in optical sensors and thermal instability, particularly due to the loss of covalently attached silane layers in aqueous media at 40 ℃ [49]. As an atomically thin, readily applicable, and stable

alternative, we use a graphene monolayer overlaid on the SiNW array for sensor functionalization and promoting efficient protein adsorption. To test the efficacy of this approach, a graphene sheet grown by chemical vapor deposition[51](CVD) was mechanically transferred onto the SiNW arrays. Besides acting as a functionalization layer, graphene monolayer is only 0.355 nm in thickness with only 2.3% absorption in the visible regime and with around 5.5% absorption further increased by the LCMR, which implies that the SiNW resonance and the corresponding optical near-fields are minimally perturbed. The quality of the transferred graphene monolayer is verified through Raman spectroscopy producing a high 2D/G peak ratio and almost negligible D peak intensity (Figure 8-39(A)).

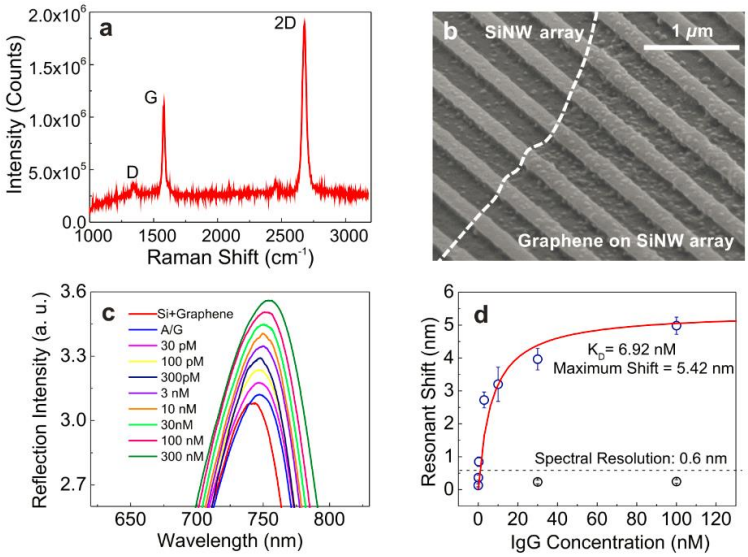

Figure 8-39. Demonstration of LCMR SiNW array in immunodetection. (a) Raman spectrum corresponds to the graphene covered area. Relative intensities of the G and 2D bands suggest monolayer graphene. Absence of a significant D peak further indicates that the graphene layer is of high quality and is largely defect free. (b) SEM image of SiNW arrays after loading with 100 nM of IgG protein. Dashed line sketches the boundary between the covered and non-covered areas. (c) Response of an A/G functionalized graphene covered LCMR sensor to IgG antibody with various concentrations, ranging from 30 pM to 300 nM. A/G on graphene serves as a specific binding intermediary while IgG antibodies are the target molecules. (d) Resonant wavelength shift

in response to specific binding of IgG antibody with A/G protein on graphene enabled LCMR sensor for various concentrations. The wavelength shift is taken as the value ~30 min after buffer solution wash, the red curve is fitted using the Langmuir isotherm. The error bars present standard deviation values on the mean, for multiple measurements (n=4). Black circles below the detection limit (horizontal dashed line) show the negative control with nonspecific binding on to bare silicon surfaces.

For proximity protein sensing with the LCMR sensor we use the commercially available immunoglobulin G (IgG) antibody (Pierce). Protein A/G (Pierce), a recombinant fusion protein constituting binding domains of both protein A and protein G was employed as the binding intermediary due to its high affinity to Fc receptors of IgG [52-54]. It effectively reduces nonspecific binding sites in the course of experiments, allowing for better sensitivity and specificity. Figure 8-39(B) shows a tilted view of a typical graphene functionalized SiNW array after spotting 1 mg/mL A/G and 100 nM IgG. The dashed line defines the boundary between the graphene covered and bare SiNW regions. It is clearly observed that the surface density of IgG antibody attached to the graphene surface is much greater than that of the bare silicon, demonstrating the effectiveness of graphene as a protein functionalization layer. As shown in Figure 8-39(C), the accumulated biomass on the graphene surface increases the local refractive index, resulting in a redshift of the spectral positions of the LCMR resonances ($\Delta\lambda \approx 5\ n$m after addition of 1 mg/mL protein A/G). To assess the detection limit and quantify the performance of our sensing device, IgG antibodies in 0.01M phosphate buffer (pH=7.4) were prepared at various concentrations. The sequentially diluted protein concentrations were verified with UV absorption spectroscopy as far as possible to ensure accurate determination of the binding affinity of IgG to our device. Each measurement was individually calibrated by calculating

the relative peak shift with respect to the A/G-Graphene functionalized device. Figure 8-39(D) indicates that the functional dependence of the sensor response to added protein concentration is well divided into two regimes: an initial, linear regime where the peak shift is proportional to the concentration, and a saturation regime where most of the binding sites are occupied by protein molecules. This is expected, since the sensing response is a surface adsorption process and can be accurately modeled by the well-known Langmuir isotherm [55]. Accordingly, we assume that the resonance peak position shift $\Delta\lambda$ is proportional to the fractional surface coverage (θ) such that $\Delta\lambda = \Delta\lambda_{max} \cdot\theta=\Delta\lambda_{max}\cdot c/(K_D+c)$. Here c is the IgG concentration (M) and $\Delta\lambda_{max}$ is the maximum LCMR shift (nm), which is proportional to the binding site surface density N ($1/m^2$) and the mode confinement factor. A lower K_D, the equilibrium dissociation constant (M), corresponds to greater binding affinity or greater adhesion strength [56]. From the fitting (solid curve in Figure 8-39(D)), we determined the average equilibrium dissociation constant K_D of the IgG-A/G binding to be 6.92 nM. Error bars signify the standard deviation of 4 individual, identical arrays, suggesting excellent reproducibility. Given the spectrometer resolution of 0.6 nm, we find a lower detection limit of 300 pM, as shown in Figure 8-39(D). The fit also gives the calibrated maximum IgG sensing response $\Delta\lambda_{max}$=5.42 nm. The control experiments (black circles) without graphene functionalization were also carried out as shown in Figure 8-39(D). We see the magnitude of resonant shift upon spotting of 30 and 100 nM IgG lies below the noise level, implying that limited amount of binding sites remain after the post-incubation rinse. This can be understood as bare SiNW arrays with native oxide contain silanol groups on the surface that exhibit extremely low binding affinity to biomolecules,

before functionalization with amine or carboxylic groups [47]. This fact is strongly suggestive of the necessity of the graphene functionalization step in enabling the SiNWs to be used for optical biosensing purposes.

Finally, it is also important to note that there are numerous potential approaches that can further improve the detection limit as well as extend the dynamic range of our LCMR sensor. One is to use a single laser and detector sensing scheme for in-situ monitoring of the reflected light intensity change in response to the changes in the bulk or local refractive index. The reflection intensity (I) sensitivity to the local refractive index (n) can be expressed as $dI/dn = dI/d\lambda \times d\lambda/dn$. For a specific resonator system, $d\lambda/dn$ is the spectral sensitivity that is determined by the magnitude of local electric field, together with the field confinement factor of the resonator. The spectrally sharp LCMR (FWHM: 50-60 nm) in the visible region results in a very steep slope (large $|dI/d\lambda|$) around the resonance, which can, in turn, compensate for weaker field confinement and resultant spectral sensitivity. In fact, compared to spectrometer-based sensing techniques for which the minimum detectable spectral shift is often limited by the spectral resolution of a diffractive element, a photodetector with a shot noise limited performance is expected to offer much improved detection limit for the light intensity. By combining such an approach with active spatial modulation of the sensor with respect to the beam, even single protein level detection can be achieved through lock-in demodulation schemes by effectively removing background response, leading to very high signal-to-background levels [57]. For instance, a laser-detector implementation of the LCMR sensor compares favorably with the LSPR sensor while being compatible with CMOS fabrication processes, unlike the latter which relies on gold (which acts as a contaminating dopant in CMOS process). The integrated

silicon in the LCMR can also be directly used as an on-chip photoconductive detector, circumventing the need for bulky external detectors and collection optics. In addition, by fabricating the LCMR sensor on the silicon-on-insulator platform, it is also possible to combine LCMR optical sensing with electrical sensing by using the SiNWs as a FET sensor [58] on the same chip leading to multimodal proximity sensing.

8.3. Fabrication Process of the Silicon-on-Glass Device

First, an amorphous silicon layer of 140 nm was deposited on a glass substrate by PECVD (Oxford PlasmaLab 100), and one ZEP 520A resist layer of ~400 nm was spin coated onto the silicon. Then, the NW array patterns were transferred by e-beam lithography (Elionix ELS-7500EX), and developed by O-xylene. The ZEP 520A resist worked as the mask for the reactive ion etching process (Oxford 80 Plus) to remove part of the silicon, leaving the NW arrays. The height of the SiNW array is confirmed by atomic force microscopy.

8.4. Conclusions.

The utilization of LCMR in deep-subwavelength SiNW arrays together with graphene's ability to adsorb various biomolecules results in a promising silicon-on-glass platform for future applications in on-chip photonic bio-analytics. It combines the advantages of having a compact footprint (some 100 μm×100 μm or less), easy alignment-insensitive input-output coupling schemes, low unit cost, label-free detection, amenability for up-scaling, and integration with silicon based photonics. We have demonstrated that such low loss leaky cavity mode resonances exhibit bulk refractive index sensitivities up

to 213 nm/RIU, and a protein sensing limit on the order of ng/mL. For future extensions, the concept of LMCR is extremely general and can be utilized to build sensors on a wide variety of semiconductor materials and geometries. Also importantly, our proposed sensor platform is expected to bring up exciting opportunities for multimodal sensing schemes.

8.5. Contributions

In this project of leaky mode biosensor, I have performed the FDTD simulations for the silicon nanowaire array design. I have developed the fabrication process, including lithography and dry-etch, and implemented the fabrication. I have characterized the topography of the Si nanowire arrays by AFM. I have performed Raman spectroscopy characterization on the graphene, and SEM characterization of the sample.

8.6. References

1. Seo, K., et al., *Multicolored Vertical Silicon Nanowires.* Nano Letters, 2011. **11**(4): p. 1851-1856.
2. Seo, M.K., et al., *Modal Characteristics in a Single-Nanowire Cavity with a Triangular Cross Section.* Nano Letters, 2008. **8**(12): p. 4534-4538.
3. Wang, B.M. and P.W. Leu, *Tunable and selective resonant absorption in vertical nanowires.* Optics Letters, 2012. **37**(18): p. 3756-3758.
4. Aydin, K., et al., *Broadband polarization-independent resonant light absorption using ultrathin plasmonic super absorbers.* Nature Communications, 2011. **2**.
5. Liu, N., et al., *Infrared Perfect Absorber and Its Application As Plasmonic Sensor.* Nano Letters, 2010. **10**(7): p. 2342-2348.
6. Wang, B.M. and P.W. Leu, *Enhanced absorption in silicon nanocone arrays for photovoltaics.* Nanotechnology, 2012. **23**(19).
7. Zhu, J., et al., *Optical Absorption Enhancement in Amorphous Silicon Nanowire and Nanocone Arrays.* Nano Letters, 2009. **9**(1): p. 279-282.

8. Kuttge, M., F.J.G. de Abajo, and A. Polman, *Ultrasmall Mode Volume Plasmonic Nanodisk Resonators.* Nano Letters, 2010. **10**(5): p. 1537-1541.

9. Paniagua-Dominguez, R., D.R. Abujetas, and J.A. Sanchez-Gil, *Ultra low-loss, isotropic optical negative-index metamaterial based on hybrid metal-semiconductor nanowires.* Scientific Reports, 2013. **3**.

10. Coenen, T., J. van de Groep, and A. Polman, *Resonant Modes of Single Silicon Nanocavities Excited by Electron Irradiation.* Acs Nano, 2013. **7**(2): p. 1689-1698.

11. Fu, Y.H., et al., *Directional visible light scattering by silicon nanoparticles.* Nature Communications, 2013. **4**.

12. Kuznetsov, A.I., et al., *Magnetic light.* Scientific Reports, 2012. **2**.

13. Cao, L.Y., et al., *Engineering light absorption in semiconductor nanowire devices.* Nature Materials, 2009. **8**(8): p. 643-647.

14. Spinelli, P., M.A. Verschuuren, and A. Polman, *Broadband omnidirectional antireflection coating based on subwavelength surface Mie resonators.* Nature Communications, 2012. **3**.

15. Yu, Y.L., et al., *Dielectric Core-Shell Optical Antennas for Strong Solar Absorption Enhancement.* Nano Letters, 2012. **12**(7): p. 3674-3681.

16. Cao, L., et al., *Semiconductor nanowire optical antenna solar absorbers.* Nano letters, 2010. **10**(2): p. 439-445.

17. Fan, P.Y., et al., *An invisible metal-semiconductor photodetector.* Nature Photonics, 2012. **6**(6): p. 380-385.

18. Barnes, W.L., A. Dereux, and T.W. Ebbesen, *Surface plasmon subwavelength optics.* Nature, 2003. **424**(6950): p. 824-830.

19. Xia, Y.N. and N.J. Halas, *Shape-controlled synthesis and surface plasmonic properties of metallic nanostructures.* Mrs Bulletin, 2005. **30**(5): p. 338-344.

20. Prodan, E., et al., *A hybridization model for the plasmon response of complex nanostructures.* Science, 2003. **302**(5644): p. 419-422.

21. Lal, S., S. Link, and N.J. Halas, *Nano-optics from sensing to waveguiding.* Nature Photonics, 2007. **1**(11): p. 641-648.

22. Chen, S., et al., *Plasmon-Enhanced Enzyme-Linked Immunosorbent Assay on Large Arrays of Individual Particles Made by Electron Beam Lithography.* Acs Nano, 2013. **7**(10): p. 8824-8832.

23. Dahlin, A.B., et al., *Promises and challenges of nanoplasmonic devices for refractometric biosensing.* Nanophotonics, 2013. **2**(2): p. 83-101.

24. Varghese, N., et al., *Binding of DNA Nucleobases and Nucleosides with Graphene.* Chemphyschem, 2009. **10**(1): p. 206-210.

25. Wang, Y., et al., *Aptamer/Graphene Oxide Nanocomplex for in Situ Molecular Probing in Living Cells.* Journal of the American Chemical Society, 2010. **132**(27): p. 9274-9276.

26. Wan, Y., et al., *Impedimetric immunosensor doped with reduced graphene sheets fabricated by controllable electrodeposition for the non-labelled detection of bacteria.* Biosensors & Bioelectronics, 2011. **26**(5): p. 1959-1964.

27. Liu, J.B., et al., *Toward a Universal "Adhesive Nanosheet" for the Assembly of Multiple Nanoparticles Based on a Protein-Induced Reduction/Decoration of Graphene Oxide.* Journal of the American Chemical Society, 2010. **132**(21): p. 7279-+.

28. Song, B., et al., *Graphene on Au(111): A Highly Conductive Material with Excellent Adsorption Properties for High-Resolution Bio/Nanodetection and Identification.* Chemphyschem, 2010. **11**(3): p. 585-589.

29. Salihoglu, O., S. Balci, and C. Kocabas, *Plasmon-polaritons on graphene-metal surface and their use in biosensors.* Applied Physics Letters, 2012. **100**(21).

30. Nair, R.R., et al., *Fine structure constant defines visual transparency of graphene.* Science, 2008. **320**(5881): p. 1308-1308.

31. Lee, M. and P.M. Fauchet, *Two-dimensional silicon photonic crystal based biosensing platform for protein detection.* Optics Express, 2007. **15**(8): p. 4530-4535.

32. Armani, A.M., et al., *Label-free, single-molecule detection with optical microcavities.* Science, 2007. **317**(5839): p. 783-787.

33. Zourob, M., et al., *Optical leaky waveguide biosensors for the detection of organophosphorus pesticides.* Analyst, 2007. **132**(2): p. 114-120.

34. Cooper, M.A., *Optical biosensors in drug discovery.* Nature Reviews Drug Discovery, 2002. **1**(7): p. 515-528.

35. Fan, S.H., W. Suh, and J.D. Joannopoulos, *Temporal coupled-mode theory for the Fano resonance in optical resonators.* Journal of the Optical Society of America a-Optics Image Science and Vision, 2003. **20**(3): p. 569-572.

36. Huang, M., et al., *Sub-wavelength nanofluidics in photonic crystal sensors.* Optics Express, 2009. **17**(26): p. 24224-24233.

37. Crozier, K.B., et al., *Air-bridged photonic crystal slabs at visible and near-infrared wavelengths.* Physical Review B, 2006. **73**(11).

38. Ghenuche, P., et al., *Optical Extinction in a Single Layer of Nanorods.* Physical Review Letters, 2012. **109**(14).

39. Yanik, A.A., et al., *Seeing protein monolayers with naked eye through plasmonic Fano resonances.* Proceedings of the National Academy of Sciences of the United States of America, 2011. **108**(29): p. 11784-11789.

40. Cetin, A.E. and H. Altug, *Fano Resonant Ring/Disk Plasmonic Nanocavities on Conducting Substrates for Advanced Biosensing.* Acs Nano, 2012. **6**(11): p. 9989-9995.

41. Karagodsky, V., F.G. Sedgwick, and C.J. Chang-Hasnain, *Theoretical analysis of subwavelength high contrast grating reflectors.* Optics Express, 2010. **18**(16): p. 16973-16988.

42. Cao, L., et al., *Engineering light absorption in semiconductor nanowire devices.* Nature Materials, 2009. **8**(8): p. 643-647.

43. Cao, L.Y., et al., *Resonant Germanium Nanoantenna Photodetectors.* Nano Letters, 2010. **10**(4): p. 1229-1233.

44. Kippenberg, T.J., S.M. Spillane, and K.J. Vahala, *Demonstration of ultra-high-Q small mode volume toroid microcavities on a chip.* Applied Physics Letters, 2004. **85**(25): p. 6113-6115.

45. Schuller, J.A. and M.L. Brongersma, *General properties of dielectric optical antennas.* Optics Express, 2009. **17**(26): p. 24084-24095.

46. Reed, J.C., et al., *Graphene-Enabled Silver Nanoantenna Sensors.* Nano Letters, 2012. **12**(8): p. 4090-4094.

47. Stern, E., et al., *Label-free immunodetection with CMOS-compatible semiconducting nanowires.* Nature, 2007. **445**(7127): p. 519-522.

48. Guo, Q.S., et al., *Noise spectroscopy as an equilibrium analysis tool for highly sensitive electrical biosensing.* Applied Physics Letters, 2012. **101**(9).

49. Asenath-Smith, E. and W. Chen, *How To Prevent the Loss of Surface Functionality Derived from Aminosilanes.* Langmuir, 2008. **24**(21): p. 12405-12409.

50. Hsiao, V.K.S., et al., *Aminopropyltriethoxysilane (APTES)-functionalized nanoporous polymeric gratings: fabrication and application in biosensing.* Journal of Materials Chemistry, 2007. **17**(46): p. 4896-4901.

51. Zourob, M., et al., *Optical leaky waveguide biosensors for the detection of organophosphorus pesticides.* Analyst, 2007. **132**(2): p. 114-120.

52. Berg, O.G. and P.H. von Hippel, *Diffusion-controlled macromolecular interactions.* Annual review of biophysics and biophysical chemistry, 1985. **14**(1): p. 131-158.

53. Saha, K., F. Bender, and E. Gizeli, *Comparative study of IgG binding to proteins G and A: nonequilibrium kinetic and binding constant determination with the acoustic waveguide device.* Analytical chemistry, 2003. **75**(4): p. 835-842.

54. Berg, O.G. and P.H. Vonhippel, *Diffusion-Controlled Macromolecular Interactions.* Annual Review of Biophysics and Biophysical Chemistry, 1985. **14**: p. 131-160.

55. Raorane, D.A., et al., *Quantitative and label-free technique for measuring protease activity and inhibition using a microfluidic cantilever array.* Nano Letters, 2008. **8**(9): p. 2968-2974.

56. Kuo, S.C. and D.A. Lauffenburger, *Relationship between Receptor-Ligand Binding-Affinity and Adhesion Strength.* Biophysical Journal, 1993. **65**(5): p. 2191-2200.

57. Hoppener, C., R. Beams, and L. Novotny, *Background Suppression in Near-Field Optical Imaging.* Nano Letters, 2009. **9**(2): p. 903-908.

58. Cui, Y., et al., *Nanowire nanosensors for highly sensitive and selective detection of biological and chemical species.* Science, 2001. **293**(5533): p. 1289-1292.